Growth of $In_xGa_{1-x}As$ Metamorphic Pseudosubstrates on GaAs Wafers and the evolution of InAs Quantum Dots on These Substrates

By

SHAHRAM GHANAD-TAVAKOLI

Growth and Characterization of $In_xGa_{1-x}As$ ($0.0 \leq x \leq 0.3$) Metamorphic Pseudosubstrates Grown on (001) GaAs Wafers and the evolution of InAs Quantum Dots Grown on These Substrates

By

SHAHRAM GHANAD-TAVAKOLI

B. Sc., Sharif University of Technology, Tehran, Iran (2000)
M. Sc., Gwang-Ju Institute of Science and Technology, Gwang-Ju, South Korea (2004)

A Thesis
Submitted to the School of Graduate Studies
in Partial Fulfillment of the Requirements
for the Degree of
Doctorate of Philosophy

McMaster University

© Copyright by Shahram GHANAD-TAVAKOLI, February 2009

Doctor of Philosophy (2009) McMaster University
(Engineering Physics) Hamilton, Ontario, Canada

TITLE: Growth and Characterization of $In_xGa_{1-x}As$ ($0.0 \leq x \leq 0.3$) Metamorphic Pseudosubstrates Grown on (001) GaAs Wafers and the evolution of InAs Quantum Dots Grown on These Substrates

AUTHOR: Shahram GHANAD-TAVAKOLI
B. Sc., Sharif University of Technology, Tehran, Iran (2000).
M. Sc., Gwang-Ju Institute of Science and Technology, Gwang-Ju, South Korea (2004).

SUPERVISOR: Professor Emeritus David A. Thompson

NUMBER OF PAGES: xvii, 123

Abstract

$In_xGa_{1-x}As$ ($0.00 \leq x \leq 0.42$) metamorphic pseudosubstrate layers (MSLs) were studied as a means to change the lattice constant of the substrates and to modify the growth conditions of InAs quantum dots (QDs) by varying the strain. The MSLs showed symmetrical mosaicity about the <110> axes but the spread was different in the two orthogonal [110] and [$1\bar{1}0$] directions. The anisotropy in the mosaic spread in two <110> directions was correlated to asymmetry of kinks and multilevel-terrace growth front during the growth of $In_xGa_{1-x}As$ buffer layers. X-ray and electron diffraction along with the least squares criterion can interchangeably be employed to determine the lattice constant of the MSLs. It is possible to grow a defect free MSL with employing a compositional undershoot relative to the terminating buffer layer. Asymmetric tilt was found in an $In_{0.42}Ga_{0.58}As$ MSL grown on a singular (001) GaAs substrate with an initial layer of a low temperature (< 300 °C) grown InGaP prior to the growth of step-graded $In_xGa_{1-x}As$ ($x = 0.02$ to 0.42) buffer layers. The tilt around [$1\bar{1}0$] axis was correlated with the imbalance of the tilt component of the Burgers vector (BV) of the 60° α-dislocations. Climb and jog formation of β-dislocations in the presence of P-interstitials were considered as a plausible mechanism for multiplication of the like-sign BV α-dislocations. These results show that an asymmetric tilt boundary can be induced in mismatched heterointerfaces grown on singular substrates.

The evolution of InAs QDs on $In_xGa_{1-x}As$ ($0.0 \leq x \leq 0.3$) MSLs on GaAs substrates was studied. The results indicate that the ratio of the height (h) over lateral diameter (d) of the QDs decreases with decreasing strain (i.e. the morphology of the coherent islands evolve toward a uniform film morphology ($\frac{h}{d} = 0$) with deceasing strain). This evolution is analogous to the current

understating of strained uniform films where the tetragonality of the uniform film decreases with decreasing strain. The photoluminescence of the buried In(Ga)As QDs increases with increasing In (decreasing Ga) mole fraction of the underlying MSL; and thin strain-reducing capping layers do not significantly shift the PL. Modelling the experimental data suggests that Ga is incorporated in InAs QDs and the incorporation was estimated to linearly depend on the Ga mole fraction of the underlying $In_xGa_{1-x}As$ MSL indicating mass transport from the substrate at the growth temperature ($\cong$ 500 °C).

Acknowledgment

I have been fortunate to collaborate with genuine, smart, and generous individuals while conducting research at McMaster University. I thank my teachers and other researchers at large. My ideas were explicitly and implicitly influenced by their writing and creative ideas. I hope that I have taken my small steps forward from the foundation they have laid down. I greatly appreciate Professor Thompson for his supervision, continuous inspiration, patience and dedication to this work. He generously let me explore different areas which attracted my attention, examined my data and hypotheses critically, and offered invaluable advice and help in tough times. I particularly admire his meticulous vision in both practice and words. This work would not have been done without Dr. Robinson's help. He keenly grew my samples and taught me MBE operation and its intricacies. His constant curiosity and simplified explanations given with rigor and passion have always been inspiring. I thank Professor Mascher and Professor LaPierre who dedicated their time to my meetings. They constructively challenged my interpretations. I am indebted to Dr. Hulko who assisted me with TEM and helped me along the way. Many thanks will go to the following individuals. Ms. Stevanovic and Dr. Peng trained me in the clean room. They always offered a hand when I needed help. Graham Pearson patiently showed me how to operate the X-ray machine. I value his friendship and his openness to help. Mr. Fred Pearson and Andy Duft helped me in TEM and AFM laboratory. Mohamed Naser generously simulated the QD systems albeit his tight schedule. Josef Czaban shed light on some of the issues that came up during the research. Farseem Mohammedy always reminded me of the rich Persian literature in our discussions. Nicholas Leeson took me out of office and engaged me in lot of other activities. I am indebted to his friendship and support. Pei-Chun Chang was an inspiration during the second year of this work. I cannot thank her enough for her encouragement, patience and sacrifices. Nooshin Tajik was a source of

encouragement while I was writing this thesis. I acknowledge the financial support of Graduate Studies, Department of Engineering Physics, and Ontario Photonics Consortium (Photonics Research Ontario).

Finally, I am truly indebted to my parents and grandparents beyond measure and words. They sacrificed a lot along this journey. My mother always took care of everything with patience and my father always conveyed his invaluable experience and advice. My brother, Shervin, was a constant source of support and encouragement. I dedicate this work to them.

Shahram GHANAD-TAVAKOLI

McMaster University
Hamilton, Ontario, Canada
February 2009

Table of Contents

List of Figures

List of Tables

Abbreviations

Acronyms

AFM	Atomic Force Microscopy
BPC	Bevel-Polish and Cleavage
BV	Burgers' Vector
CBED	Convergent beam electron diffraction
DH	Double Heterostructure
ED	Electron Diffraction
EDX	Energy-dispersive X-ray spectroscopy
FCC	Face Centered Cubic
FEG	Field Emission Gun
FOLZ	First Order Laue Zone
FTIR	Fourier Transform Infra-Red Spectroscopy
FvdM	Frank-van der Merwe
HH	Heavy Hole
HOLZ	Higher Order Laue Zone
IC	Integrated Circuits
LD	Laser Diode
LED	Light Emitting Diode
LH	Light Hole
MBE	Molecular Beam Epitaxy
MD	Misfit Dislocation
ML	Monolayer
MSL	Metamorphic Pseudosubstrate Layer
PL	Photoluminescence
QD	Quantum Dot
QW	Quantum Well
QWI	Quantum Well Intermixing
QWr	Quantum Wire
RSM	Reciprocal Space Map
SAED	Selected-Area Electron Diffraction
SH	Single Heterostructure
S-K	Stranski-Krastanow
STM	Scanning Tunnelling Microscope
TEM	Transmission Electron Microscopy
VW	Volmer-Weber
WBDF	Weak Beam Dark Field
XRD	X-ray Diffraction
ZOLZ	Zero order Laue Zone

Symbols

ω	Angle that the incoming X-ray beam makes with the sample surface
σ	Stress
λ	Wavelength
ϕ	Acute angle, phase of electron wave
ε	Strain
2θ	Angle between diffracted and incoming beam
θ_B	Bragg angle
ω_{rel}	Tilt of the sample relative to the corresponding Bragg condition of the substrate
a, b, c	Lattice constant
b	Burgers' vector
d	Plane spacing and lateral diameter of QDs
E_g	Band gap
F	Structure factor
f	Atomic scattering factor
f_0	Resonant frequency
g, k	Reciprocal lattice vector
G_{exit}	Glancing exit reflection
G_{inc}	Glancing incidence reflection
G_n	Radius of the n_{th} order Laue Zone
H	Spacing between ZOLZ and FOLZ
h, k, l	Miller indices
h_c	Critical thickness
k_0	Force constant
L	Camera length
m_0	Mass of free electron
R	Distance reading on electron diffraction micrograph
r	Radius of Kossel ring
s_g	Excitation error
U, V, W	Direction indices

Chapter 1 Introduction

1.1. A Brief History of Semiconductor Diode Laser

The invention of the transistor in December 1947[1] had a profound impact on the way we live and work today. Our digital life style would not be possible without the invention of planar field effect transistor by Hoerni[2] and integrated circuits (IC) in 1958 by Kilby at Texas Instrument[3] with a major contribution of Noyce at Fairchild semiconductors.[4, 5] The invention of the transistor paved the path for intensive studies of electron-hole (e-h) pair recombination which was essential for understanding optoelectronic devices.[6] The semiconductor laser was a direct consequence of the studies done to understand the *p-n* junction devices and the carrier recombination in indirect- (IV*) and direct-gap (III-V†) semiconductors.[6]

Before summer of 1962, Hall[7] was skeptical about the possibility of a semiconductor laser. Firstly, known lasers required long optical paths which seemed incompatible with free carrier absorption in semiconductors. Secondly, the transitions in semiconductors were over a broader range of energies compared to the sharp atomic transitions in the available lasers in those days. Finally and most importantly, the radiative recombination in semiconductors had always been reported very inefficient. Hall's attitude[7] changed when Bernard and Duraffourg[8]

* Elemental semiconductors in group IV of the periodic table. e.g. Si and Ge.
† Binary or ternary semiconductors of the group III and V of the periodic table. e.g. GaAs, InP, InAs, InSb, and their alloys.

clarified the concept of stimulated emission in semiconductors; and Keyes and Quist[9] of Lincoln Laboratory and Pankove[10] of RCA demonstrated efficient radiative recombination in GaAs. In 1962, Hall et al.[11] followed by Nathan et al.[12] at IBM, demonstrated stimulated coherent infrared emission from GaAs *p-n* homojunctions at 77 K. Very shortly after that, Holonyak and Bevacqua reported coherent *visible* light emission (at 77 K) from *p-n* homojunctions fabricated from $GaAs_{1-x}P_x$ alloys.[13] The growth procedure of the $GaAs_{1-x}P_x$ was based on chemical vapour deposition of III-V compounds that Holonyak had patented.[14] The novelty of Holonyak's work was the use of the III-V crystalline *solid* solution that emitted *visible* (0.71 μm) radiation. Quist et al.[15] at Lincoln Laboratory also announced a GaAs *p-n* homojunction semiconductor laser shortly after Holonyak's report. Except for the diodes studied by Nathan et al., which had a mesa design,[12] the first injection diode lasers were typically rectangular parallelepiped chips of GaAs (or $GaAs_{1-x}P_x$) *p-n* homojunctions with the two ends of the chip polished to form a Fabry-Perot interferometer (the plane of the *p-n* junction was perpendicular to the polished ends). The *p-n* homojunctions had been previously formed by the diffusion of a p-type dopant (e.g. Zn) into an n-type substrate (e.g. Te doped). Bond et al.[16] were the first group to report the cleaving method to form the mirrors for the injection laser. In 1963 and in a report that went unnoticed by the researchers fabricating injection lasers, Kroemer[17] proposed a new structure (which he coined the term *heterostructure*) in which a layer of semiconductor with a relatively narrow band gap was sandwiched

between two layers of a wider band gap semiconductor. He intended to design a heterostructure device with a more efficient radiative recombination in narrow gap material compared to its *p-n* homojunction counterpart. In 1967, Woodall et al.[18] at IBM reported liquid phase epitaxial* (LPE) growth of $Al_xGa_{1-x}As$ on a GaAs substrate. Their work was based on the LPE growth of GaAs on GaAs reported by Nelson[19] at RCA. Because of almost identical lattice parameter of GaAs and AlAs (Figure A-1), high quality epitaxial layers can be obtained. Rupprecht's LPE growth[20] caused Hayashi and Panish[21] to consider a heterostructure design instead of using dopants to reduce the threshold current density of the lasers. Shortly after that, Kressel and Nelson[22] followed by Hayashi and Panish[23] reported almost identical $Al_xGa_{1-x}As$-GaAs *p-n* heterojunction lasers (Hayashi and Panish[24] coined the term single heterostructure (SH) to this structure in their detailed paper published in 1970). Alferov et al.[25] at the Ioffe Physicotechnical Institute in Leningrad had also reported $Al_xGa_{1-x}As$-GaAs *p-n* heterojunction lasers in 1968. Within a year, Hayashi and Panish[26] and Alferov et al.[27] reported a multilayer structure laser, called double heterostructure (DH) laser, with a reduced threshold current density compared to SH lasers.

* The term "*epitaxy*" (is from two Greek words, epi ($\varepsilon\pi\iota$) and taxis ($\tau\alpha\xi\iota\zeta$) meaning resting upon and arrangement, respectively.) was coined by Royer for the first time in 1928 (Bull. Soc. Franc. Mineral. Cristallogr. **51**, 7 (1928)); but it had already been known long before (I. Mugge, Neues Jahrb. Miner. Geol. u. Paleont. **16**, 335 (1903), and Th. V. Barker, Zeitschrift für Kristallographie **45**, 1 (1908)). Epitaxial growth refers to the formation of a single-crystalline film on top of a crystalline substrate where the orientation of the growing crystal is not random. Epitaxy occurs when the two parallel lattice planes (of the substrate and epilayer) have identical or quasi-identical form (or symmetry) and have closely similar lateral lattice spacings. Homoepitaxy and heteroepitaxy refer to the cases where the film and substrate are composed of the same or different materials, respectively. The most significant example of homoepitaxy was the deposition of Si on Si in the fabrication of ICs. Heteroepitaxy was (is) utilized in the fabrication of optoelectronic devices such as LEDs and LDs.

1.2. Quantum Confinement and Its Advantages on Device Performance

The confinement of charges to a region on the order of the charges' de Broglie wavelength (a few nano-meters up to a few tens of nano-meters) leads to quantization of the electron and hole energy levels. The quantum effects were proposed by Dingle and Henry in 1975.[28] Dupuis et al.[29] fabricated a single heterostructure quantum well (QW) laser in 1979. These QW lasers exhibited a lower temperature sensitivity of the threshold current density compared to the bulk *p-n* junction devices.[30] This was explained by the step-like density-of-states and the disturbed electron and phonon distributions in the QW active region.*, [31] Carrier collection, carrier thermalization, and QW band filling impose limits on the operation efficiency of single QW laser but these can be overcome by using multiple QW structures.[31]

Arakawa and Sakaki theoretically showed that by decreasing the dimensionality of the active region, the threshold current density of the laser devices show reduced temperature sensitivities.[32] The temperature dependence of a bulk *p-n* junction DH laser is related to thermal spreading of the injected carriers over a wide range of states (Figure 1.2-1 (a)). This thermal spreading will decrease the maximum gain at a given injection level. In a single QW laser, the resulting step-like density of states (Figure 1.2-1 (b)) reduces the effects of the thermal spreading. If the dimensionality of the active region is further reduced to a 1-dimensional (1D) structure, i.e. a quantum wire (QWr), the effect of thermal

* Active region is the section of the device where the injected carriers recombine to emit photons; this recombination converts electrical power to optical power.

spreading will be suppressed even further as the density of states appear as equally spaced lines which show a peak and decrease with increasing energy as shown in Figure 1.2-1 (c). In an active region with a 3-dimensional (3D) confinement, i.e. a quantum box or dot* (QD), the thermal spreading of the carriers should vanish and temperature dependence of the current density should disappear due to the delta-function density of states (Figure 1.2-1 (d)).

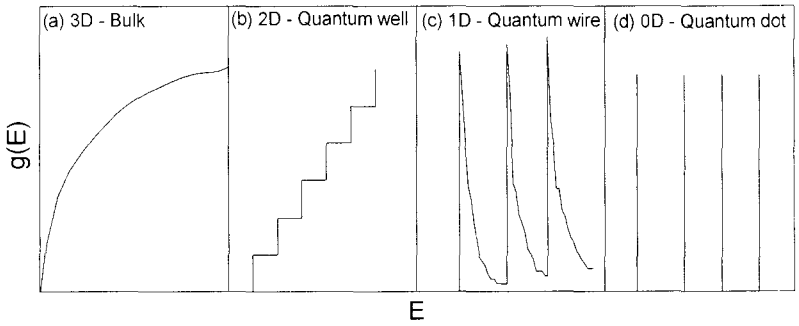

Figure 1.2-1: Schematic diagram of the density of states vs. energy of (a) bulk, quantum (b) well, (c) wire, and (d) dot.

1.3. Strain Incorporation in Active and Passive Regions of the Device

1.3.1. Introduction

Growth of strained layers has several advantages and drawbacks. Commercially available elemental and binary semiconductor (Si, Ge, GaAs, InP, GaSb, and InAs) substrates provide a limited range of lattice constants; this restricts epitaxial growth to a narrow range of ternary and quaternary semiconductor structures which limits the performance range of semiconductor devices that can be produced. Metamorphic pseudosubstrate layers (MSLs) using

* A quantum dot (QD) is a 3-D crystalline region in a semiconductor crystal (or amorphous material) that confines charges in three dimensions.

highly strained heterostructures have the potential to overcome the limited range of lattice constants of available substrates if sufficiently high quality crystalline layers can be grown.[33] $In_xGa_{1-x}As$ or $In_xAl_{1-x}As$ metamorphic heterostructures on GaAs substrates are of interest in high electron mobility transistors,[34] and long wavelength opto-electronic devices.[35] Another important application is the growth of III-V alloys on a Si substrate to combine the opto-electronic properties of III-V semiconductors with the high device density of Si microelectronics. MSLs will be explained in detail in Chapter 3. Moreover, strained layers allow growth of new and more complex material combinations on widely available substrates (e.g. Ge or GaAs on Si, $In_xGa_{1-x}As_yP_{1-y}$ on GaAs or InP). Strain makes it possible to access new band gap regimes through alloying which is not achievable with non-strained III-V semiconductors. More importantly, strained layers can be grown in tension to have the highest valence states to be light hole-like which will result in more efficient lasers and benefit faster complementary logic devices.[36] However, the growth of strained layers is thermodynamically unstable. As the thickness of the strained layer approaches a critical thickness, h_c, it is energetically favourable to relieve strain via the generation and multiplication of dislocations. This is due to the linear proportionality of the elastic strain energy ($E_{strain} \propto h$) and weaker dependence of dislocation energy ($E_{disl.} \propto \ln(h)$) with the film thickness (h). Dislocations act as mid-band gap carrier recombination centres and their presence will degrade the optical and electrical properties of the device. A more in-depth review of strain and dislocations will be given in Chapter 3.

1.3.2. Effect of Strain on Band-Structure and Device Performance

In an unstrained, bulk semiconductor, the light hole (LH) and heavy hole (HH) bands are degenerate at the Brillouin zone centre and a spin split-off band lies lower in energy (Figure 1.3.2-1(a)). For a biaxial tensile strained layer, the hydrostatic component of strain reduces the band gap while the axial component of the strain splits the degeneracy of the valence band maximum. This, in turn, introduces an anisotropic valence band structure, with the highest band being LH along the strain axis, $k_{\perp}$, and becomes "heavy-like" perpendicular to the $k_{\perp}$ axis (i.e. along $k_{\parallel}$) as shown in Figure 1.3.2-1 (b). The band gap increases for a layer under biaxial compression and the valence splitting is reversed so the highest band becomes the HH along the strain axis ($k_{\perp}$) and a "light-like" hole along the $k_{\parallel}$ strain axis (Figure 1.3.2-1 (c)).[37] Systematic treatments of the band structure of semiconductors in bulk, strained alloys and quantum structures can be found in Refs. [37, 38, 39, 40, 41, 42].

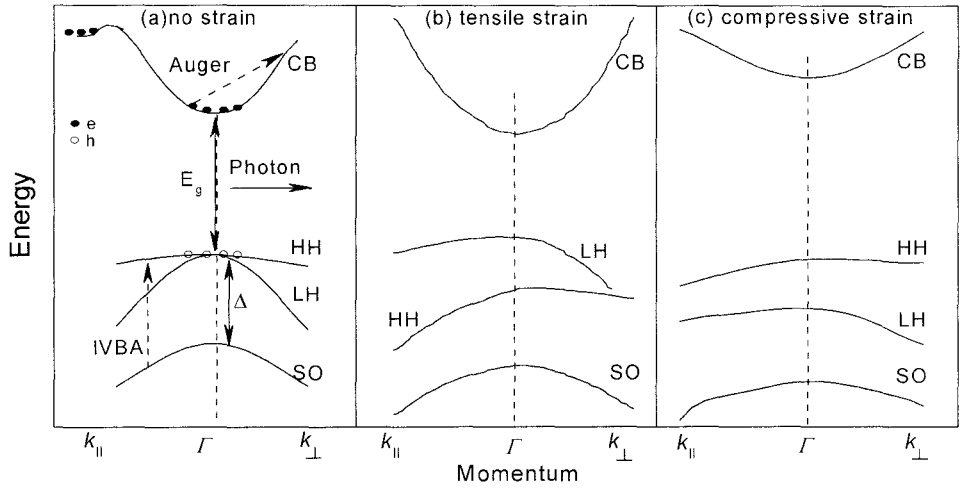

Figure 1.3.2-1: A schematic representation of the change in the band structure of a direct band gap semiconductor in (a) unstrained, (b) under biaxial tension, and (c) under biaxial compression.[37]

In a *p-n* junction semiconductor LD, the injected carriers recombine in the active region to emit photons. The broad energy bands in bulk semiconductors allow the carriers to occupy a wide range of energy and momentum states (Figure 1.3.2-1). However, lasing takes place at a sharply defined photon energy at or close to the band gap where the optical gain is maximized. A small fraction of the total injected carriers will contribute to lasing based on the energy-momentum dispersion curves. Moreover, the conduction band minimum is almost parabolic and the effective mass of electrons in GaAs is 0.1 m_0. However, there are two degenerate states in the valence band maximum, a heavy hole with $m_{hh} \sim 0.5\ m_0$ and a light hole with $m_{lh} \sim 0.1\ m_0$. Spin-orbit coupling splits off the three fold degenerate states to 2 p-like degenerate states and one split-off band. There are a couple of issues with this type of band structure. Firstly, the conduction band and

the valence band have different shapes, hence different densities of states, so a large hole concentration is needed to achieve population inversion. Secondly, cubic symmetry distributes holes equally between three types of states and are equally likely to produce light which is linearly polarized in x, y, z directions. Only one third of those holes are at correct energy in the right polarization state to contribute to the lasing mode. Loss mechanisms of photons travelling in the laser cavity at both long and short wavelengths can be explained through the band structure. At longer wavelengths (smaller energies), the photon energy becomes comparable to the separation between spin split-off and HH valence band. A long wavelength photon traveling through the laser cavity can excite the electron from the split-off band into an available hole state in the heavy hole valence band; this process is called inter-valence band absorption (IVBA) (Figure 1.3.2-1 (a)).[43] Most materials have indirect band gaps at higher energy levels, so stimulated direct recombination is suppressed at shorter wavelength; hence, lasing action is suppressed for photons with higher energies (Figure 1.3.2-1 (a)). When a layer is grown in tension (Figure 1.3.2-1 (b)), the light hole energy band moves above the heavy hole band and there will be a better match between the conduction and valence band densities of states. Hence, the threshold current density will be reduced.[44]

1.4. Formation of Quantum Dots During the Growth of Highly Strained Heterostructures

Research advancements in the past three decades have shown that the strain can be beneficial in the realization of 2- or 3-dimensionally confined quantum media. During the early days of quantum confinement realization, Yano et al. were studying the growth of InAs on GaAs substrates in Japan.[45] Schaffer et al.,[46] Goldstein et al.,[47] Houzay et al.,[48] and Elman et al.[49] studied nucleation and strain relaxation of In(Ga)As grown on (001) GaAs substrates by molecular beam epitaxy* (MBE). In the following years, several methods were used to attain two or three dimensional confinement. Etching of QW structures using a combination of lithography and etching[50, 51, 52, 53] was attempted but this had some drawbacks such as fabrication complexity, introduction of defects due to etching steps, and the limited resolution of the electron lithography. Other approaches included cluster formation from gas[54] or solution precursors,[55] growth guided by substrate patterns; i.e. on etched grooves or holes,[56] or facets of high index surfaces;[57] confinement due to local inter-diffusion,[58] and the strain field of the nano stressors.[59] The major breakthrough was the direct formation of coherent, self organized QDs during highly strained (lattice mismatch > 2 %) layer growth on singular† substrates, e.g. Ge on Si (001)[60] or In(Ga)As on GaAs (001).[61, 62, 63, 64]

---

* Molecular beam epitaxy is a growth technique in which layers are grown by impinging thermal beams of atoms or molecules on a heated substrate under ultrahigh vacuum conditions.

† A singular crystallographic surface is a plane on which all the surface atoms (with dangling bonds) lie in a single geometrical plane. In a vicinal surface, the atoms with dangling bonds do not lie in one single plane. Therefore, vicinal surfaces can be resolved into atomic scale singular surfaces.

The potential of coherently self-organized islands during the growth of these highly strained epitaxial layers has attracted considerable attention in the past 2 decades.[65]

There are three known heteroepitaxial growth modes, namely Frank-van der Merwe (FvdM),[66] Volmer-Weber (VW),[67] and Stranski-Krastanow (S-K).[68] VW, or island growth mode, results when atoms or molecules are more strongly bound to each other than to the substrate; e.g. metal or semiconductor films deposited on oxide substrates. In FvdM, or the layer by layer growth mode, the atoms or molecules preferentially bind to the substrate rather than to each other. The atoms impinging on the substrate surface diffuse across the clean reconstructed surface; arrange themselves, starting from step edges to form a continuous epitaxial layer. In S-K, or layer by layer plus island growth mode, the initial growth occurs layer by layer, however, as the layer thickness increases (typically about a few monolayer thick[48, 60, 63]) islands are formed on top of a 2D wetting layer to relax the elastic energy. The S-K growth mode is known to be the underlying mechanism for the growth of strained semiconductors, e.g. Ge on Si (001),[60] and In(Ga)As on GaAs (001).[63]

1.5. Strain Modifications in In(Ga)As QDs/GaAs system to Achieve Long Wavelength (~ 1.55 μm) Emission

Following the realization of coherent self-assembled QDs, the fabrication of light emitting devices with a QD active region was vigorously pursued. In

1994, Kirstaedter et al.[69] fabricated a laser with an active region of In(Ga)As QDs on a GaAs substrate. Fafard et al.[70] demonstrated QD lasers in the visible region of optical spectrum. The motivation for the production of QD lasers was (is) based on the requirement for temperature insensitive lasers in optical telecommunications systems. These lasers need to emit at wavelengths of 1.3 and 1.55 μm in order to minimize transmission losses in current silica fibres used for short and long haul communications.[71] Most commercial LDs for telecommunication applications are grown on InP substrates using QW structures based on lattice-matched or slightly strained $In_{1-x}Ga_xAs_yP_{1-y}$ quaternary alloys. However, InP substrates are only available in up to 100 mm diameter wafers, are somewhat fragile and have relatively high threading dislocation densities which will result in reduced yields during device fabrication. More recently, long wavelength lasers (~ 1.55 μm) have been fabricated with an InGaAs QW on an $In_xGa_{1-x}As$ MSL,[72] InGaAsN/GaAsN,[73] and InGaNAsSb/GaNAsSb[74] QWs on GaAs substrates. However, both InP- and GaAs-based QW lasers exhibit temperature sensitivity in the emission wavelength (section 1.2). To meet the demand of the telecommunication industry for long wavelength, temperature insensitive lasers, several research groups have shown photoluminescence,[75, 76, 77, 78] and lasing emission at or near 1.3 μm[79, 80, 81, 82, 83] and 1.5 μm[35, 84] spectral ranges from In(Ga)As QD active media on GaAs substrates. Several approaches, namely growth of InGaAs QDs on GaAs,[75, 79, 85] strain-engineered InAs QDs on GaAs,[77, 83, 85, 86, 87, 88] and using MSLs on a GaAs substrate along with strain

reducing capping layers[84, 85, 89] have been considered to obtain the desired emission spectral range. All the aforementioned approaches rely on the change in the ground state transition by modifying the band gap of the QDs. The change in the band gap is achieved by growing $In_xGa_{1-x}As$ QDs (which also modifies the strain) on a GaAs substrate or by varying the strain either by growing strain reducing capping layer or by increasing the lattice constant of the underlying substrate (e.g. growing InAs QDs on MSLs). The growth of InAs QDs on MSLs also allows the fabrication of devices on larger and higher quality GaAs substrates compared to InP substrates.

1.6. Purpose and Outline of the Thesis

There is no systematic study on the evolution of InAs QDs and their emission wavelength with varying strain on MSLs on GaAs substrates. Moreover, LDs emitting at 1.5 μm have been fabricated based on a defect reduction (DR) mechanism[90] for growing an MSL which relies on a complex procedure involving thermal etching of the dislocated areas in the presence of high temperature stable layer and re-growing a defect-free over-layer. This thesis aims to fabricate and study $In_xGa_{1-x}As$ MSLs without employing the complex DR procedure and study the evolution of InAs QDs grown on $In_xGa_{1-x}As$ ($0.0 \leq x \leq 0.3$) MSLs.

Chapter 2 will describe the epitaxial growth processes and provide details of the procedures used to characterize the structures grown. Chapter 3 provides the results of experimental studies on the growth and characterization of the

$In_xGa_{1-x}As$ MSLs; specifically the dislocation interaction, and showing the tilt and mosaicity that occur in the buffer layers and pseudosubstrate. It will be shown that it is possible to grow a defect free pseudosubstrate without employing a complicated DR as reported in Ref. [90]. In Chapter 4, the evolution and photoluminescence of InAs QDs with varying strain are presented. The ratio of height to lateral diameter of the QDs is shown to increase with increasing strain. This indicates that the InAs coherent island morphology evolves toward uniform film morphology with deceasing strain. It will be shown that the photoluminescence of the buried InAs QDs increases with increasing In (decreasing Ga) mole fraction of underlying MSL. Thin (2 nm) strain-reducing capping layers do not significantly shift the PL peak. The QD systems were modeled and the results suggest that, in order to achieve an agreement with the experimental results, Ga incorporation is occurring in the InAs QDs. The magnitude of this Ga incorporation is shown to linearly depend on the Ga mole fraction of the underlying $In_xGa_{1-x}As$ substrate. The final chapter concludes this work and provides suggestions for future research.

Chapter 2 Experimental Procedures

2.1. Molecular Beam Epitaxial Growth

Samples were grown by gas-source MBE in a system manufactured by SVT Associates. The group V elements were deposited as dimers (As_2, P_2) produced using gas sources, AsH_3 and PH_3, which were dissociated by passing the gases over a hot filament at 950 °C. The MBE growths were performed on 2-inch diameter, epi-ready, (001) ± 0.1°, Si-doped (n = 1×10^{18} cm^{-3}) GaAs substrates provided by Wafer Technology Ltd. (Ingot Number = WV 16472). In some instances, semi-insulating GaAs wafers were used which will be indicated in the growth structures. The etch pit density of the wafers were reported to be less than 500 cm^{-2}. All layers, except the QDs, were grown at a nominal growth rate of 1 $\mu m \cdot hr^{-1}$. During growth, the substrates were mounted facing downward on a molybdenum holder rotating at a frequency of ~ 0.25 Hz. The substrates were initially degassed at 300 °C for ~ 15 minutes. They were then transferred to the growth chamber and the substrate surfaces were cleaned *in-situ* using a hydrogen plasma and a sufficient excess flux of As_2 to compensate for any evaporative loss from the substrate surface. This cleaning process was done at a pyrometer temperature reading of 15 - 20 °C hotter than planned for the subsequent growth of the epitaxial layers. The pyrometer was calibrated using a silicon wafer.

2.1.1. Metamorphic Substrate Growth

An initial 100 nm thick GaAs buffer layer was grown on the substrates prior to the growth of the metamorphic layers. The metamorphic layers were then grown consisting of step graded $In_xGa_{1-x}As$ buffer layers and the structure was finally capped with an additional 500 nm layer of the desired composition (x) which formed the metamorphic pseudosubstrate for the growth of the subsequent QD structure. The metamorphic buffer layers ($In_xGa_{1-x}As$), where x is varied incrementally in steps of 0.02, and the metamorphic substrate layer (MSL) were grown by adjusting the In/Ga ratios based on calibration growths of $In_{0.1}Ga_{0.9}As$ and $In_{0.485}Ga_{0.515}P$ on GaAs substrates. If the desired metamorphic substrate was to have a composition up to ~ 30% In, all layer growths were extrapolated from the $In_{0.1}Ga_{0.9}As$ calibration. If the substrate was terminating at a layer with > 30% In, the layers with x varying from 0.0 to 0.2 were grown based on the $In_{0.1}Ga_{0.9}As$ calibration and those with x varying from 0.2 to 0.4 were grown based on the $In_{0.485}Ga_{0.515}P$ calibration. The final terminating pseudosubstrate served for X-ray measurement purposes.

In one instance, a low-temperature $In_{0.485}Ga_{0.515}P$ (LT-InGaP) layer was grown on top of the GaAs buffer, so it preceded the first metamorphic buffer layer. This was employed following a publication showing that growth of InAsP metamorphic layers on a LT-InP layer resulted in a much improved MSL.[91] This growth was carried out using a thermocouple reading of 245 °C (which is

extrapolated to be ~ 290 - 300 °C in pyrometer temperature) where the thermocouple was placed close to the back surface of the substrate.

2.1.2. Quantum Dot Growth

Quantum dots were grown at a nominal growth rate of 0.1 ML/sec. A shutter sequence approach (Figure 2.1.2-1) was used to achieve this desired growth rate based on the available flux from the indium cell. A specific example based on the structure illustrated in Table 2.1.2-1 will be described to clarify the process. After determining the lattice constant of the MSL (it will be shown later that the MSL layers are not fully relaxed), a buffer layer was grown of $In_xGa_{1-x}As$ where x has been adjusted in order to be laterally lattice-matched to the partially strained MSL layer. In this example, the layer on top of pseudosubstrate ($In_{0.21}Ga_{0.79}As$) should contain 17% In to be laterally lattice-matched to the underlying substrate. An $In_{0.4}Ga_{0.6}As$ capping layer was grown over the QDs to relieve strain and red shift the wavelength.

Table 2.1.2-1: Structure of a specific example of InAs QDs capped with $In_{0.40}Ga_{0.60}As$ on an $In_{0.21}Ga_{0.79}As$ metamorphic substrate. Note that the pseudosubstrate is not fully relaxed and the lateral lattice constant correlates to $In_{0.17}Ga_{0.83}As$.

2.5 nm - $In_{0.40}Ga_{0.60}As$
2.6 ML InAs QD @ 0.1 ML/sec
150 nm - $In_{0.17}Ga_{0.83}As$
$In_{0.21}Ga_{0.79}As$ (terminating pseudo-substrate)

After the growth of the $In_{0.17}Ga_{0.83}As$ buffer layer, the In and Ga cell temperatures were adjusted for the required composition of the $In_{0.4}Ga_{0.6}As$ capping layer. Thus, the In and Ga cells are set in such a way to be able to grow

InAs at a growth rate of 0.4 μm/hr and GaAs at a growth rate of 0.6 μm/hr on a GaAs substrate, respectively. Since the growth is on a pseudosubstrate with a lattice constant larger than that of the GaAs substrate, the growth rate increases. The Poisson's effect (during the growth of strained QDs) will also lead to a slightly faster growth rate which will be ignored in our calculations. The lattice constant of the pseudosubstrate calculated from X-ray results was 5.72243 Å which was ~ 1.22% bigger than the GaAs lattice constant. The growth rate of 1 μm/hr of relaxed GaAs corresponds to 0.983 ML/sec. Therefore, the InAs growth rate of 0.4 μm/hr on a GaAs substrate becomes 0.393 ML/sec. Since growth occurs on a substrate with a larger lattice constant and in the planar regime, this growth rate should be multiplied by the square of the difference of lattice constants.

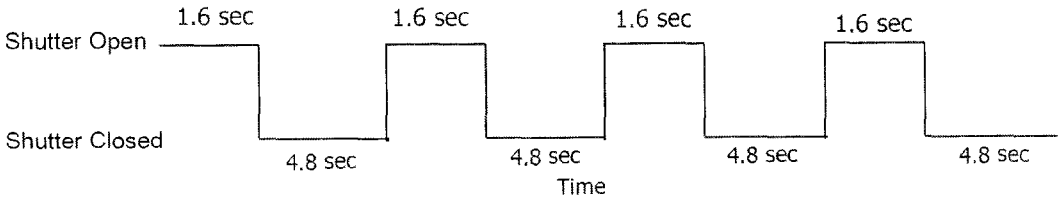

Figure 2.1.2-1: Schematic diagram of the In cell shutter sequence (4 cycles) during the growth of InAs QDs for the structure in Table 2.1.2-1. (Arsenic shutter is continuously open during the growth.)

Hence, the approximate growth rate of InAs on a substrate with a lattice constant of 5.72243 Å is $0.393 \cdot (1+0.0122)^2 = 0.403 \frac{\text{ML}}{\text{sec}}$. The time required to grow 2.6 MLs at a growth rate of 0.403 ML/sec is 6.45 sec. This growth time was divided

into 4 cycles (t_{open}= 1.6 sec). The t_{closed}= 4.8 sec was determined (according to Equation 2.1.2-1) in such a way that the growth rate of each cycle was 0.1 ML/sec. Figure 2.1.2-1 shows the schematic diagram of the In cell shutter sequence (4 cycles) during the growth of InAs QDs for the structure in Table 2.1.2-1.

Equation 2.1.2-1

$$\frac{(1.6\,\text{sec}\cdot 0.403\,\frac{ML}{\text{sec}})}{(1.6+t_{closed})\,\text{sec}} = 0.1\,\frac{ML}{\text{sec}}$$

2.2. Lattice Structure and Polarity Determination

The absence of centro-symmetry in the zinc blende crystals has an impact on the properties of these crystals and their extended defects (e.g., dislocations). A complete understanding of such defects has to be made based on the correct determination of the crystal polarity. The sign convention for polarity used throughout this text is based on locating cation atoms (Ga, In) at the origin and the anion atoms (As, P) at the other site of the basis unit (1/4, 1/4, 1/4). With this convention the group III and V bonds on a (001) surface will be in $<111>$ and $<\bar{1}\bar{1}\bar{1}>$ directions, respectively, according to Figure 2.2-1.[92] Figure 2.2-2 is a planar view of (001) GaAs wafer showing the orientation of different <110> directions and {111} planes. The inset shows the major and minor flats of a wafer based on the US convention. The crystal polarity of the GaAs substrate can be verified either by preferential etching or using convergent beam electron diffraction (CBED) method developed by Taftø and Spence;[93] with a detailed

theoretical description provided by Spiecker.[94] The polarity of one wafer was verified using CBED and the theory will be explained in detail later. Preferential etching of GaAs can also be used to determine the polarity;[92, 95, 96, 97, 98] more recipes can be found in the review paper by Clawson.[99]

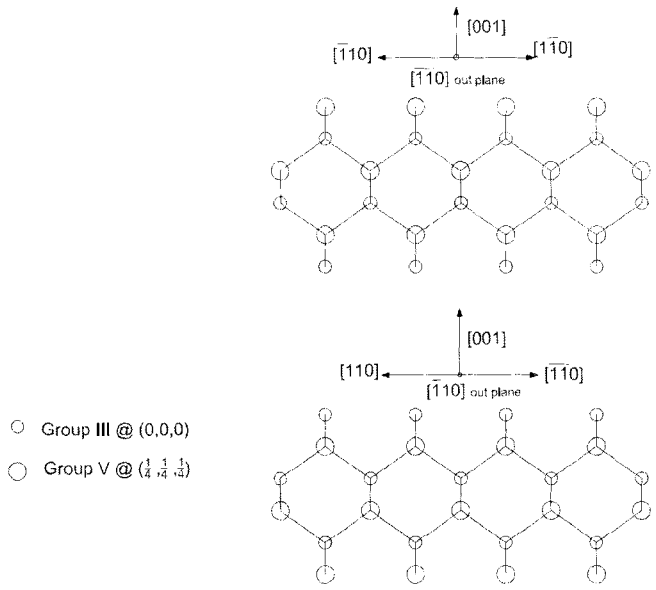

Figure 2.2-1: Group III and V bond directions based on locating cation atoms (Ga, In) at the origin and the anion atoms (As, P) at the other site of the basis unit (1/4, 1/4, 1/4).

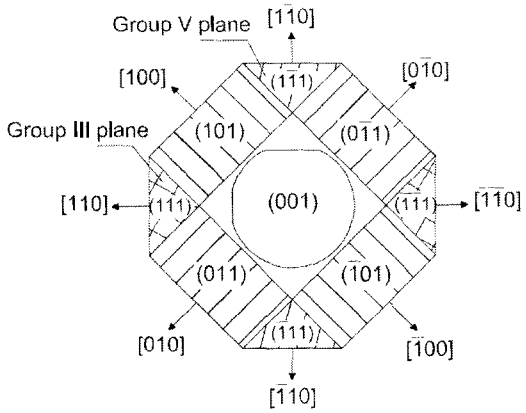

Figure 2.2-2: Planar view of (001) GaAs wafer showing the orientation of different <110> directions and {111} planes. The inset shows the major and minor flats of a wafer with the US convention.

2.3. X-ray Diffraction

A BEDE D1 triple axis diffractometer was used in this work. A two bounce asymmetric Si monochromator and a 50-μm slit was used to condition a Cu-Kα_1 (λ = 1.54056 Å) X-ray beam. In a few experiments, another two bounce asymmetric Si monochromator was used at the detector arm to restrict the angular acceptance of the detector and improve the resolution.

2.3.1. Reciprocal Space Mapping

An ω-2θ scan (ω is the angle that the incoming beam makes with the sample surface, 2θ is the angle between diffracted and incoming beam) will result in a rocking curve which provides strain information. Figure 2.3.1-1 shows an example of the ω-2θ scans (at ω_{rel} = 0, where ω_{rel} is the tilt of the sample relative to the corresponding Bragg condition of the substrate) around the [110] and [$1\bar{1}0$] directions for the $In_{0.42}Ga_{0.58}As$ MSL with an underlying LT-$In_{0.48}Ga_{0.52}P$ layer. The epilayer peak is absent in the scan around [$1\bar{1}0$]. Two dimensional reciprocal space maps (RSM)[100] were carried out and showed that the epilayer was tilted with respect to the substrate around the [$1\bar{1}0$] direction.

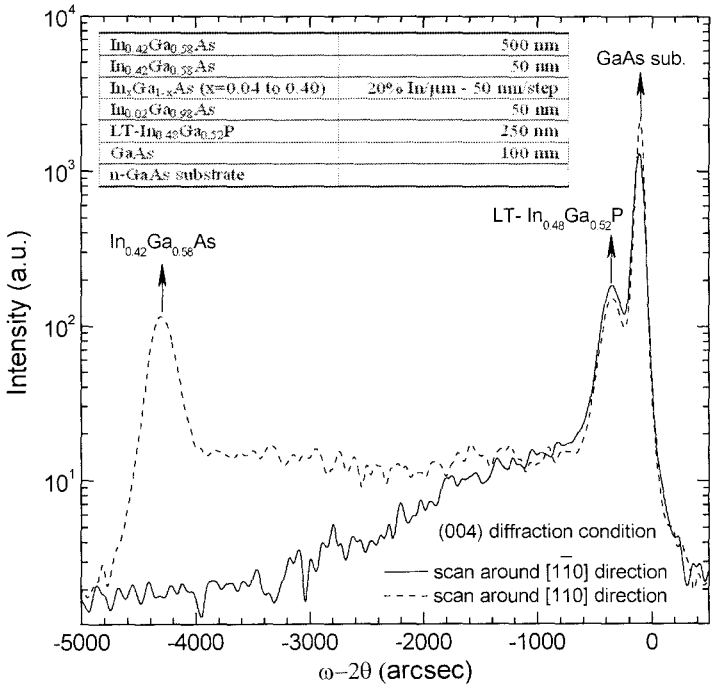

Figure 2.3.1-1: (004) ω-2θ X-ray scans (at ω_{rel}=0) around [110] and [1$\bar{1}$0] directions for $In_{0.42}Ga_{0.58}As$ MSL with underlying LT-$In_{0.48}Ga_{0.52}P$. The MSL peak is absent in the scan around [1$\bar{1}$0] due to tilting of the epilayer with respect to the substrate around that direction. The inset shows the corresponding structure (Table 3.4.2-1 (a)).

To obtain a two dimensional intensity distribution in reciprocal space, one must collect a series of ω-2θ scans at different sample angle offsets (ω-2θ vs. ω_{rel}). Figure 2.3.1-2 shows the schematic diagram of the Ewald sphere around a reciprocal lattice point (RLP) of the substrate and epilayer in a space mapping configuration. This procedure will result in a measurement of the X-ray intensity distribution near a reciprocal space point as shown in Figure 2.3.1-3.

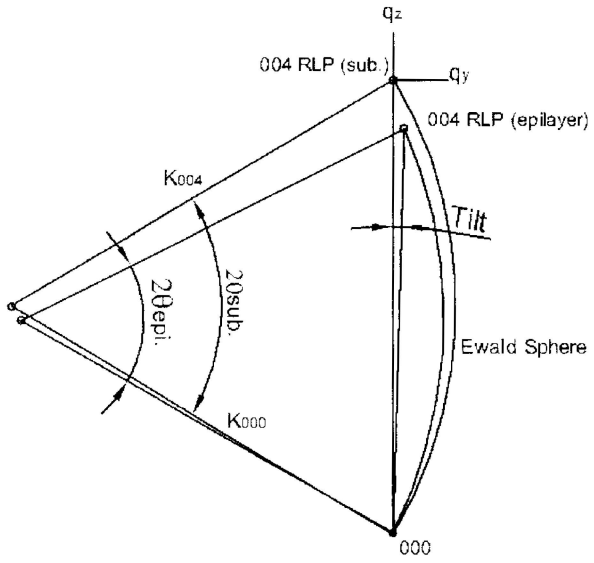

Figure 2.3.1-2: Schematic diagram of Ewald sphere around a reciprocal lattice point (RLP) of the substrate and epilayer in a space mapping configuration.

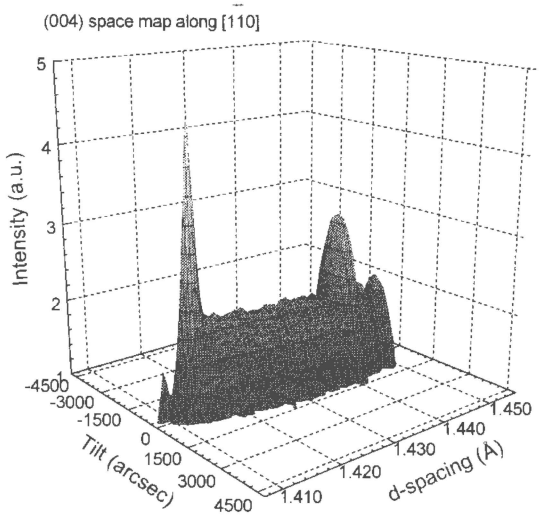

Figure 2.3.1-3: (004) 3D d-space surface map of $In_xGa_{1-x}As$ MSLs in $[1\bar{1}0]$ direction. (Refer to Table 3.5-1 for the corresponding structure.)

After growing the MSL, 2-inch diameter wafers were cleaved into quarters. One quarter of the wafer was mounted (carefully to avoid curvature of the sample) with [110] and then with $[1\bar{1}0]$ parallel to the beam direction. The

angular data were converted to d-spacing maps using an equation derived from the Ewald sphere construction which transforms the diffracted intensity of $\Delta\theta$ versus ω_{rel} to diffracted intensity of Δd-spacing versus ω_{rel}.[101]

2.3.2. Lattice Parameter Determination

Determination of the in-plane and out-of-plane lattice constants of epitaxially grown ternary and quaternary epilayers is necessary for predicting the composition (e.g., for calibration of the cells), strain (or tetragonality of the unit cell), and setting the concentration for coherent continuous growth. The examination of atomic scale features by the diffraction technique requires an incident beam wavelength less than the length scale of interest. Both X-rays and high energy electrons satisfy these conditions. Electrons interact with charges in the material and these interactions require the sample to be transparent to the beam; hence limit its thickness. In comparison, X-ray diffraction is suitable for studying thin films on substrates, requiring no sample thinning. The electron wavelength is considerably smaller (~ 0.0335 Å @ 120 keV) than that of X-rays' ($\lambda_{Cu-K\alpha_1} = 1.54056$ Å) resulting in a larger Ewald sphere.

Coherent as-grown epitaxial layers may be under strain; hence, tetragonal distortion makes in-plane and perpendicular lattice parameters unequal. In-plane biaxial strains are small in most cases; so, for simplicity and some mathematical implications which will be clear in later discussion, the two perpendicular in-plane lattice constants were considered equal ($a_x = a_y$) and different from the

lattice constant in the growth direction ($a_x = a_y \neq a_z$). The lattice parameters were determined by calculating the d spacing deduced from the peak separation in the rocking curves. The inter-planar spacing of the hkl planes (d_{hkl}) in the most general form of orthorhombic crystals ($a_x \neq a_y \neq a_z$) is

Equation 2.3.2-1

$$d_{hkl} = \frac{1}{\sqrt{\frac{h^2}{a_x^2} + \frac{k^2}{a_y^2} + \frac{l^2}{a_z^2}}} \qquad [102]$$

where a_x, a_y and a_z are the lattice constants and h, k, and l are the Miller indices of the corresponding planes. The inter-planar spacing is correlated to the Bragg angle through Bragg's law

Equation 2.3.2-2

$$d_{hkl} = \lambda / 2\sin\theta_B \qquad [103]$$

The Bragg angle, θ_B, and its corresponding inter-planar spacing of the epilayer are determined based on its corresponding Bragg peak separation from the substrate peak in ω-2θ rocking curve. A 004 reflection rocking curve is performed to determine the lattice constant in the growth direction for the epilayers grown on (001) substrates. Figure 2.3.1-1 shows an example of a 004 ω-2θ scan (at $\omega_{rel} = 0$) of an $In_{0.42}Ga_{0.58}As$ MSL grown on a GaAs substrate. The epilayer peak is absent in the scan around $[1\bar{1}0]$ (solid line) due to tilt of the epilayer with respect to the substrate around the $[1\bar{1}0]$ direction.

2.3.2.1. The Glancing Incidence and Glancing Exit Technique

For ternary and quaternary compounds, assuming that the two in-plane lattice constants are equal ($a_x = a_y$), one needs the measurements of diffraction scans for two different planar reflections to find the in-plane and out of plane lattice constants (a_x and a_z). The angle peak separation between the epilayer and substrate of both symmetrical (e.g. (004)) and asymmetrical (e.g. (224)) glancing incidence (G_{inc}) and glancing exit (G_{exit}) reflections can be used to determine a_x and a_z. The G_{inc} and G_{exit} peak separation measurements are recorded by rocking the sample in glancing incidence and glancing exit configuration in the equatorial zone. Figure 2.3.2.1-1 shows the schematic diagram of the G_{inc} and G_{exit} configuration superimposed on each other. Note that the acute angle (ϕ: the angle between the reflecting planes and the surface of the substrate) is changed ($\delta\phi$) due to tetragonal distortion. The inter-planar spacing of the epilayer is determined from the Bragg angle difference of the epilayer and that of the substrate from G_{inc} and G_{exit} rocking curves.

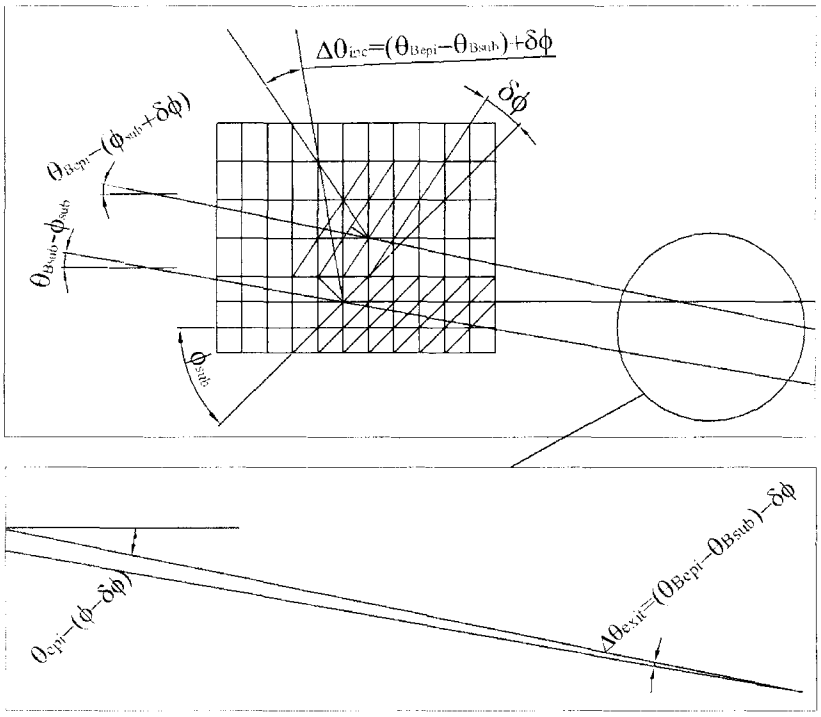

Figure 2.3.2.1-1: Schematic diagram of the G_{inc} and G_{exit} set-up in X-ray diffraction superimposed on each other.

The solution of the trigonometric and algebraic equations (assuming equal perpendicular in-plane lattice parameters) will correlate in-plane ($a_x \equiv a_{epi}$) and out-of-plane ($a_z \equiv c_{epi}$) lattice constants to the Bragg (θ_B) and acute angles (ϕ) according to the following equations

Equation 2.3.2.1-1

$$\left.\begin{aligned}\Delta\theta_{inc} &= \delta\theta_B + \delta\phi \\ \Delta\theta_{exit} &= \delta\theta_B - \delta\phi\end{aligned}\right\} \Rightarrow \begin{cases}\delta\theta_B = \dfrac{\delta\theta_{inc} + \delta\theta_{exit}}{2} \\ \delta\phi = \dfrac{\delta\theta_{inc} - \delta\theta_{exit}}{2}\end{cases}$$

where $\delta\theta_B$ is the difference between the epilayer and substrate Bragg angles, and $\delta\phi$ is the difference between the epilayer and substrate acute angles corresponding to hkl planes. Since θ_{Bsub} and ϕ_{sub} are known, we can calculate θ_{Bepi} and ϕ_{epi}. Using the geometry of the tetragonal crystal, we obtain

Equation 2.3.2.1-2

$$\sec^2 \phi_{epi} = \left(\frac{c^2}{l^2}\right)\left\{\frac{h^2+k^2}{a_{epi}^2} + \frac{l^2}{c_{epi}^2}\right\}$$

We can also obtain the following from the Bragg law

Equation 2.3.2.1-3

$$\frac{4\sin^2\theta_{Bepi}}{\lambda^2} \equiv \frac{1}{d_{hkl,epi}^2} = \left\{\frac{h^2+k^2}{a_{epi}^2} + \frac{l^2}{c_{epi}^2}\right\}$$

Then, from Equation 2.3.2.1-2 and Equation 2.3.2.1-3, the epilayer lattice constants are determined as

Equation 2.3.2.1-4

$$c_{epi} = \frac{l\lambda}{2\sin\theta_{Bepi}\cos\phi_{epi}}$$

$$a_{epi} = \frac{\lambda\cdot\sqrt{h^2+k^2}}{2\cdot\sin\theta_{Bepi}\cdot\sin\phi_{epi}}$$

2.3.2.2. Least Square Criterion Method for Lattice Constant Determination

The combination of different symmetric and asymmetric reflections is mutually inconsistent and leads to different lattice constants.[104] To clarify this inconsistency, the lattice parameter determination based on a least square criterion and combination of two pairs of electron diffraction conditions will be discussed in section 3.4.3.2. Fatemi[104] proposed a refinement technique using a least square criterion which led to consistent lattice parameters. In this technique, the measured inter-planar spacings, $\frac{1}{d_{hkl}^2}$, are slightly adjusted to minimize the errors and bring about consistency. The following example is for rocking curves around

four symmetric and/or asymmetric reflections. The following parameters are defined for brevity

Equation 2.3.2.2-1

$$\frac{1}{a^2} = A,\ \frac{1}{c^2} = C$$

Equation 2.3.2-1 and Equation 2.3.2.2-1 can be written for four arbitrary reflections as

Equation 2.3.2.2-2

$$P \equiv \frac{1}{d^2_{h_1k_1l_1}} = (h_1^2 + k_1^2)A + l_1^2 C$$
$$Q \equiv \frac{1}{d^2_{h_2k_2l_2}} = (h_2^2 + k_2^2)A + l_2^2 C$$
$$R \equiv \frac{1}{d^2_{h_3k_3l_3}} = (h_3^2 + k_3^2)A + l_3^2 C$$
$$S \equiv \frac{1}{d^2_{h_4k_4l_4}} = (h_4^2 + k_4^2)A + l_4^2 C$$

To bring the equations into consistent solutions for A and C, the calculated values of P, Q, R, S will be adjusted according to the least square criterion

Equation 2.3.2.2-3

$$P(1+p) = (h_1^2 + k_1^2)A + l_1^2 C$$
$$Q(1+q) = (h_2^2 + k_2^2)A + l_2^2 C$$
$$R(1+r) = (h_3^2 + k_3^2)A + l_3^2 C$$
$$S(1+s) = (h_4^2 + k_4^2)A + l_4^2 C$$

where p, q, r, and s are the necessary adjustments. Two more equations are required to solve the above set of equations (Equation 2.3.2.2-3) with six unknowns. Thus, the least square criterion is applied to put a constraint upon p, q, r, and s.

Equation 2.3.2.2-4

$$\text{Least square criterion } p^2+q^2+r^2+s^2=\text{minimum}$$

$$\begin{cases} 2p\dfrac{\partial p}{\partial A}+2q\dfrac{\partial q}{\partial A}+2r\dfrac{\partial r}{\partial A}+2s\dfrac{\partial s}{\partial A}=0\Rightarrow\dfrac{p(h_1^2+k_1^2)}{P}+\dfrac{q(h_2^2+k_2^2)}{Q}+\dfrac{r(h_3^2+k_3^2)}{R}+\dfrac{s(h_4^2+k_4^2)}{S}=0 \\ 2p\dfrac{\partial p}{\partial C}+2q\dfrac{\partial q}{\partial C}+2r\dfrac{\partial r}{\partial C}+2s\dfrac{\partial s}{\partial C}=0\Rightarrow\dfrac{pl_1^2}{P}+\dfrac{ql_2^2}{Q}+\dfrac{rl_3^2}{R}+\dfrac{sl_4^2}{S}=0 \end{cases}$$

Rearranging Equation 2.3.2.2-3 and Equation 2.3.2.2-4 into a matrix format results in

Equation 2.3.2.2-5

$$\begin{aligned} &Pp-(h_1^2+k_1^2)A-l_1^2C=-P \\ &Qq-(h_2^2+k_2^2)A-l_2^2C=-Q \\ &Rr-(h_3^2+k_3^2)A-l_3^2C=-R \\ &Ss-(h_4^2+k_4^2)A-l_4^2C=-S \\ &\frac{p(h_1^2+k_1^2)}{P}+\frac{q(h_2^2+k_2^2)}{Q}+\frac{r(h_3^2+k_3^2)}{R}+\frac{s(h_4^2+k_4^2)}{S}=0 \\ &\frac{pl_1^2}{P}+\frac{ql_2^2}{Q}+\frac{rl_3^2}{R}+\frac{sl_4^2}{S}=0 \end{aligned}$$

The matrices corresponding to the above set of equations are as follows

Equation 2.3.2.2-6

$$\begin{bmatrix} P & 0 & 0 & 0 & -(h_1^2+k_1^2) & -l_1^2 \\ 0 & Q & 0 & 0 & -(h_2^2+k_2^2) & -l_2^2 \\ 0 & 0 & R & 0 & -(h_3^2+k_3^2) & -l_3^2 \\ 0 & 0 & 0 & S & -(h_4^2+k_4^2) & -l_4^2 \\ \dfrac{(h_1^2+k_1^2)}{P} & \dfrac{(h_2^2+k_2^2)}{Q} & \dfrac{(h_3^2+k_3^2)}{R} & \dfrac{(h_4^2+k_4^2)}{S} & 0 & 0 \\ \dfrac{l_1^2}{P} & \dfrac{l_2^2}{Q} & \dfrac{l_3^2}{R} & \dfrac{l_4^2}{S} & 0 & 0 \end{bmatrix} \cdot \begin{bmatrix} p \\ q \\ r \\ s \\ A \\ C \end{bmatrix} = \begin{bmatrix} -P \\ -Q \\ -R \\ -S \\ 0 \\ 0 \end{bmatrix}$$

Equation 2.3.2.2-7

$$\begin{bmatrix} p \\ q \\ r \\ s \\ A \\ C \end{bmatrix} = \begin{bmatrix} P & 0 & 0 & 0 & -(h_1^2+k_1^2) & -l_1^2 \\ 0 & Q & 0 & 0 & -(h_2^2+k_2^2) & -l_2^2 \\ 0 & 0 & R & 0 & -(h_3^2+k_3^2) & -l_3^2 \\ 0 & 0 & 0 & S & -(h_4^2+k_4^2) & -l_4^2 \\ \frac{(h_1^2+k_1^2)}{P} & \frac{(h_2^2+k_2^2)}{Q} & \frac{(h_3^2+k_3^2)}{R} & \frac{(h_4^2+k_4^2)}{S} & 0 & 0 \\ \frac{l_1^2}{P} & \frac{l_2^2}{Q} & \frac{l_3^2}{R} & \frac{l_4^2}{S} & 0 & 0 \end{bmatrix}^{-1} \cdot \begin{bmatrix} -P \\ -Q \\ -R \\ -S \\ 0 \\ 0 \end{bmatrix}$$

The unknown parameters (p, q, r, s, A, C) were deduced by performing the calculations using Mathcad® software from MathSoft Inc. The d_{hkl} of the {(004), (224), (115), and (335)} reflections were used, according to the refinement method, to determine the lattice parameters of the samples. The lattice parameter of GaAs was taken to be 5.6533 Å.[105] The lattice parameters were compared with electron diffraction results.

2.4. Transmission Electron Microscopy

2.4.1. Microscope Parameters and Sample Preparation Procedure

All electron imaging and electron diffraction data were obtained with a Philips CM-12 electron microscope operating nominally at 120 kV. Compositional profiles were obtained with energy dispersive X-ray (EDX) spectroscopic analysis using a FEG JEOL-2010F scanning tunneling electron microscope operating at 200 kV with LINK EDX analyzer controlled by Oxford

instrument ISIS software. Regions of known composition were used as a standard to convert the counts to atomic percent.

Cross-sectional samples were prepared by standard polishing[106] and ion-milling using 4 kV Ar^+ at ± 4°. To quantify the number of misfit dislocations (MDs) over a large length scale, the bevel-polish and cleavage (BPC) sample preparation method developed by Spiecker et al.[107] was used along with weak-beam dark-field (WBDF) analysis. Specimens were prepared by back-side polishing and front-side ion milling using 3 kV Ar^+ at 8° with continuous sample rotation. They were cleaved along [110] directions and mounted on a copper ring to investigate MDs terminating at the edge of the sample.

2.4.2. Polarity Determination by Electron Diffraction

A short description of CBED based on the practical experiment of Taftø and Spence[93] and theoretical description of Spiecker[94] will be given. The polarity analysis is based on the interference of beams from two scattered beam paths inside the crystal; e.g. the single scattering of 0 0 0 → 0 0 2 of the direct beam in the weak 0 0 2 reflection and the double-scattering of 0 0 0 → h k l → 0 0 2 via the h k l high reflection. The phase changes of the n-fold scattering in the thin crystal approximation is

Equation 2.4.2-1
$$\omega = -\frac{n\pi}{2} + \sum_{i=1}^{n} \phi(\Delta \mathbf{g}_i) \qquad [93]$$

where $\Delta\mathbf{g}_i = \mathbf{g}_i - \mathbf{g}_{i-1}$ is the reciprocal lattice vector involved in the i^{th} scattering event $(\mathbf{g}_{i-1} \rightarrow \mathbf{g}_i)$ and $\phi(\Delta\mathbf{g}_i)$ is the phase of the corresponding structure amplitude. The minus sign in the term $-\frac{n\pi}{2}$ results from the proper crystallographic sign convention where the weaker scattering atom (e.g., Ga in GaAs or GaSb) is placed at the origin and its equivalent sites and the stronger scattering atom (e.g., As or Sb in GaAs and GaSb) is located at (1/4, 1/4, 1/4) and its corresponding equivalent positions.[94] From Equation 2.4.2-1, the phase changes of the single (ω^s) and double (ω^d) scattering events are

Equation 2.4.2-2
$$\omega^s = -\pi/2 + \phi(0\ 0\ 2)$$
$$\omega^d = -\pi + \phi(h\ k\ l) + \phi(-h\ -k\ \ 2-l)$$

Here the special case of GaAs is treated and the InP case is referred to Ref. [94]. The structure factor in an FCC structure can be written as

Equation 2.4.2-3 $$F_{GaAs} = \left\{f_{Ga} + f_{As}e^{(i\pi/2)(h+k+l)}\right\}\left\{1 + e^{i\pi(h+k)} + e^{i\pi(h+l)} + e^{i\pi(k+l)}\right\}$$ [108]

If h, k, and l are mixed even and odd numbers, the second term will always be zero and the structure amplitude vanishes. Table 2.4.2-1 shows the four different expressions of structure factor and their phases for GaAs when h, k, and l are all even or odd. The small difference of the atomic scattering factor of Ga (Z = 31) and As (Z = 33) will result in a phase $\phi(h\,k\,l) \cong \pm\pi/4$.

The phase relationship of single-scattered wave (0 0 0 → 0 0 2) and the double-scattered wave (0 0 0 → h k l → 0 0 2) are

Equation 2.4.2-4

$$\omega^s \approx -\omega^d \text{ for } h+k+l = 4m+1$$
$$\omega^s \approx \omega^d \text{ for } h+k+l = 4m+3$$

where m is an integer number.

Table 2.4.2-1: The structure factor and its phase for GaAs when *h*, *k*, and *l* are all even or odd. (m is an integer number.)

$h+k+l$	F(h k l)	$\phi(h\,k\,l) = \angle F(h\,k\,l) = \tan^{-1}(\frac{f_{Ga}}{f_{As}})$
4m	$4(f_{GaA} + f_{As})$	0
4m+1	$4(f_{GaA} + if_{As})$	$\approx \pi/4$
4m+2	$4(f_{GaA} - f_{As})$	π
4m+3	$4(f_{GaA} - if_{As})$	$\approx -\pi/4$

If $h+k+l = 4m+1$, the beam interference of single and double scattering paths is destructive. In contrast, for $h+k+l = 4m+3$, the single and double scattering paths will interfere constructively and the intensity of the 0 0 2 reflection will be increased by the *hkl* excitation. When both 0 0 2 and high index reflection of *hkl* are excited, due to symmetry, another high index reflection of *h k 2-l* is also excited. This will result in a double scattering path of 0 0 0 → h k 2-l → 0 0 2. The type of the interference (destructive or constructive) of a singly- or doubly-scattered beam and the type of reflection is determined by the contrast of the *h k l* Kikuchi lines in the 0 0 2 diffraction disc. Figure 2.4.2-1 depicts the destructive and constructive interference of singly-scattered and doubly-scattered beams in GaAs. The sample was prepared with the [110] axis perpendicular to the cross-

section and was maintained at -172 °C during the measurement. If the constructive and destructive interference are not as expected it means that the wrong orientation had been chosen. Note that the microscope was calibrated[109] with MoO_3 to avoid any misinterpretation due to the rotation of the image and diffraction space as the magnification changes.

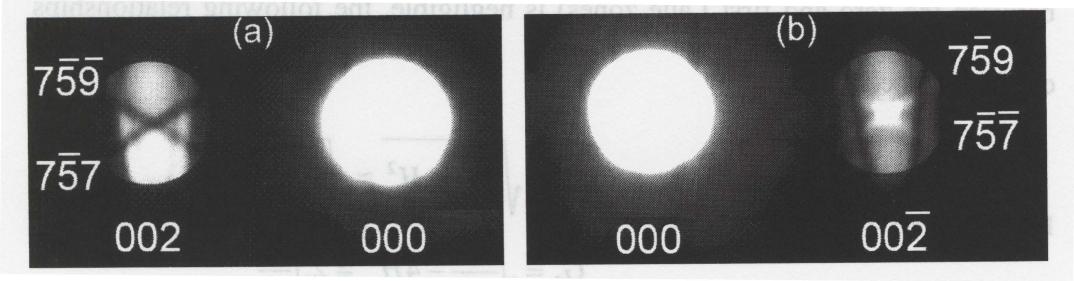

Figure 2.4.2-1: Destructive (a) and constructive (b) interference of singly- and doubly-scattered beams in GaAs. The [110] axis was perpendicular to the cross section specimen.

2.4.3. Determination of Lattice Parameters by Selective Area Electron Diffraction

Electron diffraction (ED) was employed to confirm the lattice constants obtained with X-ray diffraction. Moreover, ED can be used to calculate the lattice constant of tilted epilayers, with respect to the substrate, in the absence of a triple axis X-ray diffractometer. High energy electrons satisfy the conditions for atomic scale measurements. Compared to X-rays, the relativistic electron wavelength is 0.0335 Å at 120 keV and therefore the Bragg angles are very small. Electrons scatter (scattering can be elastic/inelastic and coherent/incoherent) within matter and these interactions require the sample to be transparent to the electron beam.

The thinning process restricts the practical application of TEM for electron diffraction (ED) measurements. Lattice constant determination via electron diffraction has been proposed by measuring the diameter of the first-order Laue zone ring (FOLZ) with CBED.[110, 111] Based on the geometry of the Ewald sphere construction (Figure 2.4.3-1) and assuming that H^2 (where H is the spacing between the zero and first Laue zones) is negligible, the following relationships can be deduced

Equation 2.4.3-1

$$G_1 = \sqrt{\frac{2H}{\lambda} - H^2} \cong \sqrt{\frac{2H}{\lambda}}$$
$$G_2 = \sqrt{\frac{4H}{\lambda} - 4H^2} \cong 2\sqrt{\frac{H}{\lambda}}$$

where G_n is the radius of the n_{th} Laue zone measured in reciprocal space. H is then determined in real-space units (H^{-1}) according to the following equation

Equation 2.4.3-2

$$\frac{1}{H} = \left(\frac{2}{\lambda}\right)\left(\frac{\lambda L}{r}\right)^2 \qquad [112]$$

where λ, L, and r are electron wavelength, camera length, and the measured radius of the Kossel ring of the FOLZ, respectively. Due to its quadratic dependence, this method requires accurate determination of camera constant (λL), electron wavelength (λ), and accurate measurement of the diameter of the Kossel ring. Moreover, if the ring is too large, the measurements will suffer from lens distortion.

H^{-1} is related to magnitude of the real-space direction vector through

$$\frac{1}{H} = \|[UVW]\|$$

where $[UVW]$ is the beam direction.

In a general orthorhombic crystal system where $a_x \neq a_y \neq a_z$, H^{-1} is given by

Equation 2.4.3-3
$$\frac{1}{H} = \left(a_x^{\,2}U^2 + a_y^{\,2}V^2 + a_z^{\,2}W^2\right)^{1/2} \qquad [112]$$

Since a tetragonal structure $(a_x = a_y \neq a_z)$ was assumed, two different zone axes CBED are needed to determine a_x and a_z.

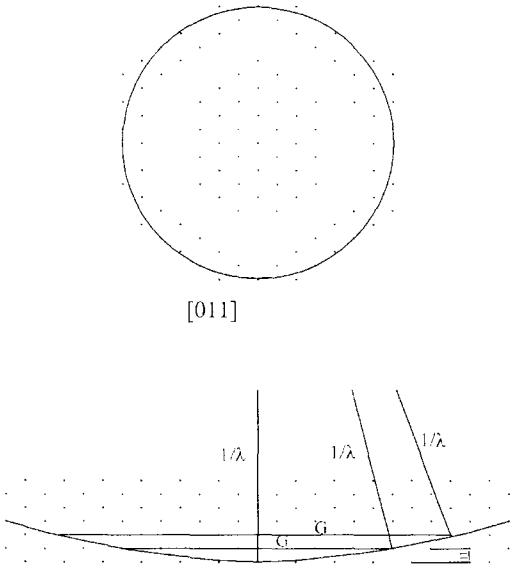

Figure 2.4.3-1: Schematic diagram of Ewald Sphere intersecting with reciprocal lattice points in ZOLZ and FOLZ in electron diffraction. The upper and lower diagrams show the top and cross-sectional view, respectively.

Instead, a method based on selected-area electron diffraction (SAD) and Fatemi's refinement technique[104] was used. Cross-sectional samples were taken in the vicinity of the previous X-ray scan area. A two beam diffraction condition was set for each diffraction spot and the exact Bragg condition was verified by the

Kikuchi lines crossing the centre of the diffraction spot. All of the 004, 111, 220, 331, 113 diffraction patterns were recorded on photographic plate with minimum exposure time to minimize the size of the spots. Figure 2.4.3-2 shows an example of the SAD pattern of the $In_{0.42}Ga_{0.58}As$ metamorphic substrate layer grown on a LT-$In_{0.48}Ga_{0.52}P$ layer (Table 3.4.2-1 (a)). The 333 diffraction spot was excited to minimize the error due to the measurement reading R.

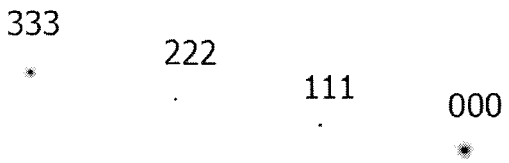

Figure 2.4.3-2: SAD pattern of $In_{0.42}Ga_{0.58}As$ metamorphic substrate layer grown on a LT-$In_{0.48}Ga_{0.52}P$ layer (Table 3.4.2-1 (a)). The 333 diffraction spot was excited to decrease the errors that might occur during the measurement reading.

The maximum practical magnification (L=1.1 m) was used to minimize the contribution of the errors from distance reading, R, in d-spacing according to the following equation

Equation 2.4.3-4 $$Rd = \lambda L \Rightarrow \partial d = -\frac{\lambda L}{R^2}\partial R$$

The camera constant (λL) was calibrated for each substrate separately based on five different Bragg conditions from the GaAs substrate and λL was considered constant after the calibration. The separation of the direct and diffracted beams, R, on the film were measured within two decimal points with a circular film

measuring instrument.[113] Table 2.4.3-1 shows the calibration data on GaAs substrate for the sample with the structure in Table 3.4.2-1 (a).

Table 2.4.3-1: λL calibration data based on the diffraction conditions on a GaAs substrate for the sample with the structure shown in Table 3.4.2-1 (a). The corresponding lattice constant for the $In_{0.42}Ga_{0.58}As$ metamorphic layer is reported in Table 3.4.3.2-1 (a). The lattice parameter of GaAs was taken to be 5.6533 Å.[105]

hkl	d_{hkl} *(Å)*	*Measured* R_{hkl} *(mm)*	λ·L *(mm·Å)*
004	1.4133	25.30	35.76
022	1.9987	17.79	35.56
111	3.2639	10.96	35.77
133	1.2969	27.61	35.81
113	1.7045	20.80	35.45
			35.67 ± 0.14

2.5. Atomic Force Microscopy

Atomic Force Microscopy (AFM) was used to measure the surface QD layer features of the sample structure. A MultiMode® Digital Instruments scanning probe microscope was employed in Tapping Mode™. A standard Si cantilever was used with a tetrahedral tip manufactured by Olympus (OMCL-AC160TS). The tips had aluminum coating on the reflex side with $k_0 = 42$ (N/m) and $f_0 \cong 300$ (kHz), where k_0 and f_0 are force constant and resonant frequency, respectively. A schematic diagram of the tip is shown in Figure 2.5-1.

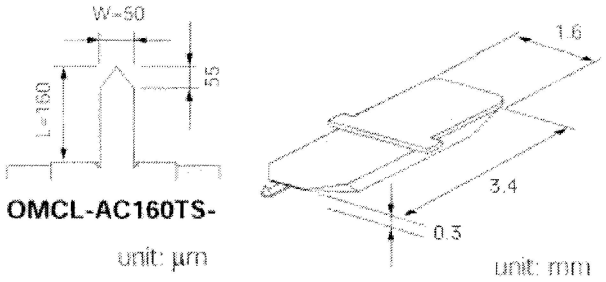

Figure 2.5-1: Schematic diagram of an Olympus (AC160TS) Si Cantilever. Courtesy of Asylum Research Product Guide.

2.5.1. Image Processing

Height distributions were extracted by NanoScope Ver. 7.30 provided by Veeco Instruments Inc. To extract lateral size distribution of the QDs, the AFM images were processed with ImageJ.[114] The AFM images were flattened after an in-plane fit and were exported in Joint Photographic Experts Group (JPEG) format in black and white background. The size of the image was then calibrated based on the actual AFM scan area. The border of the QDs versus the background was set based on the contrast in the black and white image according to Figure 2.5.1-1.

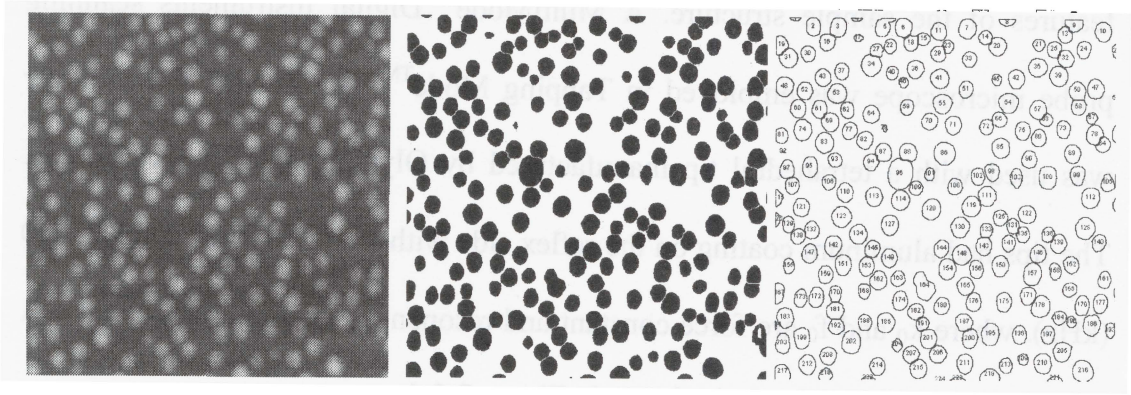

Figure 2.5.1-1: Left: grey scale AFM image, centre: processed AFM image with the QDs in white background, and right: QDs are counted and the border lines are highlighted.

The QD density was calculated according to scan size and number of the QDs (QDs on the edge of the images were counted half since they were shared by neighbouring images). The circularity of the QDs was determined to be close to unity thus they were assumed to be circular. The diameter was correlated to the area of the QDs. This was then graphed to yield the lateral diameter size distribution. Almost all the data are graphed based on three different scan areas. Figure 2.5.1-2 shows an example of the lateral diameter distribution.

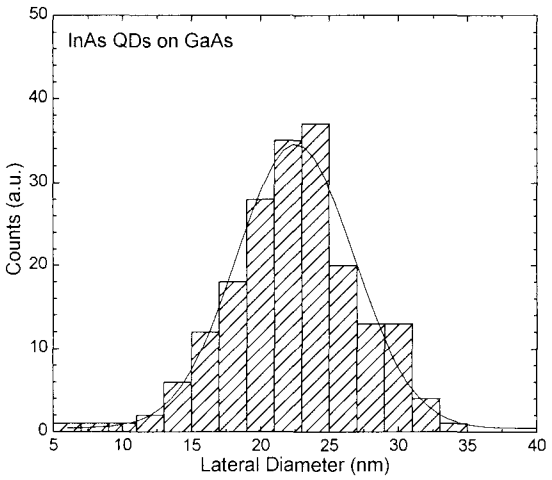

Figure 2.5.1-2: The lateral size distribution with a Gaussian fit of InAs QDs on GaAs substrate. The data are superimposed from three separate scan areas on the sample.

2.6. Photoluminescence

The samples were optically excited using an Argon ion laser (λ = 488 nm). The photoluminescence (PL) spectra were collected via an ABB Bommem MB-160 Fourier Transform Infra-Red (FTIR) spectrometer with an InGaAs detector. The cut-off wavelength of the InGaAs detector is close to 1.6 μm; therefore, the

PL spectra from samples emitting close to this range might not be symmetrical due to this cut-off. After AFM scans, the top QD layer was removed by first exposing the surface to UV-ozone for 20 min, then etching with Buffered-HF for 30 sec. The top $In_xGa_{1-x}As$ layer was then removed by etching in 1 H_2SO_4: 8 H_2O_2: 80 H_2O for 30 sec for the PL measurements.

2.7. Etch Pit Density

To verify the threading dislocation density, the etch pit density was determined using A-B etch (named after Abrahams-Buiocchi).[115] The etchant solution was added in the following order 10 ml H_2O: 40 mg $AgNO_3$: 5 gr CrO_3: 5 ml HF. For the MSLs with high In content, this etchant was not useful. For higher In content $In_xGa_{1-x}As$ (x = 0.3 - 0.4), the etch was changed to 1 H_3PO_4: 1 H_2O_2 under illumination[116] or 1 NH_4OH: 1 H_2O_2: 1 H_2O. Alternative etching solutions are reviewed by Clawson.[99]

Chapter 3 Growth and Characterization of $In_xGa_{1-x}As$ ($0.00 \leq x \leq 0.42$) Metamorphic Pseudo-substrates on Singular* (001) GaAs Wafers

3.1. Introduction

Metamorphic pseudo-substrate layers can be used to overcome the limited availability of elemental and binary substrate lattice constants which consequently limits the available compositional range of high quality crystalline layers that can be grown on top of these substrates. The practical approach is to grow buffer layers between the substrate and the MSL which confine the dislocations within these underlying buffer layers.[117] An ideal MSL should be compatible with the growth conditions of device structure layers, be completely relaxed without propagating threading dislocations into the active region of subsequent devices and have acceptable surface morphology. Figure 3.1-1 shows a <110> cross sectional TEM image of an $In_{0.21}Ga_{0.79}As$ metamorphic substrate (Table 3.1-1) showing that dislocations are confined in metamorphic layers and no dislocations are observed threading inside the top MSL layer. To verify that this confinement is spread over larger areas, an Abrahams-Buiocchi etch[115] was done (for 3 min) on the surface of a 6×6 mm^2 sample. No etch pits were observed under an optical

* A singular crystallographic surface is a plane on which all the surface atoms (with dangling bonds) lie in a single geometrical plane. In a vicinal surface, the atoms with dangling bonds do not lie in one single plane. Therefore, vicinal surfaces can be resolved into atomic scale singular surfaces.

microscope (300×); (this etch duration revealed visible etch pits on other samples with different structures).

Table 3.1-1: Structure of step-graded $In_{0.21}Ga_{0.79}As$ metamorphic substrate.

$In_{0.21}Ga_{0.79}As$	500 nm	Si-doped (1×10^{18} cm^{-3})	terminal layer
$In_{0.22}Ga_{0.78}As$	100 nm		
$In_xGa_{1-x}As$ (x=0.04 to 0.20)	100 nm/step	Si-doped (1×10^{18} cm^{-3})	metamorphic buffer
$In_{0.02}Ga_{0.98}As$	100 nm		
GaAs	100 nm	Si-doped (1×10^{18} cm^{-3})	
n-GaAs substrate			

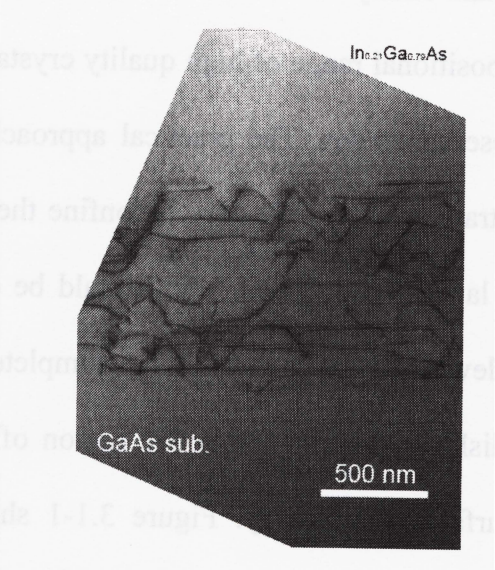

Figure 3.1-1: A <110> cross-sectional TEM image of an $In_{0.21}Ga_{0.79}As$ metamorphic substrate showing that dislocations are confined in metamorphic layer and none are threading inside the top layer. Based on the TEM sampled area, the threading dislocation density should be less than 1×10^{8} cm^{-2}. An A-B etch was done on a 6×6 mm^2 surface area to make sure that dislocation confinement is observed over a large area.

3.2. Strain and Strain Relaxation in Semiconductors

3.2.1. Strain

Throughout this work, we will consider the growth of coherent and incoherent epitaxial layers (unstrained bulk lattice constant = a_e) along [001]

direction on a thick (001) oriented substrate (lattice constant = a_s). For a thick substrate and a fully coherent growth, it is reasonable to assume that almost all the strain is applied to the epilayer; i.e. the in-plane lattice constant, $a_{\parallel}$, of the epilayer equals the substrate lattice constant, a_s (Figure 3.2.1-1). In response to in-plane strain, the epilayer goes through a tetragonal distortion along the growth direction. The net strains in the layer plane, $\varepsilon_{\parallel}$, and along the growth direction, $\varepsilon_{\perp}$ are given by

Equation 3.2.1-1
$$\varepsilon_{\parallel} = \varepsilon_{xx} = \varepsilon_{yy} = \frac{a_s - a_e}{a_s}, \text{ and } \varepsilon_{\perp} = -\frac{2\sigma}{1-\sigma}\varepsilon_{\parallel}$$

where σ is the Poisson ratio which is approximately 1/3 for a tetrahedral semiconductor. Note that $\varepsilon_{xx} = \varepsilon_{yy}$ in coherent systems. Author is not aware of any systematic research to show that this equality is valid in relaxed incoherent systems.

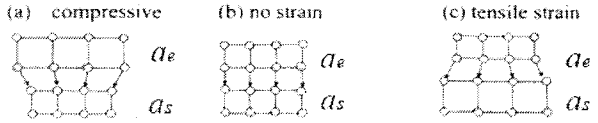

Figure 3.2.1-1: Schematic diagram of an epilayer under (a) compressive strain, (b) no strain, and (c) tensile strain on a substrate with a lattice constant a_s.

3.2.2. Critical Thickness

Sufficiently thin strained layers are thermodynamically stable. This is due to the linear proportionality of the elastic strain energy ($E_{strain} \propto h$) and weaker dependence of dislocation energy ($E_{disl.} \propto \ln(h)$) with the film thickness (Figure

3.2.2-1). For thicker films, the system usually achieves stability through energy release mechanisms like nucleation and/or multiplication of dislocations. A critical thickness, h_c, is defined as the thickness below which the strained layer is expected to be in a thermodynamically stable state. Above h_c, it is energetically favourable to relieve strain via dislocation generation and multiplication. The stability of the strained layer using a continuum model was first studied by Frank and van der Merwe.[66]. The energy stored per unit area, E_{strain}, increases linearly with layer thickness, h. However, the energy required to nucleate a dislocation is large (it involves breaking a line of bonds); and once the dislocation nucleates, the energy increases slowly with epilayer thickness, as $\ln(h)$, according to Figure 3.2.2-1. Voisin[118] calculated the critical layer thickness according to

Equation 3.2.2-1
$$h_c = \left(\frac{1-\frac{\sigma}{4}}{4\pi(1+\sigma)} \right) b\varepsilon_{\parallel}^{-1} (\ln(\frac{h_c}{b}) + \theta)$$

where b is the dislocation Burgers vector (≅ 4 Å), θ is a constant (≅ 1) reflecting the dislocation core energy and σ is the Poisson ratio. Since it is difficult to calculate the critical thickness, as a rule of thumb if the strain-thickness product, εh_c, is less than approximately 200 %Å (where h_c and ε are in Å and percent, respectively), there will be no degradation of optical and electrical properties of layer. A more in-depth review of dislocations and their interaction will be presented in later sections. A more comprehensive review of the subject can be found in Refs. [33, 119, 120, 121].

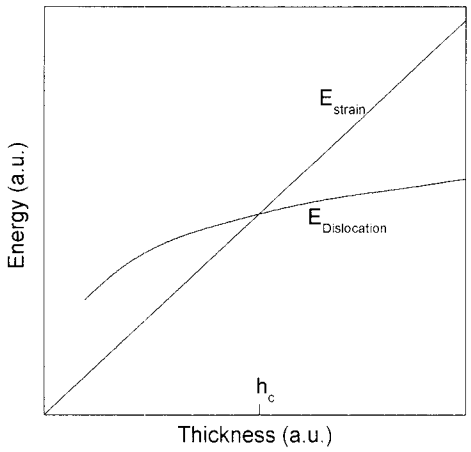

Figure 3.2.2-1: The elastic strain energy increases linearly with layer thickness but the energy of misfit dislocation rises very slowly. Below h_c the strained layer is thermodynamically stable.[121]

3.3. Formation of Dislocations at Heterointerfaces

Zincblende structures have four {111} glide planes each with three <110> slip directions for a total of 12 slip systems. In the (001) substrate, 60° MDs are aligned along two orthogonal <110> directions and glide into the plane of the interface to relieve strain. These two sets of orthogonal MDs are equivalent in diamond structure (Si and Ge). However, the [110] and $[1\bar{1}0]$ directions are crystallographically asymmetrical in zincblende materials.[95, 122, 123] The [110] and $[1\bar{1}0]$ directions are defined as group III (β or $Ga_{(glissile)}$ dislocations) and V (α or $As_{(glissile)}$ dislocations) dangling bond directions on the (001) surface, respectively.[92, 122, 124, 125] Refer to Figure 2.2-1 for bond directions. Figure 3.3-1 shows the schematic diagram of 60° MD dislocations and their Burgers vector for compressive and tensile layers.

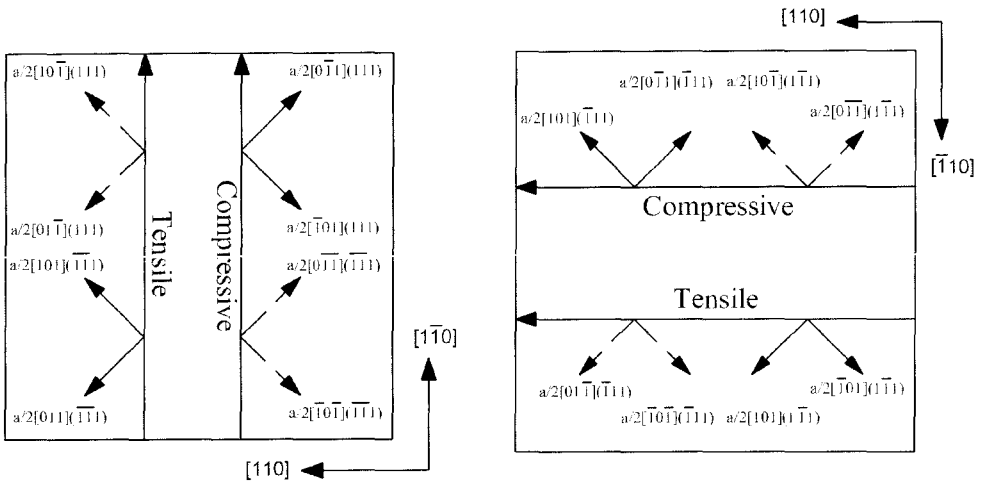

Figure 3.3-1: Schematic diagram of 60° MD dislocations and their Burgers vector for layers in compression and tension. The solid lines show the Burgers vector out of plane and the dashed lines show the BV into the plane. Refer to Figure 2.2-2 for the directions and plane notations.

All metamorphic substrates discussed in this thesis are in a compressive state. The asymmetry (onset of nucleation/multiplication in two perpendicular directions and lateral dislocation density) in α and β dislocations has been correlated[122] to the different velocities (Peierls barriers[98]) of group III and V dislocations.[98, 124, 126] However, there is a controversy on this issue in the literature. Fox and Jesser[98] report that Ga(g) dislocations have a lower Peierls barrier and generate dislocations faster which is in contrast with Choi et al.[127] and Warren et al.[125] who reported that As(g) dislocations have higher mobilities. Note that the lengthening of a misfit dislocation in the interface by glide on its glide plane depends on the mobility, and the asymmetry is mainly due to differences in the nucleation and/or multiplication processes of α and β dislocations. Since the heterostructures were grown on a *singular* (001) substrate, and the tilt was mainly

about $[1\bar{1}0]$ toward [110], any discussion on the tilt as a result of miscut will be ignored and the focus of our discussion will be on the formation and multiplication of MDs.

Frank's rule[128] states that the elastic energy of a dislocation is proportional to the square of the magnitude of its Burgers vector according to the following equation

Equation 3.3-1 $$E_{el} = \alpha G b^2$$

Thus, dislocations with [001] BV are less favoured compared to a perfect dislocation, $1/2\langle 110\rangle$. Perfect dislocations gain their name since they leave behind a perfect crystal after their glide on {111} slip planes. Slip on {111} close packed planes in <110> directions occurs through the movement of the atoms in the nearby "valleys" in zigzag motion. In vector notation, this means that every perfect dislocation will dissociate into two partial dislocations. These dislocations are coined partial dislocations since the first dislocation leaves behind a stacking fault and the tailing dislocation completes the fault and turns the crystal into a perfect one. The dissociation happens according to the following vector equation

Equation 3.3-2 $$\frac{1}{2}\langle 110\rangle \rightarrow \frac{1}{6}\langle 211\rangle + \frac{1}{6}\left\langle 12\bar{1}\right\rangle$$

Frank's rule shows that the splitting reaction is energetically favourable. It has also been shown that the dislocations dissociate in III-V compounds and the stacking fault energy was correlated to the ionicity of the crystal.[129] Partial misfit dislocations are either 30° or 90° depending on the angle that BV makes with the

dislocation line. The best way to visualise the dislocations and their BV is through Thompson tetrahedron.[130]

De Cooman and Carter[131] have shown that the sequence of the partial dislocation is dictated by the position of the extra half plane associated with 60° MD dislocation. For layers under tension, the 90° partial dislocation is closer to the hetero-interface than the 30° partial dislocation. This sequence reverses in the compressive layers. The separation of partial dislocations is strongly affected by the stacking fault energy and the force acting on the partial dislocation. Table 3.3-1 shows the perfect dislocation, partial dislocation, and the Schmidt factor for a layer under compression. The Schmidt factor changes sign for a layer under tension. Since the samples in this work were grown under compression, only the compressive case is considered.

It is evident that the compressive stress in xx and yy direction translates a larger force on the 90° partial than that of the 30° partial dislocation. Since the 90° partial is the trailing dislocation in compressive layers and is subjected to a larger force it will trail closer to the 30° partial. This means that the stacking fault is smaller compared to a fault in a tensile layer where a 90° partial trails ahead of 30° partial. This has been verified by De Cooman and Carter.[131]

Table 3.3-1: Schmidt factor, m, for the partial dislocations formed by dissociation of perfect dislocation. The Schmidt factor is larger for the 90° partial dislocation.

Perfect Dislocation	Partial Dislocation	Dislocation line	Type of partial	m_{xx}: Schmidt factor σ_{xx} $[\bar{1}00]$	m_{yy}: Schmidt factor σ_{yy} $[0\bar{1}0]$	$m=m_{xx}+m_{yy}$
$\frac{a}{2}[0\bar{1}1](111)$	$\frac{a}{6}[\bar{1}\bar{1}2](111)$	$[1\bar{1}0]$	90°	-0.236	-0.236	-0.471
	$\frac{a}{6}[\bar{1}2\bar{1}](111)$	$[\bar{1}\bar{1}0]$	30°	+0.236	-0.471	-0.236
$\frac{a}{2}[\bar{1}01](111)$	$\frac{a}{6}[\bar{1}\bar{1}2](111)$	$[\bar{1}\bar{1}0]$	90°	-0.236	-0.236	-0.471
	$\frac{a}{6}[\bar{2}11](111)$	$[\bar{1}\bar{1}0]$	-30°	-0.471	+0.236	-0.236
$\frac{a}{2}[0\bar{1}\bar{1}](\bar{1}\bar{1}1)$	$\frac{a}{6}[\bar{1}2\bar{1}](\bar{1}\bar{1}1)$	$[\bar{1}\bar{1}0]$	30°	-0.236	+0.471	+0.236
	$\frac{a}{6}[\bar{1}\bar{1}2](\bar{1}\bar{1}1)$	$[\bar{1}\bar{1}0]$	90°	+0.236	+0.236	+0.471
$\frac{a}{2}[10\bar{1}](\bar{1}\bar{1}1)$	$\frac{a}{6}[2\bar{1}\bar{1}](\bar{1}\bar{1}1)$	$[\bar{1}\bar{1}0]$	-30°	+0.471	-0.236	+0.236
	$\frac{a}{6}[\bar{1}\bar{1}2](111)$	$[110]$	90°	+0.236	+0.236	+0.471
$\frac{a}{2}[101](\bar{1}11)$	$\frac{a}{6}[211](111)$	$[110]$	30°	-0.471	+0.236	-0.236
	$\frac{a}{6}[\bar{1}\bar{1}2](\bar{1}11)$	$[110]$	90°	-0.236	-0.236	-0.471
$\frac{a}{2}[0\bar{1}1](\bar{1}11)$	$\frac{a}{6}[\bar{1}\bar{2}1](\bar{1}11)$	$[110]$	-30°	+0.236	-0.471	-0.236
	$\frac{a}{6}[\bar{1}\bar{1}2](\bar{1}11)$	$[110]$	90°	-0.236	-0.236	-0.471
$\frac{a}{2}[10\bar{1}](111)$	$\frac{a}{6}[\bar{1}\bar{1}2](\bar{1}11)$	$[110]$	90°	+0.236	+0.236	+0.471
	$\frac{a}{6}[2\bar{1}\bar{1}](\bar{1}11)$	$[110]$	30°	+0.471	-0.236	+0.236
$\frac{a}{2}[0\bar{1}\bar{1}](\bar{1}\bar{1}1)$	$\frac{a}{6}[\bar{1}\bar{1}2](\bar{1}11)$	$[110]$	90°	+0.236	+0.236	+0.471
	$\frac{a}{6}[\bar{1}\bar{2}\bar{1}](\bar{1}11)$	$[110]$	-30°	-0.236	+0.471	+0.236

3.4. Tilt and Mosaicitiy

3.4.1. Introduction

In mismatched heteroepitaxial systems, tilt or misorientation of the epilayer relative to that of the substrate has been observed in many material systems including, InGaAs/GaAs,[132, 133] InAlAs/GaAs,[134] InGaSb/GaSb,[135]

InAlAs and InAsP/InP,[136] SiGe/Si,[137] and GaAs/Si.[138, 139] Epitaxial deposition on such tilted layers should be equivalent to growth on off-cut substrates where it has been shown[140] that electrical parameters of laser devices grown on tilted substrates may be improved by increasing the misorientation.

Burgers[141] correlated the nature of the symmetric tilt to the presence of the dislocations at the interface; this was followed by dislocation models at crystal grain boundaries[142] and the observation of dislocations at the boundaries of nearly perfect Ge crystals.[143] Some researchers have observed tilt and proposed various models based on pseudomorphic growth at {001} steps,[132] the presence of 60° MDs at GaAs/Si interface,[139, 144] the preferential glide of certain dislocations in asymmetrical slip systems,[145] and a low-energy route toward accommodation of lattice misfit strain in heterointerfaces.[146]

It has been previously reported,[91] for the growth of an InAsP metamorphic pseudosubstrate on an InP substrate, that the use of a low-temperature grown InP (LT-InP) layer deposited prior to the metamorphic buffer layers can produce improved photoluminescence response in a device structure grown on top of the pseudosubstrate. Also, from work on quantum well intermixing (QWI),[147, 148] low temperature grown InGaP and InP layers grown on top of QW structures (GaAs- and InP-based, respectively) can be used to enhance the process; hence, LT-InGaP and LT-InP contain similar defects. These observations suggested there could be advantages to growing a low-temperature InGaP (LT-InGaP) layer lattice-matched to GaAs underlying a strained, step-graded InGaAs buffer on a singular

(001) GaAs substrate. For this material system, an asymmetric tilt was observed in mismatched heterointerfaces around $[1\bar{1}0]$ toward [110] direction. Weak-beam dark-field electron imaging has been applied to show the imbalance of opposite sign BV MDs. Multiplication and climb mechanisms have been considered as a method for generation of like-sign Burger vector MDs.

3.4.2. Tilt and Mosaicity: Reciprocal Space Maps

Table 3.4.2-1 shows the structure of metamorphic layers for samples with and without LT-$In_{0.48}Ga_{0.52}P$ (250 nm). The growth details and calibration calculations are explained in Chapter 2.

Table 3.4.2-1: Structure of step-graded metamorphic layers for samples with (a) and without (b) LT- $In_{0.48}Ga_{0.52}P$.

(a)

$In_{0.42}Ga_{0.58}As$	500 nm	terminal layer
$In_{0.42}Ga_{0.58}As$	50 nm	
$In_xGa_{1-x}As$ (x=0.04 to 0.40)	20% In/μm - 50 nm/step	metamorphic buffer
$In_{0.02}Ga_{0.98}As$	50 nm	
LT-$In_{0.48}Ga_{0.52}P$	250 nm	
GaAs	100 nm	
n-GaAs substrate		

(b)

$In_{0.42}Ga_{0.58}As$	500 nm	terminal layer
$In_{0.42}Ga_{0.58}As$	50 nm	
$In_xGa_{1-x}As$ (x=0.04 to 0.40)	20% In/μm - 50 nm/step	metamorphic buffer
$In_{0.02}Ga_{0.98}As$	50 nm	
GaAs	100 nm	
n-GaAs substrate		

Figure 3.4.2-1 (a) and Figure 3.4.2-2 (a) show the real space contour map of (004) reciprocal lattice point of the GaAs substrate, the $In_xGa_{1-x}As$ metamorphic buffer layers and the MSL in the [110] direction for samples with and without LT-InGaP, respectively. Figure 3.4.2-1 (b) and Figure 3.4.2-2 (b) depict the scans in $[1\bar{1}0]$ direction. The contours of LT-InGaP layer can be seen in Figure 3.4.2-1 and the slightly larger *d*-spacing indicates that it is under a small amount of compressive strain. It is evident that the $In_{0.42}Ga_{0.58}As$ MSL on the LT-InGaP is ~ 0.9° tilted toward [110] direction with a mosaic spread of around ± 1500 arcsec. The [110] tilt initially increases slowly and at some point during the growth of the metamorphic buffer layers the rate of tilt increases as indicated by change of the slope in the straight lines. In contrast, the (004) planes of the MSL in the $[1\bar{1}0]$ direction tilted by < 0.1 °; hence, they are almost parallel to those in the substrate. In the sample without LT-InGaP (Figure 3.4.2-1 (b)), the growth starts similarly, exhibiting a slowly increasing tilt toward $[\bar{1}\bar{1}0]$ direction, then after partial growth of the metamorphic buffer, the tilt remains constant for the remaining layers. It is noted that the mosaic spread in the epilayers is greater than the spread due to system resolution or sample bending as can qualitatively be seen by comparing the width of substrate peak relative to that of the epilayers. The broadening seen in *d*-spacing is due to varying degrees of relaxation. The same behaviour was observed in the (224), (115), and (335) scans (not shown here).

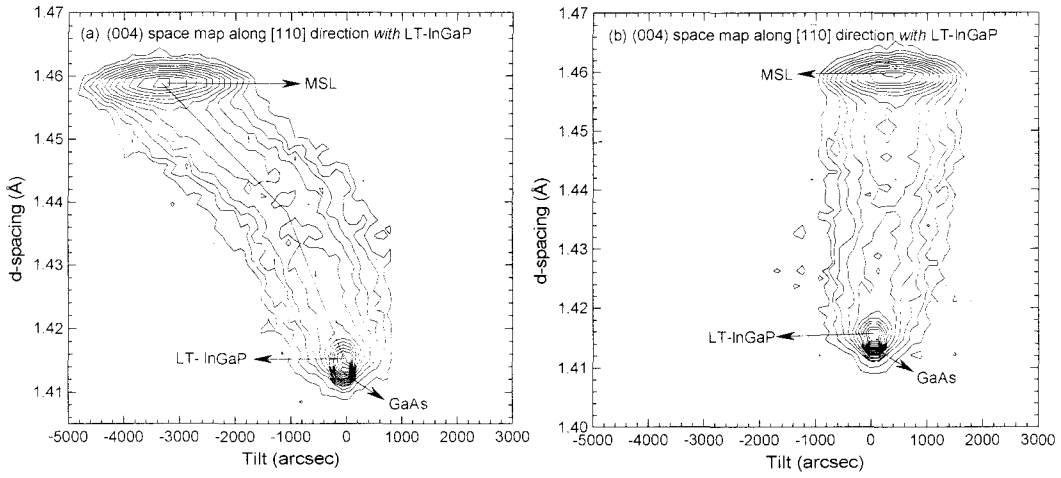

Figure 3.4.2-1: (004) space map of $In_xGa_{1-x}As$ MSL with LT-$In_{0.48}Ga_{0.52}P$ in (a) [110] direction and (b) [1$\bar{1}$0] direction. It is evident that the $In_xGa_{1-x}As$ MSL layer on the LT-$In_{0.48}Ga_{0.52}P$ is ~ 0.9° tilted toward [110] direction. In contrast, the (004) planes of the MSL in the [1$\bar{1}$0] direction are only tilted by < 0.1 ° and are almost parallel to those in the substrate. The contours of LT- $In_{0.48}Ga_{0.52}P$ layer can be seen and the slightly larger d-spacing indicates that it is under a small amount of compressive strain.

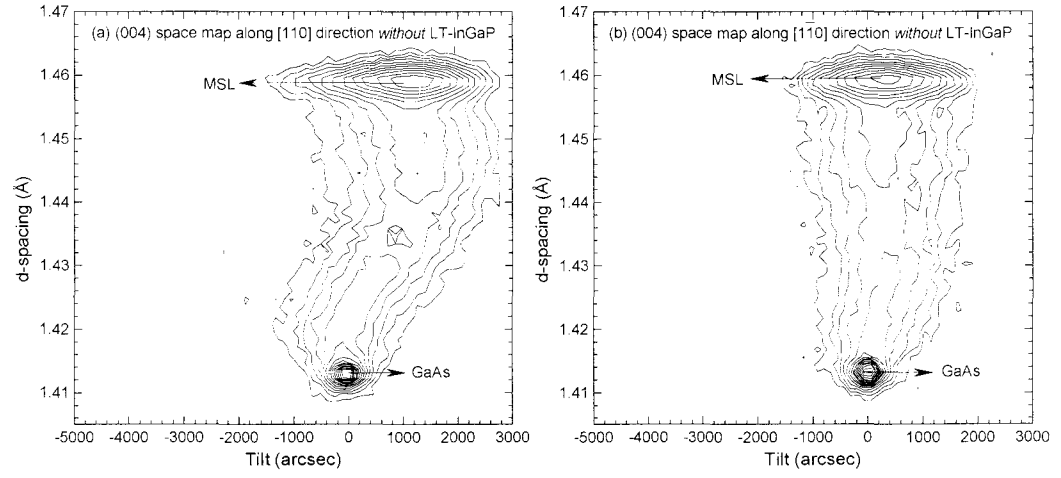

Figure 3.4.2-2: (004) space map of $In_xGa_{1-x}As$ MSL without LT-$In_{0.48}Ga_{0.52}P$ (a) in [110] direction and (b) in [1$\bar{1}$0] direction. The growth starts similarly exhibiting a slowly increasing tilt toward [1$\bar{1}$0] direction, then after partial growth of the metamorphic buffer, the tilt remains constant for the remaining layers.

Heller and Legally[149] showed that GaAs layers (grown by MBE) on a singular GaAs substrate have a multilevel system of terraces. Edges along $[1\bar{1}0]$ (A-type steps) are smooth and slowly meandering while steps parallel to [110] (B-type steps) are kinked suggesting that B steps have a much higher energy. They showed that A-type terraces occupy six or seven levels over a distance of ~ 800 nm in the [110] direction and the B type terraces have one level over a distance of ~ 600 nm along $[1\bar{1}0]$. They correlated the result to the step energy and sticking anisotropy with a preference for sticking at B-type steps[149] possibly due to anisotropic surface migration of Ga atoms on GaAs.[150] Larger mosaic spread in $<110>$ direction compared to that in $<1\bar{1}0>$ direction in both samples (Figure 3.4.2-1 and Figure 3.4.2-2), suggests the same type of asymmetry in the presence of kinks and multilevel-terrace growth front during the growth of $In_xGa_{1-x}As$ metamorphic buffer layers.

3.4.3. Lattice Constant and Relaxation

3.4.3.1. X-ray Diffraction Results

Table 3.4.3.1-1 shows the calculated d_{hkl} for the MSL obtained from the space maps for different sets of planes. Each data point is an average of both glancing incidence and exit results. The (004) reflection was included in the

calculation of the lattice parameter. The fractional adjustments depict that small changes bring self-consistency.

Table 3.4.3.1-1: Least square adjustments for $In_{0.42}Ga_{0.58}As$ cap layer sample *with* LT-$In_{0.48}Ga_{0.52}P$ (a) and *without* LT-$In_{0.48}Ga_{0.52}P$ (b) taking into account all the measurement including (004) reflection.

(a)

hkl	*Measured* d_{hkl}, *(Å)*	*Measured* $\frac{1}{d_{hkl}^2}$, $(Å^{-2})$	*Adjusted* $\frac{1}{d_{hkl}^2}$, $(Å^{-2})$	Fractional change, (ppm)
004	1.45937	0.46953	0.469493	-84
224	1.18937	0.70691	0.706733	-246
115	1.12312	0.79276	0.792893	163
335	0.8883	1.26716	1.267373	167
a = 5.807 Å, c = 5.838 Å				

(b)

hkl	*Measured* d_{hkl}, *(Å)*	*Measured* $\frac{1}{d_{hkl}^2}$, $(Å^{-2})$	*Adjusted* $\frac{1}{d_{hkl}^2}$, $(Å^{-2})$	Fractional change, (ppm)
004	1.45875	0.46994	0.469903	-70
224	1.18937	0.70691	0.706693	-302
115	1.12275	0.79329	0.793420	160
335	0.88850	1.26673	1.267000	212
a = 5.812 Å, c = 5.835 Å				

The lattice parameters of $In_{0.42}Ga_{0.58}As$ MSL calculated according to the least square criterion were found to be[104]

a = 5.807 Å and c = 5.838 Å (with LT-$In_{0.48}Ga_{0.52}P$)

a = 5.812 Å and c = 5.835 Å (without LT-$In_{0.48}Ga_{0.52}P$)

Due to symmetry of the matrix solution of the set of equations, it was not possible to calculate three separate lattice parameters and verify asymmetry of relaxation in [110] and $[1\bar{1}0]$ directions.[151] However, Nomarski interference photographs (not shown here) of the surface of both samples show that the linear dislocation densities are different in two directions ($n_{\perp[110]} > n_{\perp[1\bar{1}0]}$). This agrees with other data in the literature reporting higher asymmetry in the first stages of the growth of highly strained layers and decreasing the asymmetry (with nucleation and/or multiplication of perpendicular MDs) as the growth proceeds.[151, 152] This observed asymmetry has been correlated[153, 154] to the different velocities (Peierls barriers[98]) of group III and V dislocations[124, 125, 126] However, the lengthening of MDs on the glide plane in the interface depends on their mobility and the asymmetry is mainly due to differences in the nucleation and/or multiplication processes of α and β dislocations rather than their mobilities. This will be discussed in more detail later. The partial relaxation of the terminating $In_{0.42}Ga_{0.58}As$ layer agrees with the current models of Tsao[146] and Tersoff,[155] showing that the equilibrium dislocation density is less than that which would eliminate all the coherency strain. The in-plane lattice constants show that the MSL pseudosubstrate with LT-InGaP is more relaxed due to higher asymmetric tilt which accommodates lattice mismatch without producing long-range stress fields around dislocations.[146]

3.4.3.2. Electron Diffraction Results

Table 3.4.3.2-1 tabulates the separation of direct and diffracted electron beam, R_{hkl}, and their corresponding calculated and adjusted d_{hkl}. The least square criterion results in the following lattice parameters

a = 5.798 Å and c = 5.818 Å (with LT-$In_{0.48}Ga_{0.52}P$)

a = 5.803 Å and c = 5.820 Å (without LT-$In_{0.48}Ga_{0.52}P$)

The fractional changes which bring a consistent answer are an order of magnitude larger than those of the X-ray data. This is due to the fact that the gradients of fractional changes with respect to R are inversely proportional to R^3 according to the following derivation.

Equation 2.3.2.2-3 and Equation 2.4.3-4 can be written as $p = \frac{(h_1^2 + k_1^2)A + l_1^2 C}{P} - 1$ and $\frac{1}{d_{h_2k_1l_1}^2} = \frac{R_{h_2k_1l_1}^2}{\lambda^2 L^2}$, respectively. The gradient of fractional change, p, with respect to R would be as follows

Equation 3.4.3.2-1

$$\frac{\partial p}{\partial R} = \left((h_1^2 + k_1^2)A + l_1^2 C\right) \cdot \left(\frac{-\left(\frac{\partial P}{\partial R}\right)}{P^2} \right) \propto \left(\frac{-\left(\frac{\partial P}{\partial R}\right)}{P^2} \right) \propto \left(\frac{-\left(\frac{\partial \left(\frac{1}{d_{h_1k_1l_1}^2} \right)}{\partial R} \right)}{\frac{1}{d_{h_1k_1l_1}^4}} \right) \propto -\frac{\left(\frac{\partial \left(\frac{R_{h_1k_1l_1}^2}{\lambda^2 L^2} \right)}{\partial R} \right)}{\left(\frac{R_{h_1k_1l_1}^4}{\lambda^4 L^4} \right)} \propto \frac{\left(\frac{-2R_{h_1k_1l_1}}{\lambda^2 L^2} \right)}{\left(\frac{R_{h_1k_1l_1}^4}{\lambda^4 L^4} \right)} \propto \frac{-2\lambda^2 L^2}{R_{h_1k_1l_1}^3}$$

It is evident that even with larger fractional changes, the method converges the measurements to lattice parameters which are 0.15% different from those deduced from X-ray results (Table 3.4.3.1-1). The same set of measurements on another sample (Table 3.4.3.2-1 (b)) resulted in approximately the same order of magnitude in deviation. The calculated lattice parameters based on the combination of two different diffraction conditions (Table 3.4.3.2-2) do not converge to a single solution and have discrepancies compared to X-ray reference data. Arguing in a similar way to Fatemi,[104] averaging the several combinations of the lattice parameters is unjustified due to the fact that they are interdependent variables and will not lead to an accurate result. In the absence of triple axis diffractometry to map tilted epilayers, ED along with the least square criterion of multiple diffraction conditions is an appropriate candidate for lattice parameter determination. Combination of two pairs of diffraction conditions (Table 3.4.3.2-2) and averaging their results will not give reliable sets of lattice constants and are not justified. The determination of lattice constants based on ED is a promising method for samples with smaller volumes which do not yield high intensity reflected X-ray. It should be noted that ED evaluation suffers from localized sampling and will not provide a measure of how much d-spacing fluctuation might be present in the epilayer.

Table 3.4.3.2-1: Separation of direct and diffracted beam and their corresponding d_{hkl} for $In_{0.42}Ga_{0.58}As$ MSL (a) with LT-$In_{0.48}Ga_{0.52}P$ sample ($\lambda \cdot L = 35.67 \pm 0.14 mm$ Å) and (b) without LT-$In_{0.48}Ga_{0.52}P$ sample ($\lambda \cdot L = 35.85 \pm 0.04 mm$ Å).

(a)

hkl	*Measured* R_{hkl}, *(mm)*	*Calculated* d_{hkl}, *(Å)*	*Calculated* $\frac{1}{d_{hkl}^2}$, *(Å^{-2})*	*Adjusted* $\frac{1}{d_{hkl}^2}$, *(Å^{-2})*	*Adjusted* d_{hkl}, *(Å)*	Fractional change, (ppm)
004	24.55	1.4529	0.4737	0.4726	1.4546	-2263
022	17.32	2.0594	0.2358	0.2371	2.0535	5735
111	10.65	3.3492	0.0891	0.0890	3.3515	-1365
133	26.82	1.3300	0.5654	0.5649	1.3305	-795.3
113	20.41	1.7476	0.3274	0.3270	1.7488	-1354
a = 5.798 Å, c = 5.818 Å						

(b)

hkl	*Measured* R_{hkl}, *(mm)*	*Calculated* d_{hkl}, *(Å)*	*Calculated* $\frac{1}{d_{hkl}^2}$, *(Å^{-2})*	*Adjusted* $\frac{1}{d_{hkl}^2}$, *(Å^{-2})*	*Adjusted* d_{hkl}, *(Å)*	Fractional change, (ppm)
004	24.60	1.4574	0.4708	0.4724	1.4550	3392
022	17.51	2.0476	0.2385	0.2369	2.0546	-6821
111	10.70	3.3508	0.0891	0.0889	3.3535	-1627
133	26.95	1.3304	0.5650	0.5641	1.3314	-1619
113	20.42	1.7558	0.3244	0.3265	1.7500	6568
a = 5.803 Å, c = 5.820 Å						

Table 3.4.3.2-2: In-plane and out-of-plane lattice parameters of $In_{0.42}Ga_{0.58}As$ MSL with LT-$In_{0.48}Ga_{0.52}P$ (Table 3.4.2-1 (a)) based on the combination of two different electron diffraction condition results (Table 3.4.3.2-1 (a)). The percentages reported in brackets are the deviations with respect to the corresponding lattice parameter calculated from X-ray results (Table 3.4.3.1-1 (a)).

Reflection combination	in-plane lattice parameter, a (Å)	perpendicular lattice parameter, c(Å)
004 & 111	5.7957 (0.19%)	5.8117 (0.45%)
004 & 022	5.8383 (0.54%)	5.8117 (0.45%)
004 & 133	5.7841 (0.39%)	5.8117 (0.45%)
004 & 113	5.7283 (1.36%)	5.8117 (0.45%)
111 & 220	5.7541 (0.91%)	5.8985 (1.04%)
111 & 133	5.8104 (0.06%)	5.7825 (0.95%)
111 & 113	5.8043 (0.05%)	5.7945 (0.74%)
220 & 133	5.3560 (7.77%)	6.4435 (10.4%)
220 & 113	5.8709 (1.10%)	5.7801 (0.99%)
113 & 133	5.7983 (0.15%)	5.7958 (0.72%)
Ten number average, including 004	5.7540 ± 0.1454 (0.91%)	5.8742 ± 0.2028 (0.62%)
Six number average, excluding 004	5.7323 ± 0.1881 (1.29%)	5.9158 ± 0.2623 (1.34%)

3.4.4. Electron Imaging

The Burgers vector (BV) of 60° MDs can be decomposed to three parts (e.g., $(a/2)[0\bar{1}1] = (a/4)[\bar{1}\bar{1}0] + (a/4)[1\bar{1}0] + (a/2)[001] = \boldsymbol{b}_{misfit} + \boldsymbol{b}_{screw} + \boldsymbol{b}_{tilt}$). For a dislocation along $[1\bar{1}0]$, the misfit component ($(a/4)[\bar{1}\bar{1}0]$) is responsible for relieving misfit in the $[\bar{1}\bar{1}0]$ direction, the screw component ($(a/4)[1\bar{1}0]$) results in local rotation of the epilayer around the [001] direction relative to the substrate, while the tilt component ($(a/2)[001]$) produces a tilt around a dislocation line ($[1\bar{1}0]$) between the epilayer and the substrate. The same concepts

are true for a dislocation along [110]. If all possible slip systems participate in relaxation equally, the tilt components will cancel out vectorially and there will not be any net macroscopic tilt. Our X-ray space maps show that the MSL has a tilt about $[1\bar{1}0]$ toward [110] indicating an imbalance in the population of unlike sign dislocations. This imbalance was verified using the BPC method developed by Spiecker et al.[107] The BV of the dislocations was determined with WBDF imaging developed by Ishida et al.[156] To image MDs which lie along $[1\bar{1}0]$, GaAs/LT-InGaP/InGaAs sample was prepared according to BPC method and was cleaved along the [110] and loaded backside toward the electron beam (close to $[00\bar{1}]$ zone axis) according to Ref. [107]. The sample was tilted about [110] toward $[11\bar{2}]$ zone axis and WBDF images of the $(\bar{1}11)$ reflection with $s_g >> 0$ were obtained. The difference in the number of the thickness fringes around a closed circuit is equal to $\mathbf{g}\cdot\mathbf{b}$ with $\mathbf{g}$ and $\mathbf{b}$ denoting diffraction vector and BV, respectively.[156] The side from which the terminating fringe enters depends on the sign of $\mathbf{g}\cdot\mathbf{b}$ and the sign of excitation error s_g.[107, 156] It should be noted that with a $(\bar{1}11)$ reflection, the image is insensitive to any misfit component of BV ($\mathbf{g}\cdot\mathbf{b}_{misfit} = [\bar{1}\bar{1}1]\cdot\frac{1}{4}[\bar{1}\bar{1}0]$) and only tilt and twist components will interact with fringes. If $\mathbf{g}\cdot\mathbf{b} = 0$ (e.g. dislocations do not terminate the fringe), another

reflection (e.g. {113}) has to be set.[107] But, for statistical purposes, only $(1\bar{1}1)$ WBDF imaging condition was used.

Figure 3.4.4-1 shows the $(1\bar{1}1)$ WBDF image of GaAs/LT-InGaP/InGaAs specimen along the [110] direction. The inset shows the magnified portion of the images and the termination of the fringes. Those MDs terminating from right hand side have $\mathbf{g}\cdot\mathbf{b}>0$. Almost 360 dislocations were counted covering an approximate total length of 300 μm on a slope along [110] direction. The result is summarized in Table 3.4.4-1 and shows an asymmetry in the population of the $1/2[0\bar{1}1](\bar{1}\bar{1}1)$ and $1/2[\bar{1}0\bar{1}](111)$ glide systems. Analyzing in a similar way to Spiecker et al.,[107] an asymmetry is expected for the group of the 153 dislocations of either of the glide systems $1/2[\bar{1}01](\bar{1}\bar{1}1)$ and $1/2[0\bar{1}\bar{1}](111)$. This imbalance in the population of opposite sign tilt component of the BV is in agreement with the crystallographic tilt as revealed by RSM (Figure 3.4.2-1 (a)).

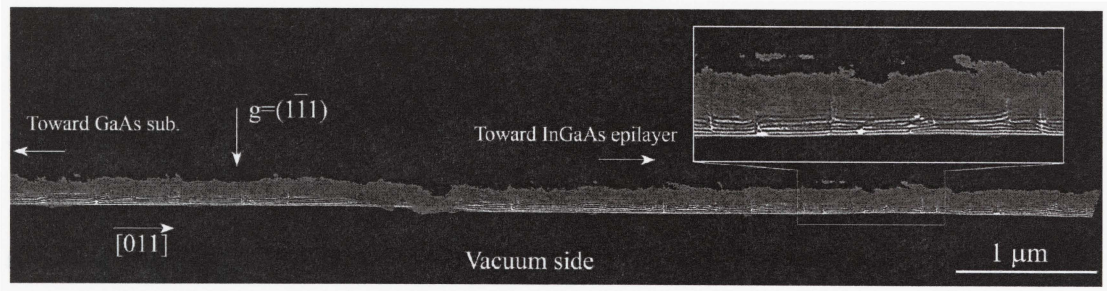

Figure 3.4.4-1: $(1\bar{1}1)$ weak beam dark field images of 60° misfit dislocation of InGaAs/LT-InGaP/GaAs sample along [110] direction. The inset shows the termination of the fringes by misfit dislocation. The sign of the $\mathbf{g}\cdot\mathbf{b}$ is deduced by how the dislocations terminate the thickness fringes.

Table 3.4.4-1: Glide systems and corresponding BV components of misfit dislocation along $[1\bar{1}0]$ and the statistical BV analysis for ~ 300 dislocations of step graded $In_xGa_{1-x}As$ buffer layer with an underlying LT-InGaP layer (Table 3.4.2-1 (a)).

Dislocation Type	Glide System	b_{misfit}	b_{twist}	b_{tilt}	$\mathbf{g}\cdot\mathbf{b}=(\bar{1}\bar{1}1)\cdot\mathbf{b}$	Number of Dislocations
60°	$\frac{1}{2}[0\bar{1}1](\bar{1}\bar{1}1)$	$\frac{1}{4}[\bar{1}\bar{1}0]$	$\frac{1}{4}[1\bar{1}0]$	$\frac{1}{2}[001]$	1	114
	$\frac{1}{2}[\bar{1}01](\bar{1}\bar{1}1)$	$\frac{1}{4}[\bar{1}\bar{1}0]$	$\frac{1}{4}[\bar{1}10]$	$\frac{1}{2}[001]$	0	153
	$\frac{1}{2}[0\bar{1}\bar{1}](111)$	$\frac{1}{4}[\bar{1}\bar{1}0]$	$\frac{1}{4}[\bar{1}10]$	$\frac{1}{2}[00\bar{1}]$	0	
	$\frac{1}{2}[\bar{1}01](111)$	$\frac{1}{4}[\bar{1}\bar{1}0]$	$\frac{1}{4}[\bar{1}10]$	$\frac{1}{2}[00\bar{1}]$	-1	72

$In_xGa_{1-x}P$ ($x \approx 0.5$) may form an ordered structure under specific growth conditions[157] where growth occurs as alternating layers of InP and GaP. If ordering were present, the diffraction pattern would exhibit extra intensity spots at or around the 1/2(111) diffraction spots suggesting an ordering of the atoms on the {111} planes.[158] These structures have been suggested and used to observe the track of misfit dislocations by anti-phase boundaries.[158, 159] The absence of 1/2{111} point in the electron diffraction patterns of LT-InGaP/GaAs sample ruled out the presence of ordering. However, it has been shown that InGaP grown at low temperature (< 300 °C) is P rich, containing P_{In} antisite defects[160, 161] which may dissociate at the growth temperature of the metamorphic layers (525 °C) and P interstitials migrate and interact through the P-As exchange mechanism[162, 163]

leading to interfacial inter-diffusion. To confirm this, a comparison was undertaken of the compositional profile at the LT-InGaP/$In_xGa_{1-x}As$ interface in the current samples with a calibration sample where LT-InGaP layer was grown on GaAs such that this interface was only subjected to the low temperature (245 °C) of the final layer growth. Figure 3.4.4-2 compares the EDX profiles of the underlying LT-InGaP/$In_xGa_{1-x}As$ interface with that of the LT-InGaP/GaAs interface. A broadened interface is seen at the initial interface which results from defect enhanced interdiffusion during the higher temperature MSL growths.

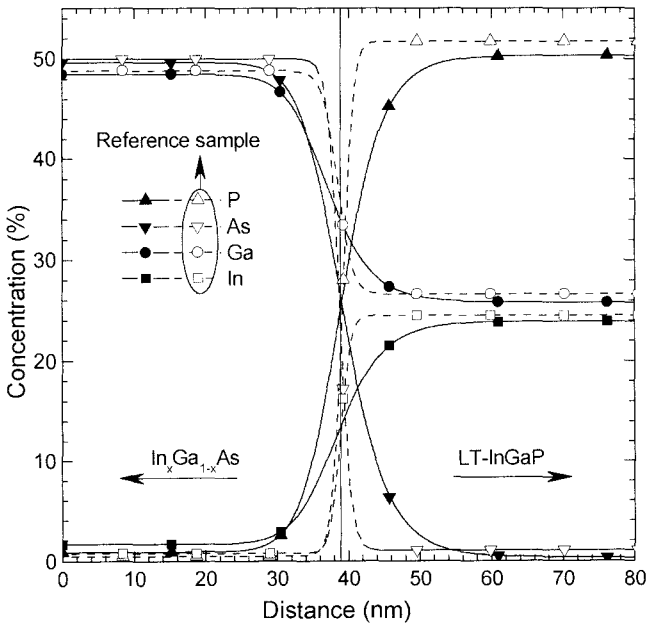

Figure 3.4.4-2: EDX profiles across the LT-InGaP/$In_xGa_{1-x}As$ interface (closed symbols) and LT-InGaP/GaAs reference sample interface (open symbols) showing the As/P and In/Ga exchange inside the step-graded layer. (The profiles are continuous and only selected symbols are shown for identification purposes.)

3.5. Anisotropy of Mosaic Spread in two <110> Crystallographic Directions

Table 3.5-1 shows the layer structure of the metamorphic substrate. The growth details and calibration calculations are explained in chapter 2. Due to partial relaxation of strained layers, in accordance with models by Tsao[146] and Tersoff[155] which show that the equilibrium dislocation density is less than that which would eliminate the entire coherency strain, the terminating layer was grown with a smaller Indium fraction in order to avoid further strain build up.

Table 3.5-1: Structure of step-graded metamorphic substrate. The terminating layer was grown with a smaller In fraction in order to avoid further strain build up.

$In_{0.26}Ga_{0.74}As$	500 nm	Si-doped (1×10^{18} cm^{-3})	terminal layer
$In_{0.30}Ga_{0.70}As$	100 nm		
$In_xGa_{1-x}As$ (x=0.04 to 0.30)	100 nm/step	Si-doped (1×10^{18} cm^{-3})	metamorphic buffer
$In_{0.02}Ga_{0.98}As$	100 nm		
GaAs	100 nm	Si-doped (1×10^{18} cm^{-3})	
n-GaAs substrate			

Figure 3.5-1 shows a (004) ω-2θ X-ray scan (at ω_{rel}=0) around the [110] direction for the structure in Table 3.5-1. The peaks of the last two metamorphic layers ($In_xGa_{1-x}As$, x = 0.28, 0.30) are a sign of the defect-free crystalline quality of these layers. The peak of the $In_{0.30}Ga_{0.70}As$ layer has slightly higher intensity than the peak of the $In_{0.28}Ga_{0.72}As$ layer, revealing a better quality of the layer. This was verified with X-TEM (Figure 3.5-2) in two diffraction conditions (the image taken at g = [002] shows the interfaces of the metamorphic layers and the

one taken at g = [220] shows the absence of the dislocations propagating though the final layers).

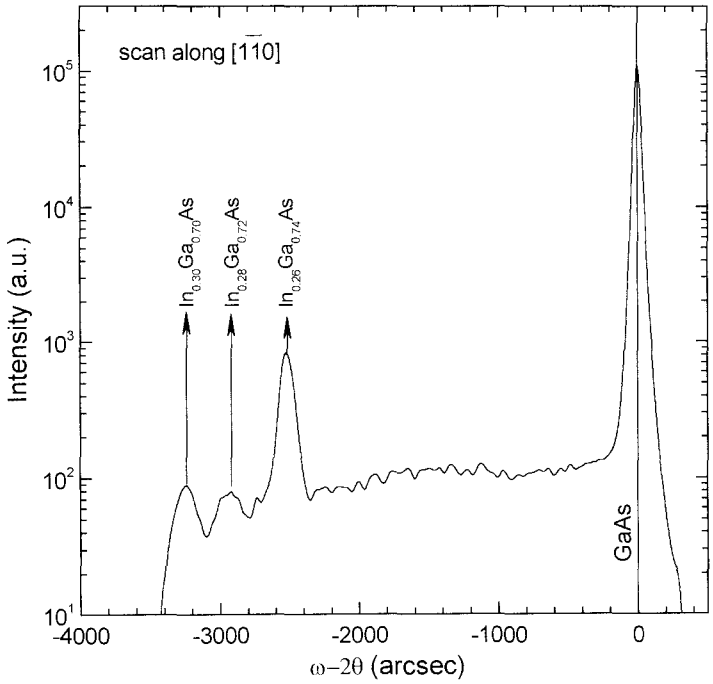

Figure 3.5-1: (004) ω-2θ X-ray scan (at ω_{rel}=0) around [110] direction for MSL in Table 3.5-1. The peaks of the last two metamorphic layers ($In_xGa_{1-x}As$, x = 0.28, 0.30) are a sign of the defect-free crystalline quality of these layers.

Figure 3.5-3 shows the space maps in two orthogonal <110> directions. The 2D contour plots (at the bottom of the Figure 3.5-3) in [110] and [1$\bar{1}$0] show an anisotropy in the symmetrical mosaic spread of the (004) planes in the two orthogonal directions. The mosaic spread of (004) planes are about ± 1.2° and ± 0.4° in [110] and [1$\bar{1}$0] directions, respectively. It is evident that as the growth of $In_xGa_{1-x}As$ metamorphic layers starts, the mosaicity of the planes commences and the symmetrical spreads around axes are anisotropic in two orthogonal directions.

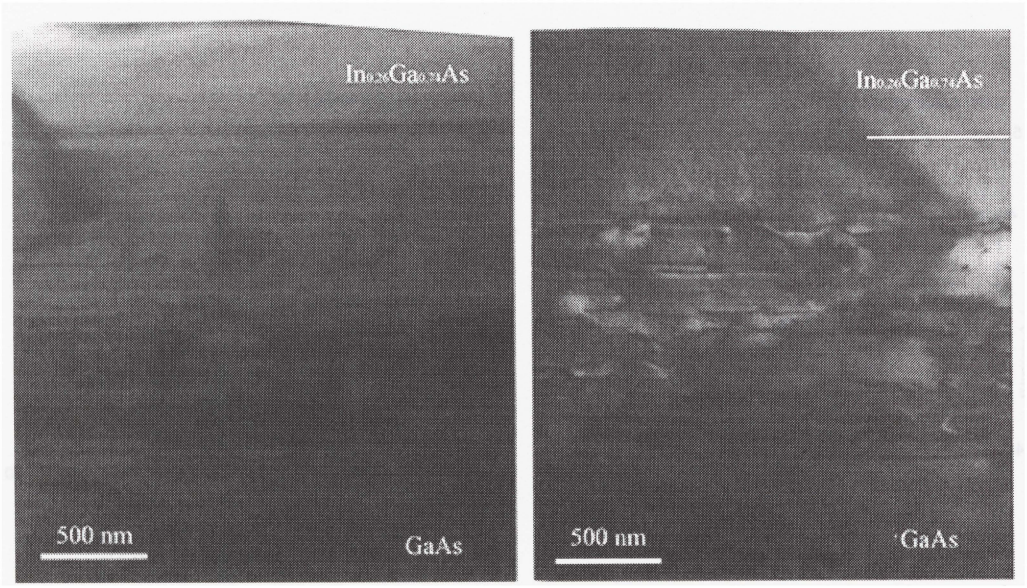

Figure 3.5-2: X-TEM micrographs of the structure showing the interfaces of the metamorphic layers (left: g = [002]) and the absence of the dislocations propagating through terminal layer (right: g = [220]).

The mosaicity increases in [110] direction as the growth advances, however, the mosaic spread is constant in $[1\bar{1}0]$ direction. This behaviour was also observed in other samples (not shown here). The ± 1.2° (2.4°) mosaic spread in [110] direction is in agreement with the result reported by Pidduck et al.[164] who reported through AFM studies that (001) GaAs grown by MBE under various conditions forms surface ridges preferentially along one <110> direction with slopes of ~ 2°. The anisotropy in the mosaic spread in two <110> directions suggests the same type of asymmetry due to the presence of kinks and multilevel-terrace growth front during the growth of $In_xGa_{1-x}As$ metamorphic buffer layers.[149]

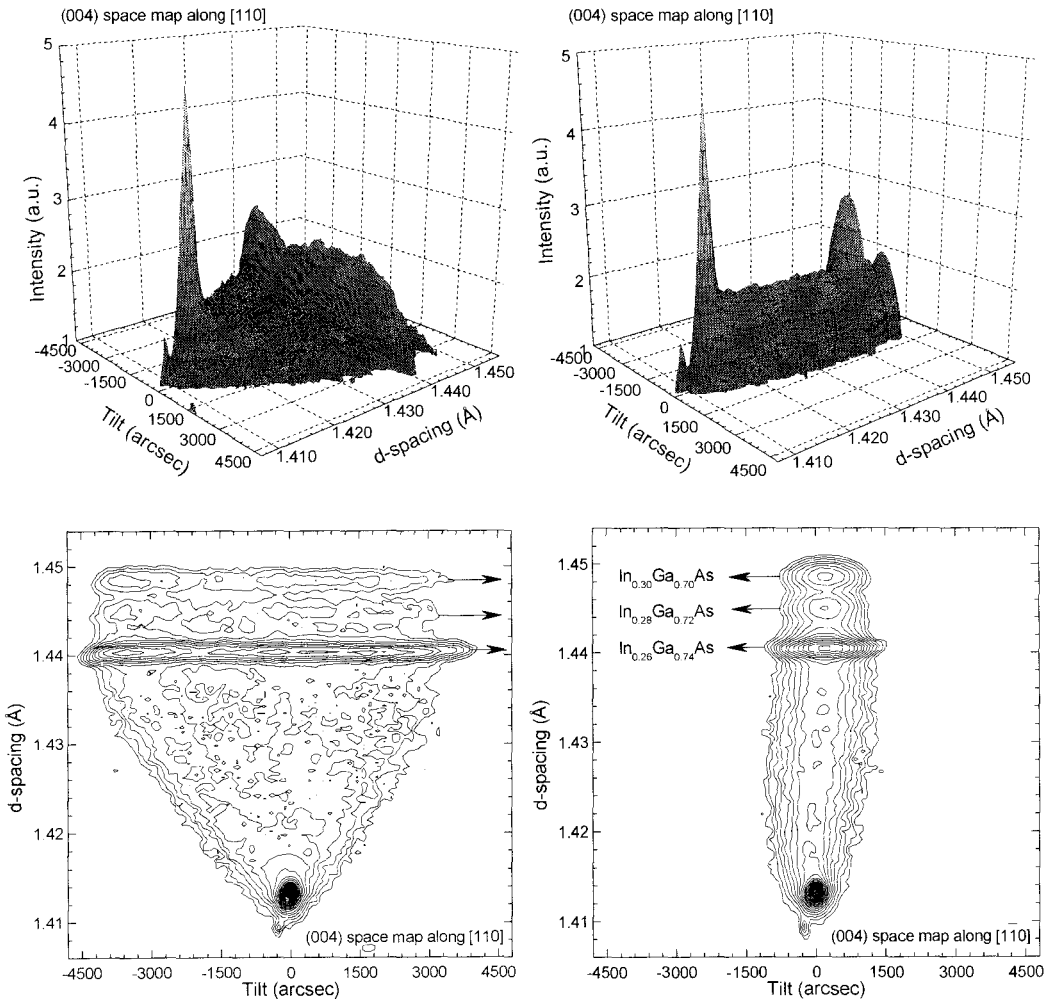

Figure 3.5-3: (004) d-space maps of $In_xGa_{1-x}As$ MSLs in [110] (left) and in [1$\bar{1}$0] (right) directions. Top graphs: 3D surface maps. Bottom graphs: 2D contour plots.

The 2D contour plots (bottom) in [110] and [1$\bar{1}$0] show an anisotropy in the symmetrical mosaic spread of the (004) planes in the two orthogonal directions. As the growth of $In_xGa_{1-x}As$ metamorphic layers starts, the mosaicity of the planes commences and the symmetrical spreads around axes is anisotropic in two orthogonal directions.

3.6. Discussion

The observation of relaxation in III-V heteroepitaxial layers shows that two waves of misfit dislocation introduction occur.[98, 154, 159, 165, 166, 167] The first wave occurs at the critical thickness h_c, when MDs are energetically favoured to be present at the interface. This initial set of dislocations arises from the substrate imperfections such as threading dislocations which intersect the surface of the substrate[166] or surface steps.[131] It has been shown that the first wave of dislocation introduction commences at about 3.5× greater than the theoretical critical thickness observed from anti-phase boundaries in ordered InGaP.[159] The second wave of dislocations occurs at a thickness considerably larger (10 – 12×) than h_c [159, 165] and results from dislocation multiplication.[167] Among several different dislocation multiplication mechanisms that have been proposed,[167, 168, 169] the Hagen–Strunk mechanism[168] is based on the interaction and cross slip of dislocations on {111} planes that are present at the same interface and multiplying perpendicular dislocation. The Hagen–Strunk mechanism is not a plausible mechanism at the early stages of relaxation in III-V material systems since these alloys have two waves of dislocations at early stages of growth. We propose the following possible process for the multiplication of the like-sign BV dislocations. The process starts with generation of α-dislocations at the $In_xGa_{1-x}As$ surface, preferentially at the step edges. The practical critical thickness should have been smaller in our samples since the underlying LT-InGaP was under compressive

strain (Figure 3.4.2-1 (a)). These dislocations will emit several β-dislocations according to plausible mechanisms described by Capano[169] at the early stages of the relaxation according to the following steps: pinning of the threading arm of α-dislocations; cross-slip of a part of the threading arm in the perpendicular slip plane; activation of a spiral source on the secondary slip plane; expansion of the dislocation until it reaches the interface; and continued glide around the pinning point after untangling the original dislocation. We speculate that the β-dislocation formation will proceed by formation of jogs due to injection of P interstitials according to the climb mechanism proposed by Petroff and Kimerling.[170] These jogs will act as an internal dislocation (internal dislocation refers to dislocations lying above but parallel to the interface) to multiply the α-dislocations based on the mechanism proposed by Beanland[167] according to the following steps: the threading arm of a 60° α-dislocation reacts with a perpendicular internal 60° β-dislocation (jog), this reaction forces a part of the threading arm to cross-slip; activation of a spiral source after a second cross slip; and emission of a bunch of dislocations parallel to the original incoming α-dislocation. Dislocation bunching or preferential grouping (presence of dislocations with identical BVs) has been reported in early stages of mismatched epitaxial growth.[159, 168, 171] With the exception of Spiecker et al.[159] who showed the bunching in cross sectional view, other authors based their conclusion on plan view images. The presence of the tilt around $[1\bar{1}0]$ in both specimens rules out the arguments of increased normalized

resolved shear stress on glide plane due to misorientation in accordance with the result of Fox and Jesser.[98] The accelerated tilt (Figure 3.4.2-1 (a)) in the sample with LT-InGaP might be a demonstration of overcoming of the system from high energy low-tilted to lower energy high-titled state according to Dodson et al.[146] It is not clear whether this might have been a result of multiplication or the nucleation of a new set dislocations.

3.7. Conclusion

Asymmetric tilt was found in an $In_{0.42}Ga_{0.58}As$ metamorphic pseudosubstrate grown on a singular GaAs substrate with an initial layer of a LT-InGaP followed with step-graded $In_xGa_{1-x}As$ ($x = 0.02$ to 0.42) metamorphic buffer layers. The epitaxial films were tilted around $[1\bar{1}0]$ and the tilt was correlated with the imbalance of the BV tilt component of the 60° α-dislocations. Climb and jog formation of β-dislocations in the presence of P-interstitials were considered as route for multiplication of the like-sign BV α-dislocations as a plausible mechanism. Anisotropic mosaic spread in [110] and $[1\bar{1}0]$ direction was also verified with X-ray reciprocal space maps. The anisotropy in the mosaic spread in two <110> directions correlates with a suggested type of asymmetry due to the presence of kinks and multilevel-terrace growth front during the growth of $In_xGa_{1-x}As$ metamorphic buffer layers. X-ray and ED along with least square criterion were employed to determine the lattice constant. The residual strain in the

terminating substrate layer suggests that there should be a compositional undershoot for devices thick enough that they might trigger dislocation nucleation. This was in accordance with the models by Tsao[146] and Tersoff[155] who show that the equilibrium dislocation density is less than that which would eliminate the entire coherency strain. These results show that an asymmetric tilt boundary can be induced in mismatched heterointerfaces grown on a singular substrate. This might offer another route to control the dislocation multiplication specifically in the application of relaxed heterostructures on Si substrates.

Chapter 4 Characterization of InAs Quantum Dots on $In_xGa_{1-x}As$ ($0.0 \leq x \leq 0.3$) Metamorphic Pseudosubstrates on (001) GaAs Wafers

4.1. Introduction

The physics of quantum dots (QDs) reveals many identical characteristics with the behaviour of naturally occurring quantum systems in atomic physics. Methods to controllably fabricate semiconductor QDs have been developed in order to exploit their properties of extremely small dimensions and low power dissipation. The tuneable and discrete energy levels typical of QDs mean that the choice of emitted wavelength can be tailored and the small volume permits operation at low power. The shape and size dependence of the quantum effect have been verified in semiconductors by a series of experiments with quantum wells, wires, and dots.[172, 173] In a QD, the kinetic energy for states localized in the dots is fully quantized and the sub-band for the states becomes a series of discrete states (Figure 1.2-1 (d)). A continuum of the states may exist at higher energies but these correspond to unconfined states with energies above the barrier material. The discrete energy states are favourable for optical devices; firstly, more transitions can contribute to recombination at the same energy leading to a low threshold current density in laser devices;[174] and secondly, the thermal spreading of the energy of the carriers vanishes and temperature dependence of the current density disappears.[32]

Three dimensional confinement has been demonstrated in colloidal InAs dots,[175, 176] by QDs made from QWs by exploiting etching techniques,[53] by local interdiffusion,[58] and by the strain field of the nano-stressors.[59] Aside from the above methods, coherently self-organized islands that develop during the growth of highly strained layers are of considerable interest due to their ease of formation and compatibility with the growth of device structures. Among the three known heteroepitaxial growth modes (namely FvdM,[66] VW,[67] and S-K[68] modes), the S-K mode is considered to be the underlying mechanism in the growth of strained semiconductors, e.g. Ge on Si (001),[60] In(Ga)As on GaAs (001).[63] Joyce et al.[177] have shown that the growth of InAs QDs on GaAs will deviate from S-K growth mode with increasing growth temperature from 350 to 500 °C with substantial mass transport occurring from both the wetting layer[63] and substrate.[177]

There is an ambiguity about the shape of these self-organized dots. AFM images (Figure 4.3.1-1) resolve the QDs as having dome shaped features, but they are faceted and the AFM images are the convolution of the sample structure and AFM tip. Costantini et al.[178] demonstrated (with *in situ* STM) the existence (and/or coexistence) of only two families of faceted, defect-free islands in InAs/GaAs(001) and Ge/Si(001) systems. Only two discrete, well defined families of islands developed in both systems; pyramids are islands bounded by one type of shallow facets and domes are larger islands bounded by steeper, multi-faceted surfaces. The capping process of overgrowing with the substrate material results in the extension of the shallow facets at the expense of the steeper ones which

reduces the island heights. Figure 4.1-1 shows the STM topographs and structural models of Ge QDs on Si(001) and InAs QDs on GaAs(001) before and after capping with substrate material.[178]

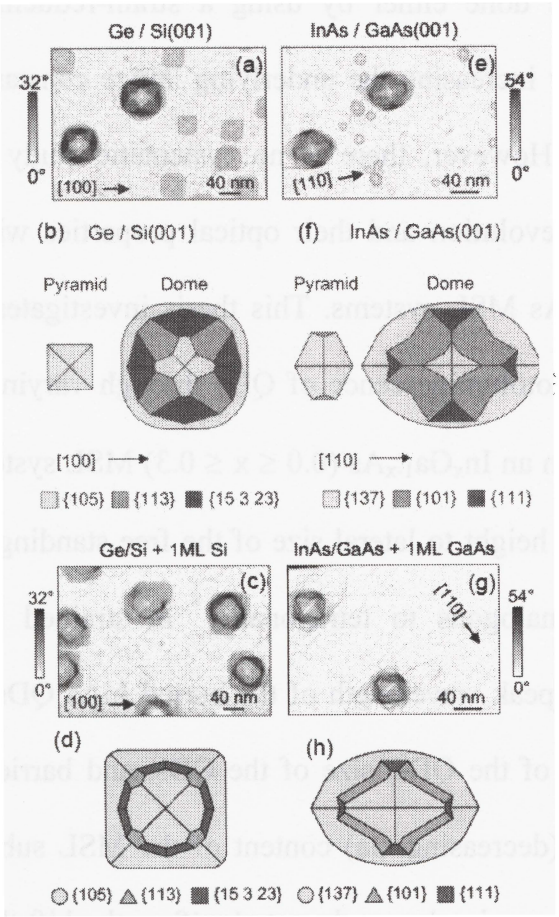

Figure 4.1-1: STM topograph of self-assembled pyramid and dome islands for: (a) 7.0 ML Ge on Si (001), (c) 1ML Si on Ge domes (e) 1.8 ML InAs on GaAs(001), and (g) 1 ML GaAs grown over InAs domes. Structural models of pyramid and dome shape islands for (b) Ge on Si (001), (d) Si overgrown on Ge domes, (f) InAs on GaAs (001), and (h) GaAs overgrown on InAs domes.[178]

In order to produce devices applicable to the telecommunication industry, temperature insensitive, long wavelength LDs (1.3 and 1.55 μm) are required. Several approaches, namely growth of InGaAs QDs on GaAs,[79, 85] strain-engineered InAs QDs on GaAs,[77, 83, 88] and using MSLs along with strain reducing

capping layers[84, 89] have been investigated. These approaches rely on the change in the band gap of QDs either by growing InGaAs QDs (which also changes the strain) on GaAs substrate or by tailoring the band gap of InAs QDs by varying the strain. This can be done either by using a strain-reducing capping layer or decreasing strain by increasing the underlying lattice constant via growing InAs QDs on an MSL. However, there is no systematic study on the relationship between InAs QD evolution and their optical properties with varying strain in InAs QDs/$In_xGa_{1-x}As$ MSL systems. This thesis investigates the changes in the morphology and photoluminescence of QDs through varying the strain in InAs QDs when grown on an $In_xGa_{1-x}As$ ($0.0 \leq x \leq 0.3$) MSL system. It will be shown that the ratio of the height to lateral size of the free standing dots increases with increasing strain analogous to tetragonality* in strained uniform films. The photoluminescence peak wavelength of the buried InAs QDs, which depends on strain, composition of the QDs, size of the QDs, and barrier material increases with increasing In (decreasing Ga) content of the MSL substrate. Also, thin (2 nm) strain-reducing capping layers do not *significantly* shift the PL peak. Through comparison of the experimental PL data with modelling studies, it was determined that Ga is incorporated in InAs QDs; and the Ga mole fraction in InAs QDs was estimated to linearly depend on the Ga mole fraction of the underlying $In_xGa_{1-x}As$ substrate. The findings, in agreement with the previous report of InAs QDs on GaAs,[177] show that the growth of InAs QDs on $In_xGa_{1-x}As$ MSLs occurs with

* The ratio of out-of-plane to in-plane lattice constant.

substantial mass transport from the substrate at high growth temperature (≅ 500 °C).

4.2. Structure of InAs QDs on $In_xGa_{1-x}As$ ($0.0 \leq x \leq 0.3$) MSLs

Figure 4.2-1 (top) shows a schematic of the layered structure grown to study InAs QDs on MSLs. The MSLs, terminating at the $In_{k2}Ga_{1-k2}As$ layer, were grown on a 2-inch diameter GaAs wafer according to growth details outlined in section 2.1.1. The wafers were cleaved into quarters and the lattice constants were calculated from X-ray diffraction data following the method outlined in section 2.3.2. Structures on top of MSLs ($In_{k2}Ga_{1-k2}As$ layer) were grown at 1 $\mu m \cdot hr^{-1}$ on a quarter of the pseudosubstrates. The QDs were grown at a growth rate of 0.1 ML/sec with an open-closed shutter sequence mode according to section 2.1.2. The buried QD layers in an $In_xGa_{1-x}As$ well were sandwiched between two $In_yGa_{1-y}P$ barrier layers, lattice matched to its underlying $In_xGa_{1-x}As$ layer, to confine carriers and enhance the PL emission. The structures were terminated with an InAs QD layer on the surface for AFM measurements. The samples were cooled under As_2 flux after the growth of the final QD terminating layer. Lateral size and height distributions were plotted according to section 2.5.1. The top layers above $In_yGa_{1-y}P$ were etched after AFM scans and prior to PL measurement according to section 2.6. Figure 4.2-1 (bottom) shows the schematic band diagram of the structures after etching the top $In_xGa_{1-x}As$ layer.

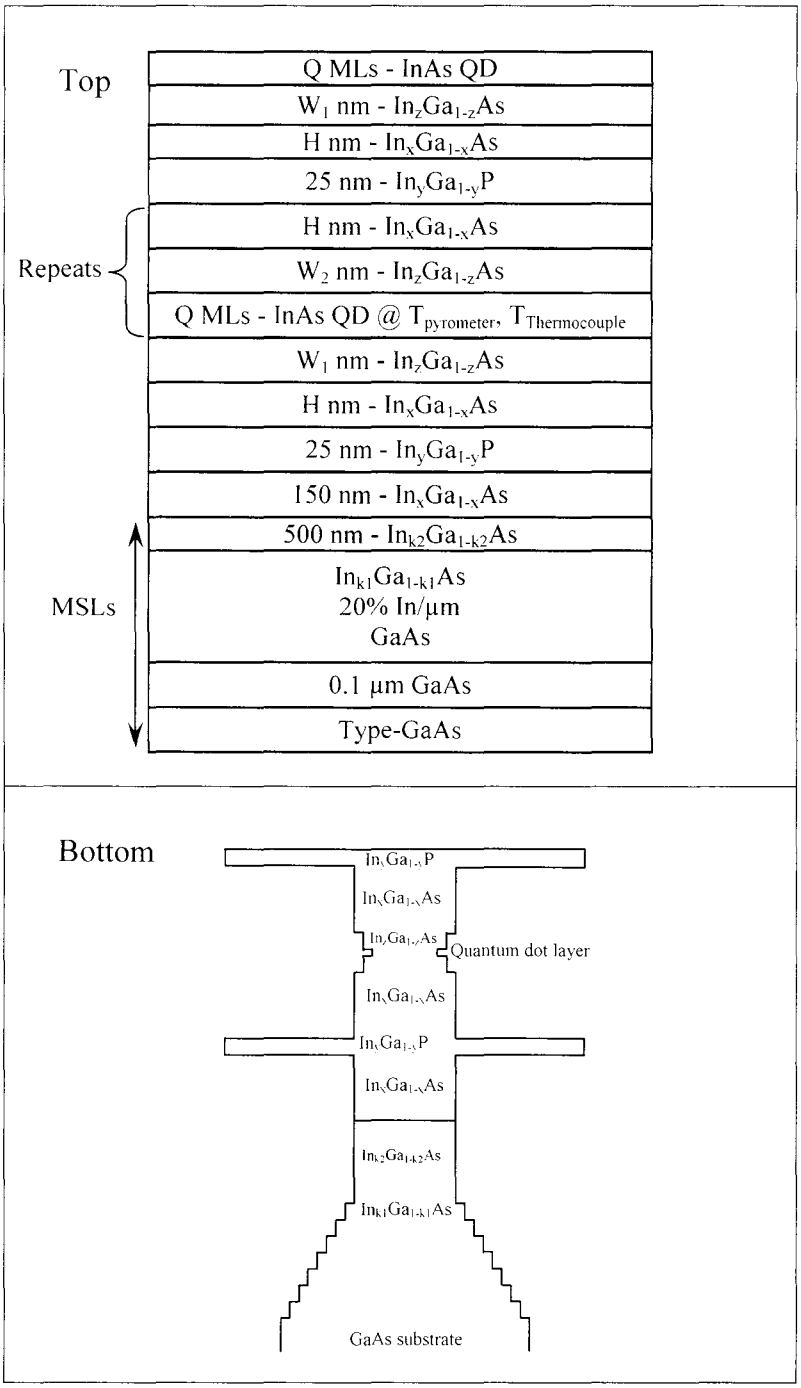

Figure 4.2-1: Top: Schematic structure of metamorphic pseudosubstrate and QD layers. Bottom: Schematic band energy diagram of samples after etching the top QD and $In_xGa_{1-x}As$ (and $In_zGa_{1-z}As$) layers.

The parameters of the structures shown in Figure 4.2-1 are tabulated in Table 4.2-1. Each structure will be referred to with its corresponding sample number. The *nominal* strains* are calculated based on the lateral lattice parameter of the underlying substrate, calculated from X-ray diffraction results (section 2.3.2), and the InAs lattice constant assuming no Ga and In inter-diffusion between the InAs QDs and their barrier materials. Both pyrometer and thermocouple temperatures are reported for reference. Figure 4.2-2 shows the <110> cross sectional TEM micrographs of structures in Table 4.2-1 verifying that the QDs are coherently formed on the substrate as no dislocations were visible on these micrographs.

Table 4.2-1: Tabulated parameters for the structures shown in Figure 4.2-1.

$T_{Thermocouple}$ (°C) (at the back side of the wafer)	424	409	422	423	423	405	406	413
$T_{pyrometer}$ (°C)	475	480	500	500	500	480	500	500
Repeats	0	0	0	0	0	1	0	0
W_2 (nm)	0.0	2.0	2.5	1.82	1.82	4.0	0.0	7.5
Q (MLs)	**2.2**	**2.2**	**2.6**	**2.2**	**2.6**	**3.0**	**3.0**	**3.0**
W_1 (nm)	0.0	0.0	0.0	0.0	0.0	4.0	0.0	7.5
z	0.00	0.40	0.40	0.42	0.42	0.35	0.00	0.40
H (nm)	150	150	150	150	150	40	150	150
x	**0.00**	**0.17**	**0.17**	**0.22**	**0.22**	**0.27**	**0.30**	**0.30**
k2	0.00	0.21	0.21	0.26	0.26	0.32	0.30	0.30
k1	0.00	0.22	0.22	0.30	0.30	0.32	0.30	0.30
Type	Semi-Insulating	n-type	n-type	n-type	n-type	n-type	n-type	n-type
Nominal strain* with respect to underlying substrate (%)	7.16	5.87	5.87	5.50	5.50	5.13	4.90	4.90
Growth No.	121	651	666	740	734	553	285	286
Sample No.	**1**	**2**	**3**	**4**	**5**	**6**	**7**	**8**

* The QDs are under compressive strain and the absolute values of strain are reported hereafter.

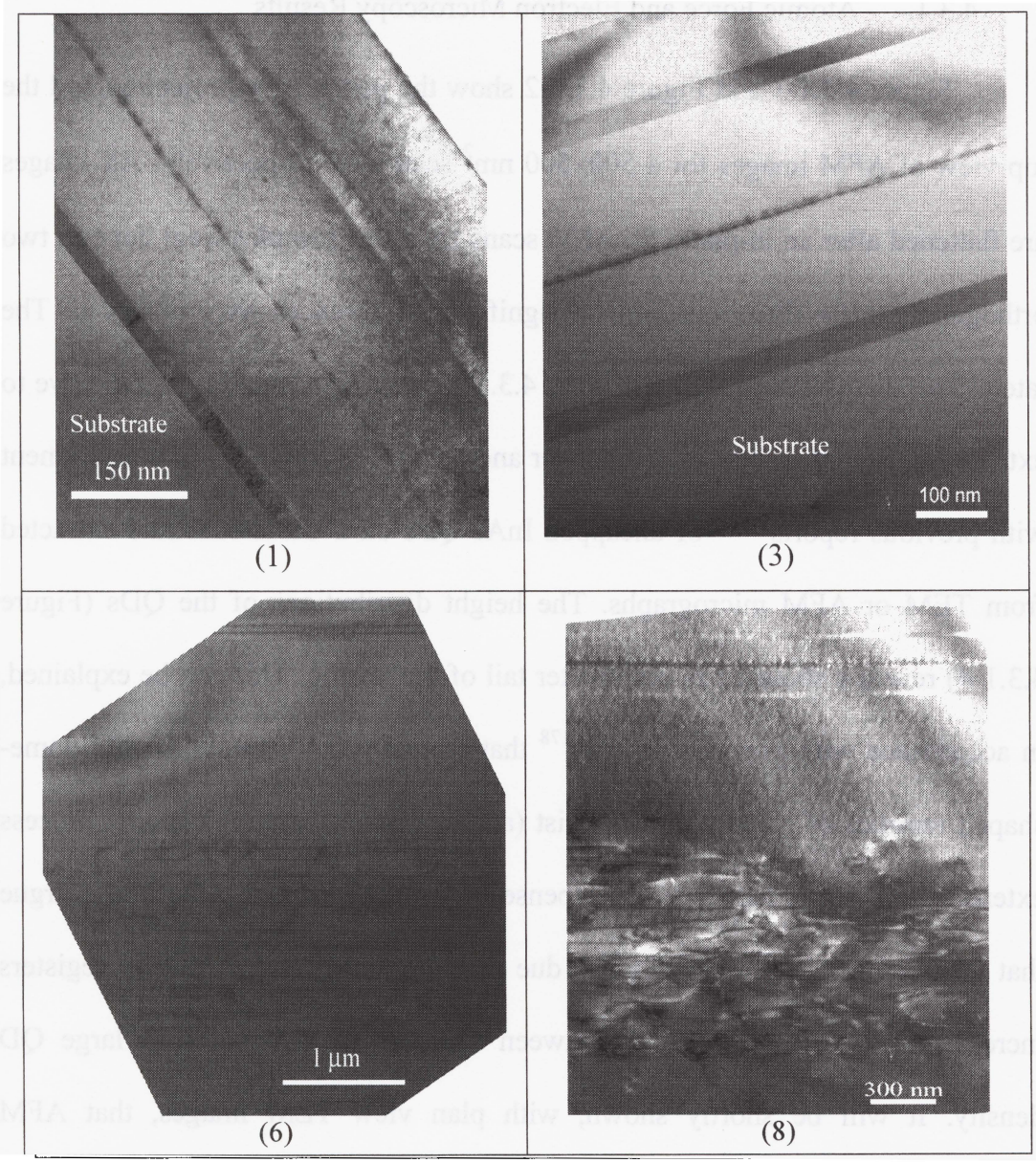

Figure 4.2-2: <110> cross sectional TEM images of InAs QD layers on $In_xGa_{1-x}As$ MSLs showing that the QDs are coherently formed on the substrate as no dislocations were visible with these imaging conditions. The numbers correspond to sample number in Table 4.2-1.

4.3. Size and Height Distribution of InAs QDs on MSLs

4.3.1. Atomic Force and Electron Microscopy Results

Figure 4.3.1-1 and Figure 4.3.1-2 show the perspective projection and the top view of AFM images for a 500×500 nm^2 scan area, respectively. All images are flattened after an in-plane fit. AFM scans for a few samples were done in two orthogonal <110> directions and no significant differences were observed. The lateral size distribution profiles (Figure 4.3.1-3) were fit with a Gaussian curve to extract the mean diameter. The diameter and height of sample # 1 is in agreement with previous reports[62, 63] of uncapped InAs QDs on a GaAs substrate extracted from TEM or AFM micrographs. The height distributions of the QDs (Figure 4.3.1-4) reveal a shoulder in the shorter tail of the profile. This can be explained, in accordance with previous reports,[178] that typically two pyramidal- and dome-shaped families of faceted islands exist (and/or coexist) and the capping process extends the shallow facets at the expense of the steeper ones. One might argue that the presence of the shoulder is due to the tip artifact; i.e. the tip registers increased heights in the spaces between the dots in samples with large QD density. It will be shortly shown, with plan view TEM images, that AFM measurements overestimate the lateral base dimension of the QDs (Figure 4.3.1-5 - sample # 6); and the QDs are not as close as they are revealed in AFM images. Moreover, the mean free distance between the bases of the dots based on plan

view TEM (Figure 4.3.1-5 – sample #6) is approximately 17 nm which is ~ 1.7× larger than the nominal size of the cantilever tip.

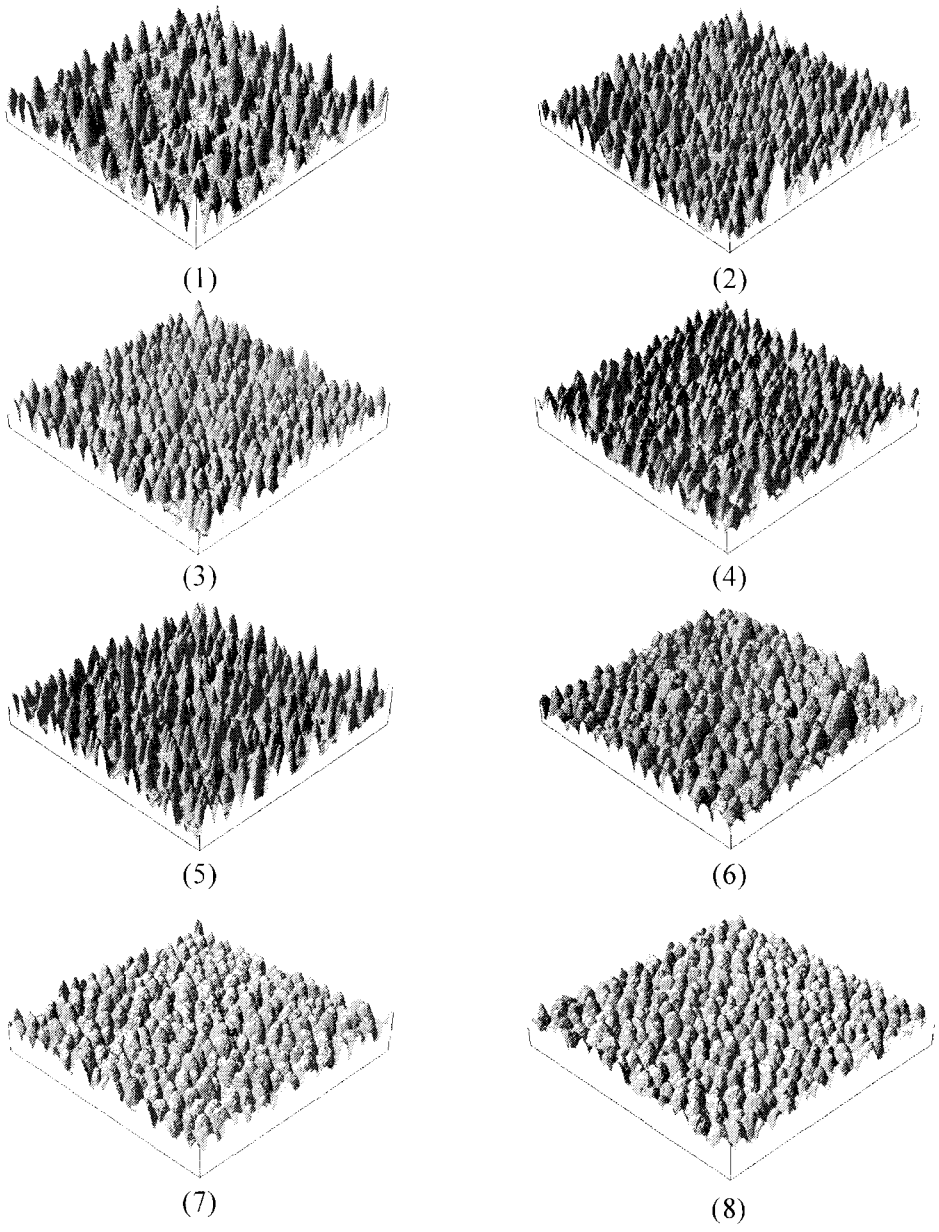

Figure 4.3.1-1: Perspective projection of AFM images (500×500 nm^2). All samples are flattened after and in-plane fit. The numbers under each graph correspond to the sample number in Table 4.2-1.

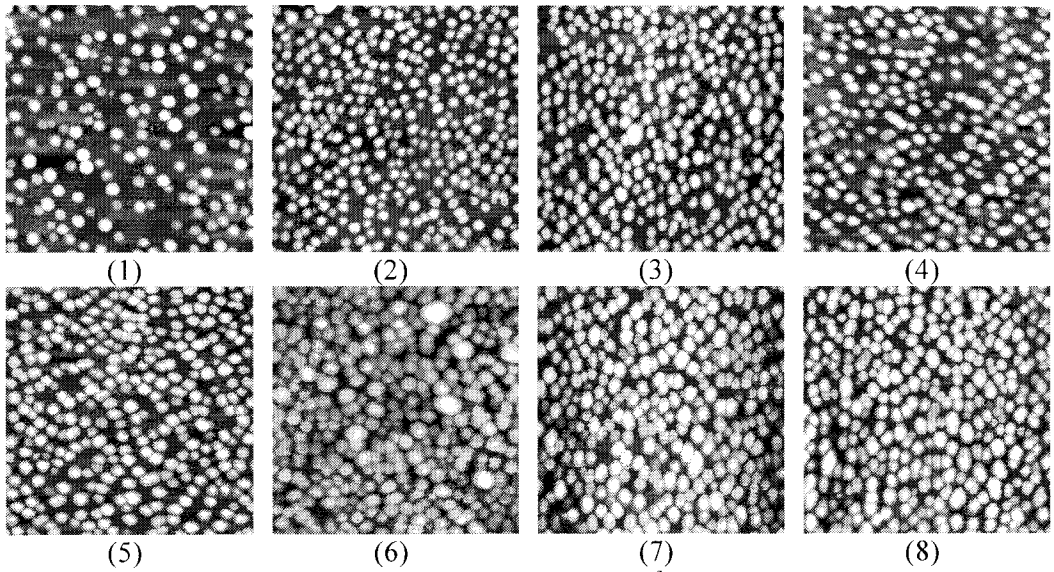

Figure 4.3.1-2: Top view of AFM images (500×500 nm^2) of sample # 1 through # 8 after in-plane fit and flattening. The numbers in each graph correspond to the sample number in Table 4.2-1.

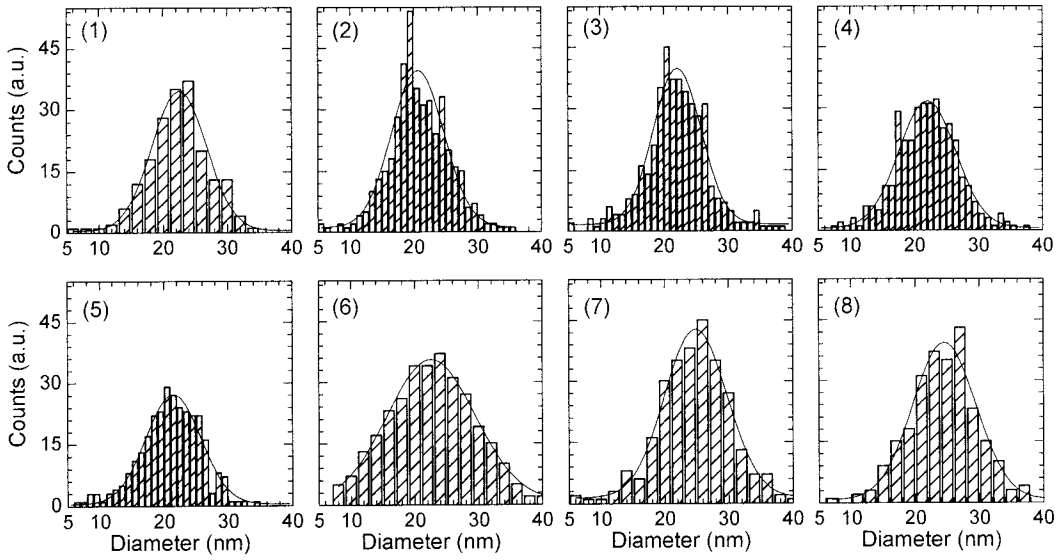

Figure 4.3.1-3: Lateral size distribution (and the Gaussian fits) of InAs QDs on different substrates. The data are superimposed from three separate scan areas on each sample. The numbers in each graph correspond to the sample number in Table 4.2-1.

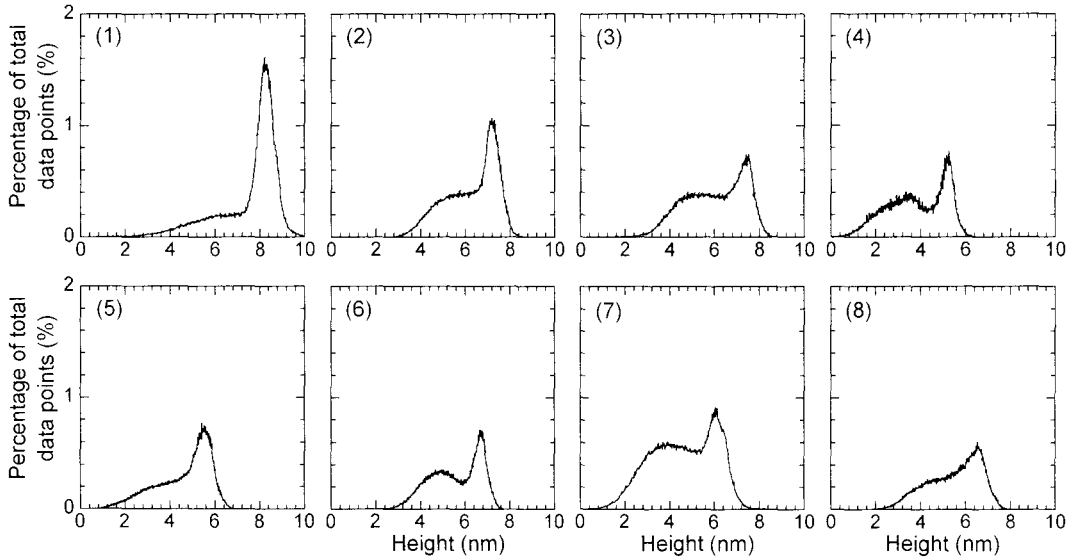

Figure 4.3.1-4: Height distribution of InAs QDs on different substrates. The height distributions of the QDs reveal second overlapping height distribution on the shorter tail of the profile. This is attributed to coexistence of two pyramidal and dome shaped families of faceted islands.[178] The numbers in each graph correspond to the sample number in Table 4.2-1.

To verify the range of lateral size and height distributions extracted from AFM measurements, high resolution cross sectional and plan view TEM images were obtained. These refer to buried QDs as opposed to surface quantum dots measured by the AFM. Figure 4.3.1-5 is the plan view TEM micrograph of surface InAs QDs on $In_{0.27}Ga_{0.73}As$ MSL (sample # 6) showing the facets of the QDs.[178] Figure 4.3.1-6 is the <110> on axis X-TEM of an InAs QD on a GaAs substrate. A comparison of the size-distribution profiles (Figure 4.3.1-3) extracted from AFM images reveals that the mean lateral base diameters of the QDs are approximately between 22 – 25 nm. In comparison, the lateral base dimension of InAs QDs on $In_{0.27}Ga_{0.73}As$ MSL (Figure 4.3.1-5 - sample # 6) based on plan view

TEM are estimated to be approximately between 16 – 19 nm. Thus, AFM measurements overestimate the lateral size of the QDs. Figure 4.3.1-6 also reveals that the lateral size and height of the buried QDs are approximately 17 nm and 7 nm, respectively. There are three issues to consider when interpreting TEM images of the QDs. First, there is no control on the sampling of the cross sectional QDs. In other words, one is not aware which part of the size distribution profile is being sampled. Second, there is an uncertainty about the location of the cross section through any single QD. If a semi spherical QD is sectioned more than half its diameter, the lateral size and height of the QD measured is less than its real value. Third, TEM images are formed by convolution of strain contrast with atomic number (Z) dependent contrast which results in overestimation of the dot dimensions.

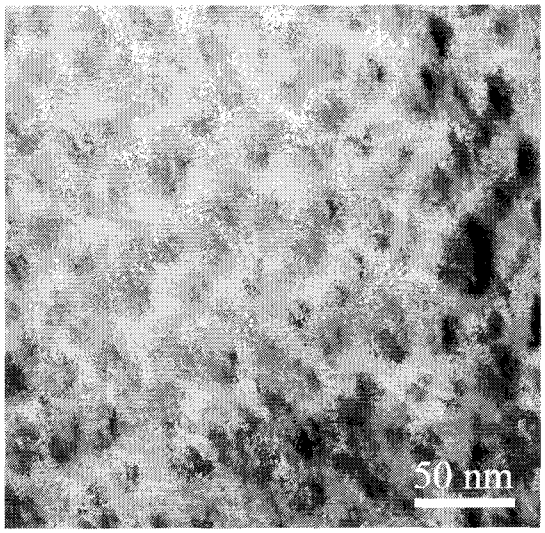

Figure 4.3.1-5: Plan view TEM micrograph of surface InAs QDs on $In_{0.27}Ga_{0.73}As$ MSL (sample # 6) showing the pyramid pattern of the QDs. The base diameters of the dots are approximately 16 - 19 nm.

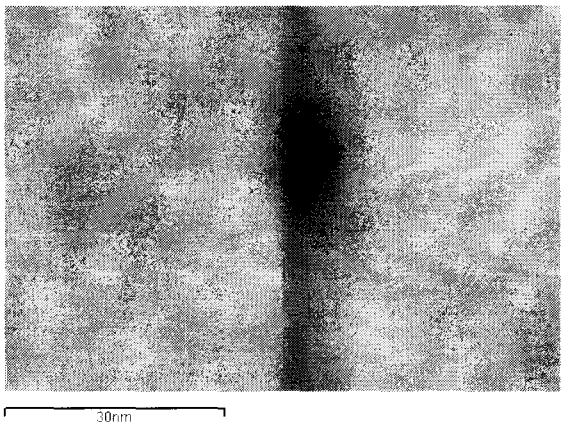

Figure 4.3.1-6: <110> XTEM micrograph of a buried InAs QD on GaAs substrate (sample #1). Approximate diameter and height are ~ 17.4 and ~ 7.1 nm, respectively. Note that TEM images are formed by convolution of strain contrast with atomic number (Z) dependent contrast which results in overestimation of the dot dimensions.

Leonard et al.[61] reported a Gaussian size-distribution of 27.8 ± 2.8 nm for a 4ML layer of $In_{0.5}Ga_{0.5}As$ QDs buried under GaAs on a GaAs substrate measured through two beam dynamical electron diffraction of plan view samples. It should be reiterated that though the absolute size of the QDs is overestimated in TEM[61, 179] or AFM measurements, the distribution itself will remain unaffected. Note that the comparison between XTEM and AFM results, in accordance with previous reports,[179] show that the buried QDs are smaller compared to the surface dots.

When the coherent islands form, the total energy of the system can be written as[65]

Equation 4.3.1-1 $$E = E_{\text{surf}} + E_{\text{edges}} + \Delta E_{\text{elastic}}$$

where E_{surf}, E_{edges}, and $\Delta E_{elastic}$ are the energy needed to create the surfaces (facets) of the islands, the energy to create island edges, and the change in energy due to elastic relaxation, respectively. The above energies are proportional to the island size (D) according to $E_{surf} \cong a(\varepsilon) \cdot D^2$, $E_{edges} \cong b(\varepsilon) \cdot D$, and $\Delta E_{elastic} \cong c(\varepsilon) \cdot D^3$. Note that the coefficients are functions of strain. If we consider a constant strain (e.g. InAs QDs on GaAs) there is a critical dimension (D_{crit}) where the increase in E_{surf} and E_{edges} due to the formation of dots are cancelled by the reduction of energy due to elastic relaxation of strain ($\Delta E_{elastic}$). The coherent islands with sizes larger than D_{crit} are energetically favoured and the belief is that, once formed, they undergo Ostwald ripening at the expense of annihilation of the islands with sizes smaller than D_{crit}. However, the ripening becomes energetically unfavourable at some stage during the growth due to the competition between dislocation introduction and elastic relaxation. Note that the growth of QDs deviates[177] from the S-K growth mode at higher growth temperatures (>400 °C) with substantial mass transport from both the WL[63] and substrate[177] to maximize the $\Delta E_{elastic}$.

Kobayashi et al.[180] have shown that the average lateral size and dispersion of uncapped InAs QDs on GaAs, measured through *in-situ* AFM measurements, initially increases with an increasing number of InAs MLs and then decreases and saturates. The InAs coverage in our samples was chosen so that the growth condition falls in the saturation regime. Kobayashi et al.[180] explained this

evolution through two possible mechanisms. First, the growth rate of an InAs QD slows down as its size increases due to accumulation of elastic energy. From a kinetic point of view, this can be considered as an increase in the energy barrier for atoms to incorporate into an existing island whether at its edges or from underlying wetting layer (WL) or substrate. Consequently, the smaller dots will grow faster or new islands will nucleate. A second possible mechanism is due to the presence of interacting island-induced strain fields in the substrate with increasing InAs deposition. There will be a driving force for migration of atoms toward smaller dots due to a downward tilt in surface potential toward smaller islands.

4.3.2. Evolution of Size and Height of Surface QDs with Varying Strain

Figure 4.3.2-1 (a), (b), and (c) show the diameter (d), height (h), ($\frac{h}{d}$), and density of the QDs versus nominal strain. The ratio of $\frac{h}{d}$ was calculated based on the mean diameter and height data. Sample # 8 was excluded from this graph because the QDs were grown on a strained $In_{0.4}Ga_{0.6}As$ layer instead of directly on the metamorphic layer. Note that the absolute lateral sizes of the QDs are overestimated in AFM measurements, therefore all diameters are expected to move to smaller values. Figure 4.3.2-1 (a) shows that as the strain increases the mean diameters *slowly* decrease from 25 ± 4.9 nm to 22 ± 4.9 nm. On the other

hand, the height of the QDs with the same InAs ML coverage increases with increasing strain (i.e. an increase in height from sample # 7 to # 6 (3.0 ML InAs) and from sample # 4 to # 2 to # 1 (2.2 ML InAs)). The decrease in height from sample # 6 to # 4 is due to the decrease in InAs coverage from 3.0 to 2.2 ML. Increasing the InAs ML coverage at a constant strain from 2.2 ML to 2.6 ML (i.e., sample #2 and 3, and sample #4 and 5) will increase the height of the QDs without a significant change in diameter. This is expected since the atoms are not constrained in the growth direction.

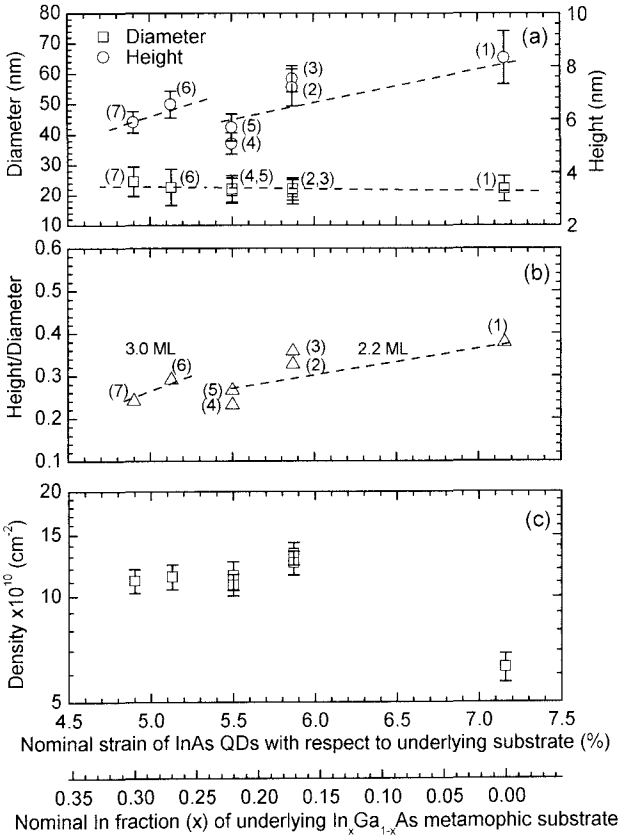

Figure 4.3.2-1: (a) Mean diameter (d) and height (h), (b) $(\frac{h}{d})$, and (c) density of QDs versus nominal strain. The error bars represent the standard deviation of the Gaussian distributions. The dashed lines are to guide the eyes.

The evolution of d and h versus strain indicates that the ratio $\frac{h}{d}$ of the QDs decreases with reducing strain (Figure 4.3.2-1 (b)). In other words, the QDs tend to evolve towards a uniform film morphology ($\frac{h}{d} = 0$) with deceasing strain as expected. The ratio of $\frac{h}{d}$ in a coherent island morphology is analogous to the tetragonaltiy ratio* in a uniform film morphology. The behaviour of the QDs with respect to strain is analogous to uniform films, i.e. increasing the strain increases the $\frac{h}{d}$ in coherent island morphology or tetragonality of the unit cell in uniform film morphology. The increase in the densities of the QDs with reducing strain is also attributed to the evolution of coherent islands toward uniform film morphology (i.e., coherent islands grown at smaller strains with respect to underlying substrate tend to have higher density with slightly larger lateral size and shorter height (Figure 4.3.2-1 (c)). Moreover, the increase in $\frac{h}{d}$ with increasing strain (at constant coverage) implies that the wetting layer should become thinner. Note that the change in elastic energy ($\Delta E_{\text{elastic}} \cong c(\varepsilon) \cdot D^3$) is a function of volume (Equation 4.3.1-1) and it is more favourable to release the elastic energy of the uniform film (WL) with increasing the size of the dots (specifically the height of the dots due to the freedom of the movement of atoms in the growth direction).

* The ratio of out-of-plane to in-plane lattice constant.

4.4. Energy-Dispersive X-ray Spectroscopy

Figure 4.4-1 (top) shows the location (grey line) for a <110> cross-sectional EDX line scan through a single InAs QD on a GaAs substrate (sample #1). Note that the InAs QD appears dome shaped, in contrast to pyramid shaped, and is distorted because the TEM image is a convolution of strain contrast with atomic number (Z) dependent contrast. Figure 4.4-1 (bottom) shows the compositional profiles (In, Ga, and As) obtained from this scan. The EDX profiles across InAs QD show an increase in In concentration as the electron beam crosses the WL and decreases as the beam moves toward the top of the QD. As the electron beam is scanned through the dot, the Ga atoms from the GaAs behind and in front of the InAs dots will be excited and emit X-rays, reducing the In/Ga ratio; this effect becomes more pronounced as the beam traverses towards the top of the dot. Figure 4.4-2 shows a line scan profile only through the WL in the region between the QDs. As the electron beam crosses the WL there is an increase in In and a decrease in Ga profile. Siverns et al.[179] showed that in the InAs QD/GaAs system, the WL and QDs alloy with the GaAs capping layer. Moreover, the alloying of the dots with the underlying substrate (GaAs) happens even before the capping process according to STM results.[181] Therefore, the interfaces between the dots and the substrate (GaAs in sample # 1) are not abrupt; this will put a constraint on the modeling of these systems since the confining potential will be varying gradually.

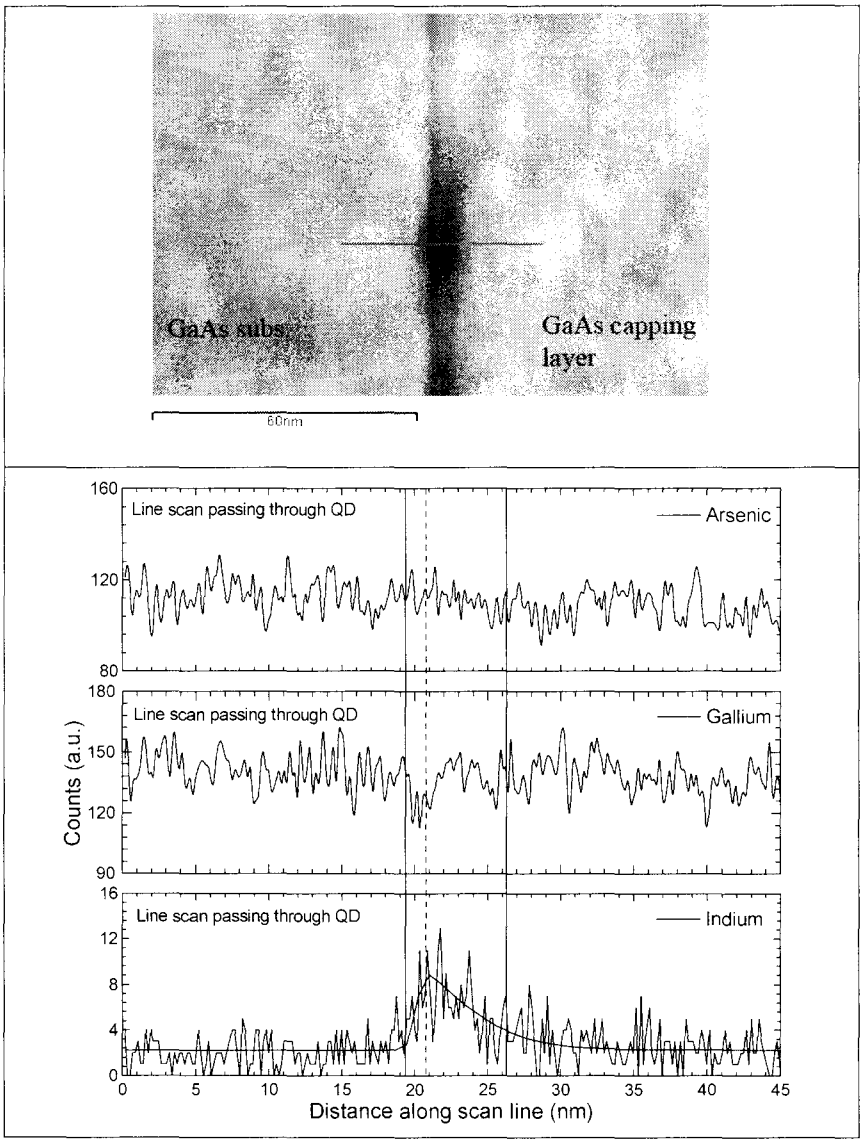

Figure 4.4-1: Top: <110> XTEM image of a single InAs QD on a GaAs substrate (sample # 1). The grey line depicts the EDX scan line. Note that the InAs QDs are dome (pyramid) shape. Bottom: EDX profiles across InAs QD showing the increase in In concentration in QD and its wetting layer. As the electron beam travels through QDs, In profile shows a peak of In. As the electron beam is scanned toward the top of the dot, more Ga atoms behind and in front of the InAs dots will be excited and emit X-rays. (The vertical dashed line is to guide the eye, showing the maximum and minimum in In and Ga profiles, respectively.)

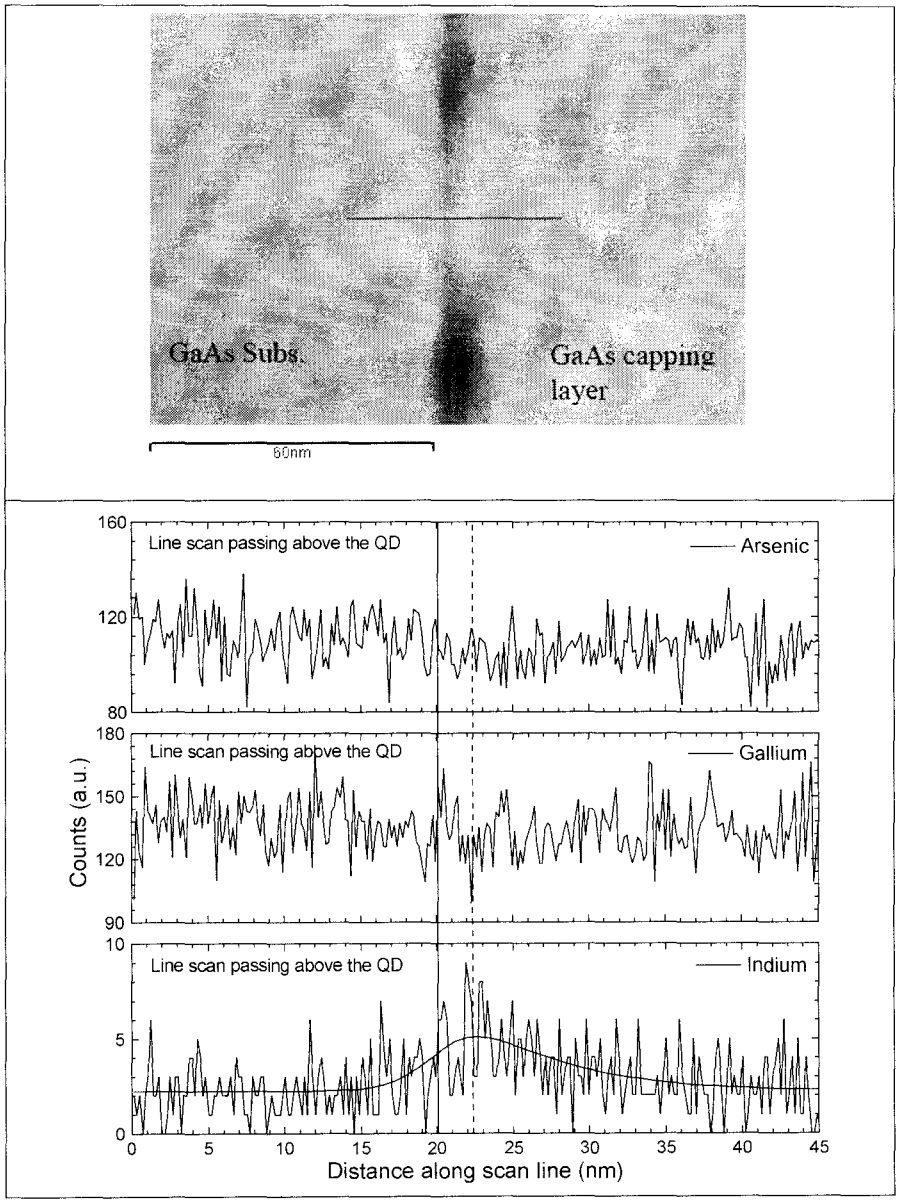

Figure 4.4-2: Top: <110> XTEM image of a single InAs QD on a GaAs substrate (sample #1). The grey line depicts the EDX scan line. Bottom: EDX profiles across InAs WL showing the increase in In concentration in WL. Note that the indium profile across the WL is broader compared to In profile for the line scan passing through the QD. (The vertical dashed line is for eye guiding purposes, showing the maximum and minimum in In and Ga profiles, respectively.)

4.5. Photoluminescence

Figure 4.5-1 shows the luminescence spectra of buried QDs of samples # 1 through # 8 measured at room temperature. They have been graphed in scale for comparison purposes. Except for samples # 1 and # 4, all samples show a weak radiative efficiency due to non-radiative recombination mechanisms present in the structures which are probably due to threading dislocations from underlying MSLs, although no dislocations were seen in the XTEM studies as shown in Figure 4.2-2.

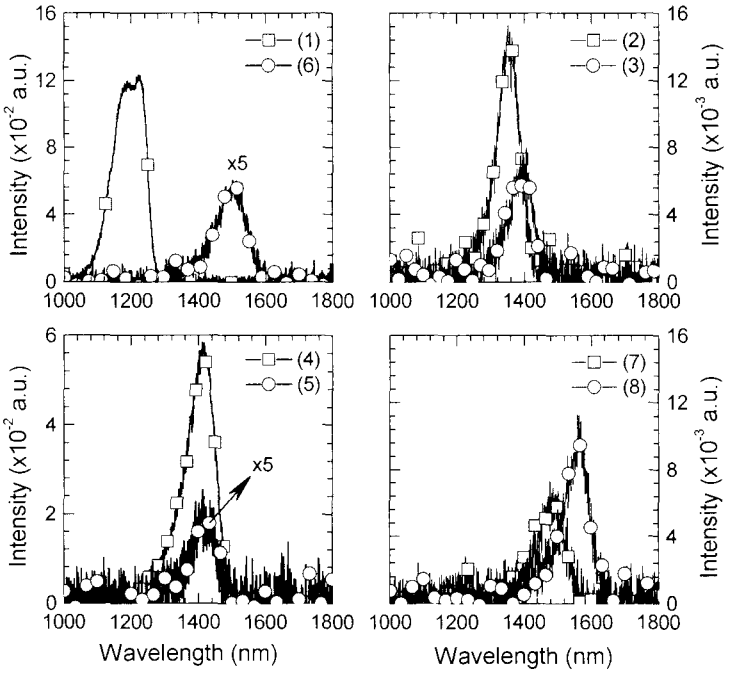

Figure 4.5-1: Photoluminescence spectra of the buried QD layers at room temperature. The numbers in each graph correspond to sample number in Table 4.2-1. (The profiles are continuous and only selected symbols are shown for identification purposes.)

The growth of the pseudosubstrate for sample # 4 was discussed in detail in section 3.5 and shows that it is possible to grow defect free pseudosubstrates

without employing the complicated defect reduction mechanism reported in Ref. [90]. The additional peak emerging at higher energy (shorter wavelength) for InAs QDs on GaAs (sample #1) is attributed to the energy difference between ground and excited states of InAs QDs on GaAs. Bogani et al.[182] reported, through time resolved PL measurements, that the energy difference of adjacent states of InAs QDs on GaAs (with same average diameter as our samples) is on the order of 40-50 meV which is in agreement with our results.

Figure 4.5-2 shows the peak PL wavelength, average height, and mean diameter versus nominal strain of InAs QDs with respect to the underlying substrate. The PL wavelength peak which is a function of the strain, the size of the QDs, the composition of the QDs, and barrier potentials increases with increasing In (decreasing Ga) content of the underlying MSL substrate. As the strain increases the mean diameter *slowly* decreases from 25 ± 4.9 nm to 22 ± 4.9 nm. The height of the QDs with the same InAs ML coverage increases with increasing strain (heights of the QDs increase from sample # 7 to # 6 (3.0 ML InAs) and from sample # 4 to # 2 to # 1 (2.2 ML InAs)). The decrease in height from sample # 6 to # 4 is due to the decrease in InAs coverage. Increasing the InAs ML coverage at a constant strain from 2.2 ML to 2.6 ML (i.e., sample # 2 and 3, and sample # 4 and 5) will slightly increase the height of the QDs without significant changes in diameters. Note that since the absolute sizes of the QDs are overestimated in AFM measurements, the diameter distribution line should really be at smaller values. Moreover, the buried QDs will be smaller based on EDX,

AFM and STM[178] results. Note that the QDs in sample # 8 which show a photoluminescence wavelength at ~ 1.55 μm are grown in an $In_{0.4}Ga_{0.6}As$ strained QW. The strained capping layer on the QDs (# 2 – 6) does not dramatically shift the emission wavelengths. As it will be shown shortly by modeling results, the strain with respect to underlying layer (whether through QD alloying or the change of the underlying lattice constant) makes a major contribution to change of the band gap of the QDs. It will be shown that the increase in the band gap due to alloying dominates the decrease in the band gap due to the reduction of compressive strain due to In/Ga exchange in QDs.

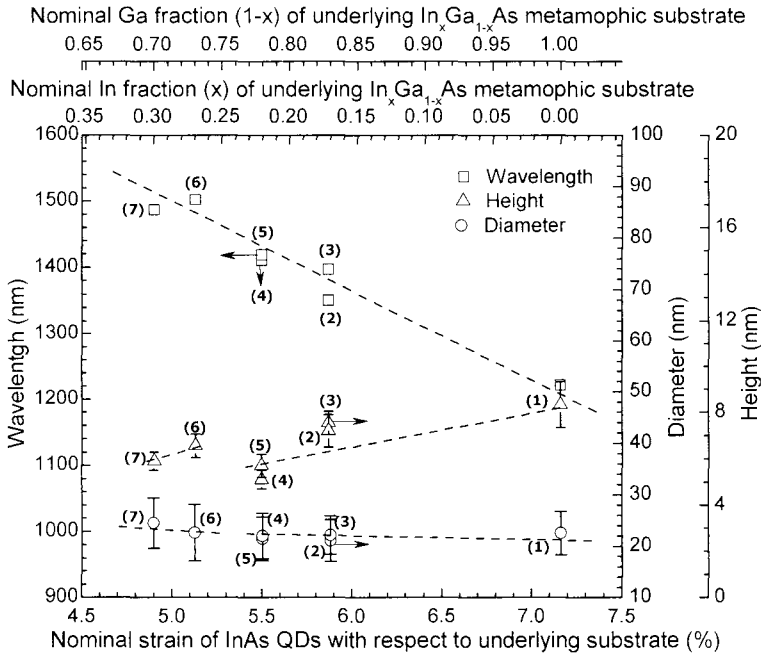

Figure 4.5-2: Wavelength, height and mean diameter vs. nominal strain ($|\varepsilon|$) of InAs QDs with respect to the underlying substrate. The height of the QDs with the same InAs ML coverage increases with increasing strain (i.e. an increase in height from sample # 7 to # 6 (3.0 ML InAs) and from sample # 4 to # 2 to # 1 (2.2 ML InAs)). Increasing the InAs ML coverage at a constant strain from 2.2 ML to 2.6 ML (i.e., sample #2 and 3, and sample #4 and 5) will slightly increase the height of the QDs without a significant change in diameter. (The error bars represent the standard deviation of the Gaussian distributions. The dashed lines are to guide the eyes.)

4.6. Modeling of the InAs QDs in $In_xGa_{1-x}As$ Quantum Well

QD systems in this work were modeled by Mohamed Naser and the results will be published in detail elsewhere. The theoretical model based on the Green's function technique was developed to calculate the density of states (DOS) of electrons and heavy holes in the conduction (CB) and valence bands (VB) of the QDs.[183, 184] A numerical technique based on finite differences was used to solve the governing kinetic equations of the Green's function. The ground state position for both electrons and holes was extracted based on the DOS. The number of states per unit energy inside a cylindrical volume enclosing a QD is obtained by integrating the localized DOS over the chosen volume.[183, 184] Both the discrete energy levels and the continuum part of the spectrum for the QD inside the cylinder were obtained. The effect of the strain was taken into consideration by calculating the change in the band gap of the InAs as a function of strain according to Ref. [38]. The CB and VB offsets between InAs QDs and $In_xGa_{1-x}As$ substrates are taken to be 60 and 40 % of their differences in the band gaps, respectively[185] and type I band offsets are assumed. As an approximate estimate, the diameters and heights of the buried QDs were extracted based on the linear fit to the experimental results of the samples # 1, 2, 4, 6, 7 (Figure 4.3.2-1 (a)). For simplification purposes, the WL thicknesses were considered constant (0.5 nm). The diameter and height of the cylinder enclosing one QD were chosen to be 40 nm and 30 nm, respectively.

Figure 4.6-1 shows the change in the band gap, CB, and VB offsets as a function of strain for InAs QDs grown on different $In_xGa_{1-x}As$ ($0.0 \leq x \leq 0.3$) MSLs. It is evident that increasing the strain increases the band gap of InAs, CB, and VB offsets. Increasing the band gap and the barrier potentials will make the separation between the ground states of electrons and holes larger and hence blue-shift the PL peak.

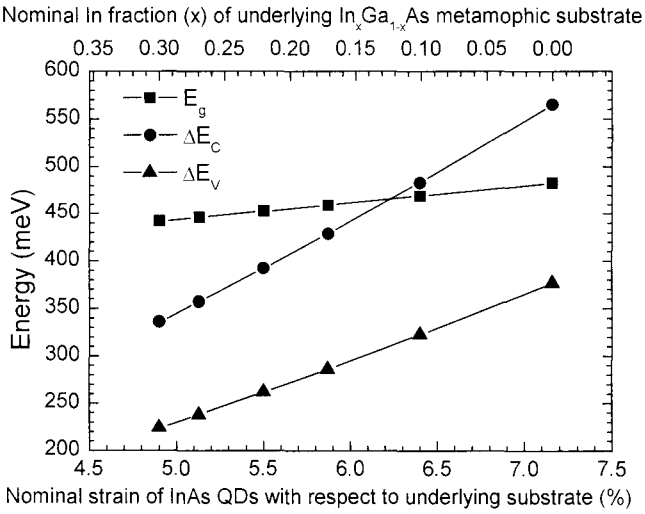

Figure 4.6-1: The change in InAs band gap, CB, and VB offsets versus nominal strain. (In mole fraction of the underlying MSL is provided for comparison purposes.)

Figure 4.6-2 depicts the PL peak wavelengths for the experimental and simulation results. The PL peak wavelengths of experimental results which are function of strain, size of the QD, composition of the QDs, and barrier potentials increases with increasing the In content of underlying MSL. Note that the difference between the ML coverage of the two sets of data (#1, 2, 3 and 6, 7) is ignored. The separation between the ground states of electrons and heavy holes based on simulation of InAs QDs on GaAs is 888 meV (1396 nm). For InAs

grown on an $In_{0.3}Ga_{0.7}As$ MSL, the calculated ground state energy levels of electrons and holes shift to lower energy levels compared to the CB and VB edges of the InAs QDs and no higher bound excited states exist. The shift of the ground states and the disappearance of the bound excited states are due to the smaller barrier potentials (i.e. the CB and VB offsets decrease). The energy transition between the ground states of electrons and holes based on the modelling of InAs QDs on $In_{0.3}Ga_{0.7}As$ corresponds to 778 meV (1592 nm).

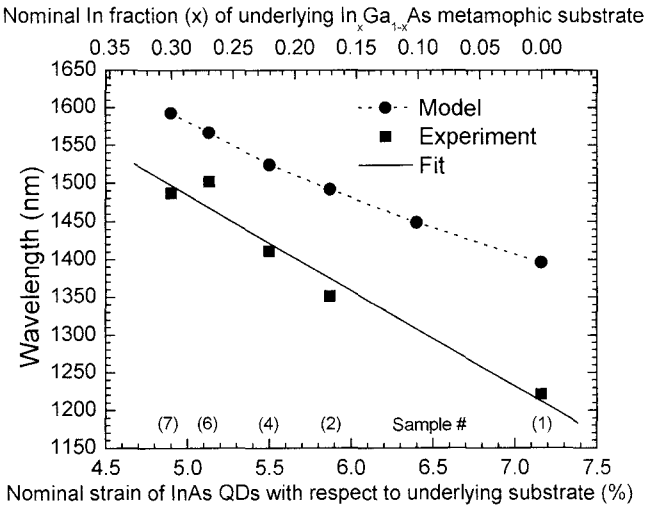

Figure 4.6-2: The calculated and the experimental PL peak wavelength versus nominal strain. (In mole fraction of underlying MSL is provided for comparison.)

There is a qualitative agreement between the model and the experimental results (i.e. the PL wavelength increases with increasing In mole fraction of the MSL in both sets of data). However, the model overestimates the experimental peak wavelengths. The overestimation can be attributed to Ga out-diffusion from underlying MSL during growth into the InAs QDs.[179] The amount of Ga diffusing into the InAs QDs will be expected to depend on the Ga mole fraction of the

underlying $In_xGa_{1-x}As$ substrate. Therefore, for a larger difference between the Ga fraction of the InAs QDs and $In_xGa_{1-x}As$ MSL, a larger amount of Ga inter-diffusion into the QDs is expected. Ga incorporation in the InAs QDs will modify the lattice constant, effective masses, band gap, and CB and VB offsets. The Ga incorporation increases the band gap, producing a blue-shift in the wavelength which is partially compensated for by a decrease in the strain. In order to fit the calculated wavelengths to those measured, the QDs were assumed to have an average composition of $In_qGa_{1-q}As$ where 1-q was assumed to linearly depend on the underlying Ga mole fraction (1-x) in the $In_xGa_{1-x}As$ MSL. Figure 4.6-3 shows a good agreement between the experimental and modelling PL for $In_qGa_{1-q}As$ QDs where $(1-q) = 0.33(1-x) - 0.13$.

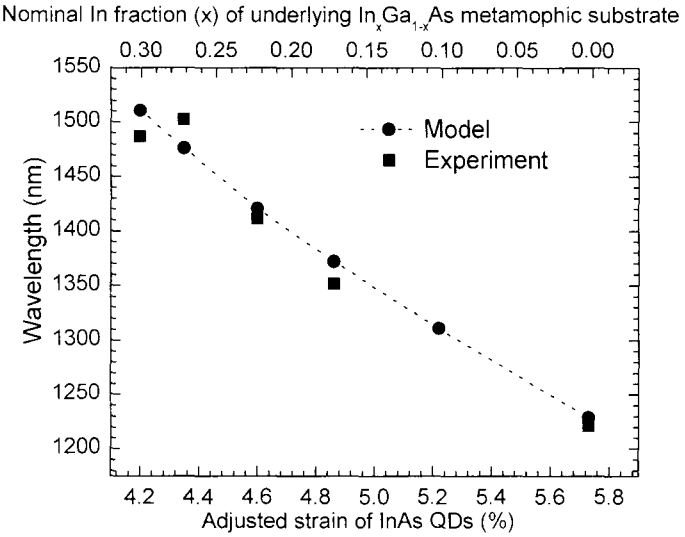

Figure 4.6-3: PL peak wavelength versus adjusted strain based the modelling of $In_qGa_{1-q}As$ QDs ($(1-q) = 0.33(1-x) - 0.13$) on $In_xGa_{1-x}As$ MSLs and experimental results.

Siverns et al.[179] also showed, through EDX measurement, that the QDs alloy with GaAs during the capping process and the Ga fraction (1-q) of the

$In_qGa_{1-q}As$ QD in InAs/GaAs system (where x = 0) is approximately 0.69. The discrepancy between their experimental measurements and the current modeling estimates of the composition of the QDs might be due to the overestimation of the size of the buried QDs based on surface QDs in this work, potential errors in their experimental EDX measurements, and their choice of the shape of the dots (i.e. semi-spherical compared to pyramids).

Figure 4.6-4 shows the strain of the InAs and the $In_qGa_{1-q}As$ QDs ($(1-q)=0.33(1-x)-0.13$) with respect to the In (x) (or Ga (1-x)) mole fraction of the underlying MSL. The strain decreases with increasing Ga incorporation (i.e. increase in 1-x) in the InAs QDs and this reduction is more pronounced at larger values of 1-x.

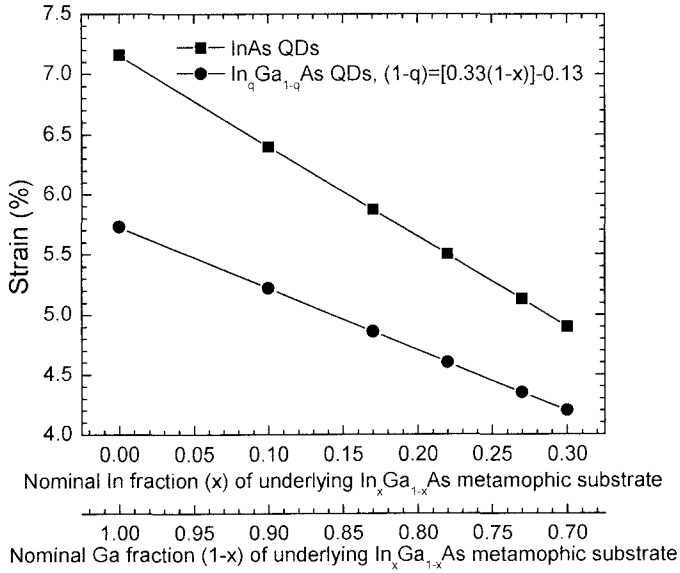

Figure 4.6-4: The strain of InAs and the $In_qGa_{1-q}As$ ($(1-q)=0.33(1-x)-0.13$) QDs versus In (x) (or Ga (1-x)) mole fraction of the underlying substrate. The strain decreases with increasing Ga incorporation (i.e. increase in 1-x) and the reduction is more pronounced at larger values (1-x).

The Ga incorporation into the QDs modifies the QD band gap and the corresponding CB and VB offsets and requires adjusting the strain with respect to the underlying MSL composition. These changes are shown in Figure 4.6-5. The band gap increases due to the incorporation of Ga and the CB and VB offsets decrease due to the reduction of the difference between the band gap of the QDs and the substrate.

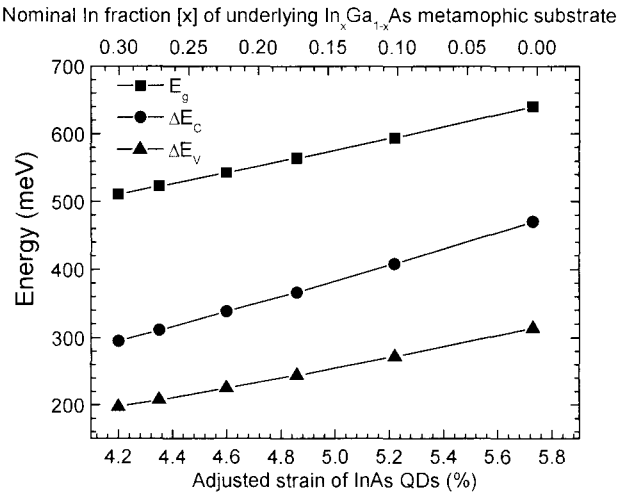

Figure 4.6-5: The bandgap, CB, and VB offsets of $In_qGa_{1-q}As$ QDs ($(1-q) = 0.33(1-x) - 0.13$, where x is the In mole fraction of underlying MSL) as a function of the adjusted strain. (Nominal In mole fraction of underlying MSL is provided for comparison.)

4.7. Discussion

Growth of thin (about a few monolayer[48, 60, 63]) highly strained semiconductor layers forms three dimensional faceted pyramid- or dome- shaped features[178] through the S-K growth mode.[68] The distribution of the QD diameters follows a Gaussian distribution and the height distributions of the free standing QDs reveal two overlapping height distributions which was attributed to the presence of two

families[178] of the QDs. Comparison of AFM measurements and plan view TEM images show that the AFM measurement overestimates the lateral size of the QDs. Moreover, the comparison between XTEM and AFM results, in agreement with previous reports,[179] show that the buried QDs are smaller compared to the free standing dots.

The morphology of the QDs on different MSLs show that, with decreasing the strain (at constant deposited coverage), the height (h) of the QDs decreases and the lateral diameter (d) increases slowly (Figure 4.3.2-1 (a)). This indicates that the ratio ($\frac{h}{d}$) of the QDs decreases with decreasing strain. The morphology of the coherent islands tend to move toward a uniform film morphology ($\frac{h}{d} = 0$) with decreasing strain as expected. The ratio of $\frac{h}{d}$ in coherent island morphology is analogous to the strain dependant tetragonality in uniform film morphology. Moreover, with increasing strain (at constant coverage), the increase in $\frac{h}{d}$ implies that the WL should become thinner. The change in elastic energy is a function of volume (Equation 4.3.1-1) and it is more favourable to release the elastic energy of the uniform film (WL) with increasing the size of the dots ($\Delta E_{\text{elastic}} \cong c(\varepsilon) \cdot D^3$).

The PL peak wavelength of the buried InAs QDs, which depends on strain, size and composition (through intermixing between the QDs and adjacent layers) of the QDs, and barrier potentials, increases with increasing the In content of the underlying MSLs. The PL peak wavelength calculated based on the

theoretical model qualitatively agrees with the experimental results. Increasing the strain increases the band gap of InAs, CB, and VB offsets; and therefore they will make the separation between the ground states of electrons and holes larger and hence blue-shift the PL peak wavelength. The amount of In/Ga intermixing in InAs QDs was modeled to linearly depend on the In (or Ga) mole fraction of the underlying $In_xGa_{1-x}As$ substrate (i.e. the larger the difference between the Ga fraction of the InAs QDs and $In_xGa_{1-x}As$ MSL, the larger the Ga incorporation into the QDs will be). The In/Ga intermixing can be viewed as a reduction of the difference of elastic energy between QDs and its surrounding matrix. Ga incorporation into InAs QDs increases the band gap and modifies CB, and VB offsets. The strain between In(Ga)As QD and underlying layer decreases with increasing Ga incorporation; and the reduction in strain decreases the contribution of strain in changing the band gap. On the other hand, the CB and VB offsets will decrease as Ga intermixes with InAs QDs; the band gap of the QDs increases relative to the surrounding barriers. The increase in the band gap blue-shifts the PL transition, while the decrease in the band offsets red-shifts them. However, the increase in the band gap is larger than the reduction of ground states due to the smaller potential barriers. The In/Ga intermixing of InAs QDs with the surrounding matrix ($In_xGa_{1-x}As$) is in agreement with previous reports.[177, 181]

4.8. Conclusion

This chapter reports on the evolution of InAs QDs with varying strain by changing the underlying pseudosubstrate ($In_xGa_{1-x}As$, $0 \leq x \leq 0.30$) lattice constant. The morphology of the QDs on different MSLs shows that with decreasing strain (at constant deposited coverage) the height (h) of the QDs decreases and diameter (d) slowly increases (Figure 4.5-2), analogous to the strain dependant tetragonality in uniform film morphology.

It was shown that it is possible to grow QDs on defect free pseudosubstrates (sample # 4) without employing the complicated defect reduction mechanism reported in Ref. [90]. The main contributing factors that result in the change in the peak PL wavelength are the change in the band gap of InAs due to strain, change in the confining potential due to the change of barriers, change in size of the QDs, and In/Ga intermixing in the QDs. The photoluminescence peak wavelength of the buried InAs QDs increases with increasing In (decreasing Ga) mole fraction of the underlying MSL; and thin strain-reducing capping layers do not significantly shift the PL. The amount of Ga included in InAs QDs was theoretically shown to linearly depend on the Ga mole fraction of the underlying $In_xGa_{1-x}As$ substrate (i.e. the larger the difference between the In fraction of the InAs QDs and $In_xGa_{1-x}As$ MSL, the larger the Ga incorporation into the QDs will be). These results confirm that the growth of InAs QDs tend to evolve toward a layer by layer growth mode with decreasing strain and the growth of In(Ga)As QDs on $In_xGa_{1-x}As$ involves intermixing from both wetting layer and substrate.

Chapter 5 Conclusion

$In_xGa_{1-x}As$ ($0.00 \leq x \leq 0.42$) MSLs were grown as a means to fabricate pseudosubstrates with larger lateral lattice constant than that of GaAs. The RSM contour plots of MSLs showed symmetrical mosaicity about the <110> axes but the spread was different in the two orthogonal [110] and [$1\bar{1}0$] directions. The anisotropy in the symmetrical mosaic spread in two <110> directions suggests the same type of asymmetry due to the presence of kinks and multilevel-terrace growth front during the growth of $In_xGa_{1-x}As$ metamorphic buffer layers.[149] It was shown that X-ray and electron diffraction along with the least square criterion can be employed to determine the lattice constant of the pseudosubstrate layer. The residual strain in terminating substrate layer suggests that there should be a compositional undershoot for devices thick enough that might trigger dislocation nucleation. A defect free pseudosubstrate was grown with employing a compositional undershoot in the terminating layer without using the complicated defect reduction mechanism as reported in Ref. [90].

Asymmetric tilt was found in an $In_{0.42}Ga_{0.58}As$ metamorphic pseudosubstrate grown on a (001) singular GaAs substrate with an initial layer of a LT-InGaP followed with step-graded $In_xGa_{1-x}As$ (x = 0.02 to 0.42) metamorphic buffer layers. The epitaxial films were tilted around [$1\bar{1}0$] and the tilt was correlated with the imbalance of the tilt component of BV of the 60° α-dislocations. Climb and jog formation of β-dislocations in the presence of P-

interstitials were considered as a plausible mechanism for multiplication of the like-sign BV α-dislocations. These results show that an asymmetric tilt boundary can be induced in mismatched heterointerfaces grown on a singular substrate. These finding might offer another route to control the dislocation multiplication specifically in the application of relaxed heterostructures on Si substrates.

The evolution of InAs QDs and their emission wavelength with varying strain on $In_xGa_{1-x}As$ ($0.0 \leq x \leq 0.3$) MSLs on GaAs substrates was studied. The results show that the ratio of the height (h) over lateral diameter (d) of the QDs decreases with decreasing strain. This is analogous to strained, coherent, uniform films where the tetragonality of the uniform film decreases with decreasing strain. The photoluminescence peak wavelength of the buried InAs QDs increases with increasing In (decreasing Ga) mole fraction of the underlying MSL. Also, thin strain-reducing capping layers do not significantly shift the PL peak. Decreasing the strain of the InAs QDs with respect to MSLs by increasing the In mole fraction of the underlying MSL reduces the barrier potentials and decreases the band gap of the QDs due to the reduction in strain, hence, reduces the separation between the ground states of electrons and holes, and red-shifts the PL peak. The change in size and the In/Ga intermixing with increasing In mole fraction of MSL also modifies the change in the PL peak. The amount of Ga diffusing into the InAs QDs is expected to depend on the difference between the Ga mole fraction of the InAs QDs and $In_xGa_{1-x}As$ MSL. Based on the theoretical modelling, the

dependence of Ga mole fraction in $In_qGa_{1-q}As$ QDs on Ga mole fraction of the underlying $In_xGa_{1-x}As$ MSL was estimated to increase linearly according to $(1-q) = 0.33(1-x) - 0.13$. These findings, in agreement with previous reports of InAs QDs on GaAs,[177, 181] show that the growth of InAs QDs on $In_xGa_{1-x}As$ MSLs occur with substantial mass transport from the substrate.

5.1. Future Research

Available theories of dislocation multiplication mechanisms are based on perfect dislocation interactions. However, the slip of the dislocations on (111) planes in zinc blend structures occurs via partial dislocations. There is growing need for understanding the underlying principles of dislocation multiplication based on partial dislocation interactions. The reciprocal space maps in this work are measured in two dimensional reciprocal spaces in two orthogonal directions; however, a three dimensional reciprocal space map (four dimensional graph) is needed for a comprehensive understanding of the mosaicity of the pseudosubstrate layer.

The lateral size distribution of QD ensembles was based on AFM measurement of the free standing islands. However, the dots evolve during the capping process. The lateral size distribution of capped QDs (with a few MLs of substrate material) should be verified with plan view TEM imaging.

Increasing the relative strain of the coherent islands with respect to underlying substrate implies that the wetting layer (WL) thickness decreases. The

change in the WL thickness with changing strain should be verified with high resolution EDX. The linear dependence of Ga mole fraction of $In_qGa_{1-q}As$ QDs on Ga mole fraction of the underlying $In_xGa_{1-x}As$ MSL was estimated based on modeling results which requires verification through EDX experimental studies. Temperature insensitive lasers emitting at ~ 1.55 μm with QD active region should be fabricated on metamorphic pseudosubstrates. Broadband QD optical sources might be achievable by stacking different $In_qGa_{1-q}As$ QD layers in the active region of the device.

Appendix A

Table A-1: Physical constants and useful physical quantities and conversions.

Physical constant	Symbol	Numerical values
Speed of light in vacuum	c	2.9979×10^{8} m/s
Bohr radius	$a_0 = \frac{4\pi\varepsilon_0\hbar^2}{e^2 m_0}$	0.529177 Å
Elementary charge	e	1.6022×10^{-19} C
Acceleration on earth at sea level due to gravity	g	9.8067 m/s^2
Gravitational constant	G	6.6730×10^{-11} m^3/kg s^2
Permittivity in free space	ε_0	8.8542×10^{-12} F/m
Permeability in free space	μ_0	$4\pi \times 10^{-7}$ H/m
Free electron mass	m_0 or m_e	9.1094×10^{-31} kg
Planck constant	h	6.6261×10^{-34} Js (4.1356×10^{-15} eVs)
Reduced Planck constant	$\hbar = \frac{h}{2\pi}$	1.05459×10^{-34} Js (6.5822×10^{-16} eVs)
Boltzmann constant	k_B	1.3807×10^{-23} J/K (8.6176×10^{-5} eV/K)
Avogadro number	N_{Avo}	6.0221×1023 mol^{-1}
Ideal gas constant	$R=kN_{Avo}$	8.3145 J K^{-1} mo^{-1}
Useful physical quantities		
Photon energy	$\hbar\omega = h\frac{c}{\lambda}$	$\frac{1.2398}{\lambda}$ eV, where λ is in μm
Energy unit	1 eV	1.60219×10^{-19} J
Angstrom unit	1 Å	10^{-10} m = 10^{-8} cm = 10^{-4} μm
Thermal energy at 300 K	k_BT	25.83 meV
Thermal energy at 293.15 K	k_BT	25.25 meV

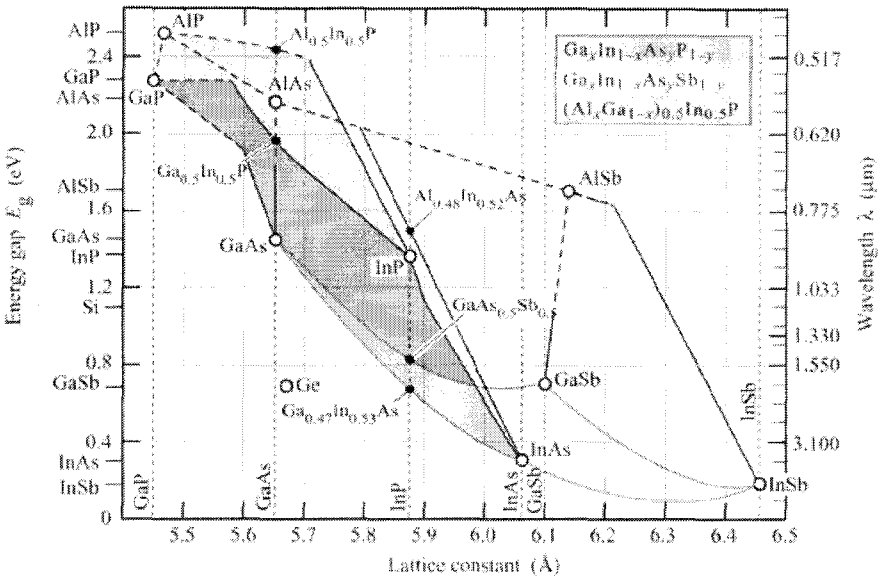

Figure A-1: Lattice Constant versus band gap at room temperature for III-V binary and ternary compounds.[186]

Table A-2: Electronic and Band Structure Parameters of a Few Binary Compounds.[187, 38]

Parameters	GaAs	GaP	InAs	InP
Lattice constant (Å)	5.65359	5.4506	6.0583	5.8687
Band gap (eV)				
0 K	1.51914	2.895 (Dir.) 2.350 (Ind.)	0.4180 (4.2 K)	1.4236 (1.6K)
300 K	1.424(1)	2.78 (Dir.) 2.272 (Ind.)	0.354(3) (295 K)	1.344
Deformation Potentials				
a_c (eV)	-7.17	-7.14	-5.08	-5.04
a_v (eV)	1.16	1.70	1.00	1.27
$a=a_c-a_v$ (eV)	-8.33	-8.83	-6.08	-6.31
b (eV)	-1.7	-1.8	-1.8	-1.7
d (eV)	-4.55	-4.5	-3.6	-5.6
C_{11} (10^{11} dyne/cm^2)	11.9	14.05	8.329	10.11
C_{12} (10^{11} dyne/cm^2)	5.38	6.203	4.526	5.61
C_{44} (10^{11} dyne/cm^2)	5.95	7.033	3.959	4.56
Effective masses				
m_e^*/m_0	0.067	0.25	0.023	0.077
m_{hh}^*/m_0	0.50	0.67	0.40	0.60
m_{lh}^*/m_0	0.087	0.17	0.026	0.12
Dielectric constant ε_s (F/m)	$13.1\varepsilon_0$	$11.11\varepsilon_0$	$15.15\varepsilon_0$	$12.56\varepsilon_0$
Mobility (cm^2/Vs) at 300 K				
Electron	9200	160	$2 \sim 3.3\times10^4$	5370
Hole	400	135	100~450	150

Table A-3: Important Parameters for $In_{1-x}Ga_xAs_yP_{1-y}$ quaternary compounds.[38]

General interpolation formula for quaternary alloy parameter
$P(A_xB_{1-x}C_yD_{1-y})$=xyP(AC)+(1-x)(1-y)P(BD)+(1-x)yP(BC)+x(1-y)P(AD)

$In_{1-x}Ga_xAs_yP_{1-y}$

$$Eg(x,y) = 1.35 + 0.668x - 1.068y + 0.758x^2 + 0.078y^2 - 0.069xy - 0.322x^2y + 0.03xy^2 \text{ (eV) at 300 K}$$

$$a(x,y) = 5.8687 - 0.4181x + 0.1896y + 0.01339xy \text{ (Å)}$$

Lattice matched to InP

$$x = \frac{0.1896y}{0.4181 - 0.01339y}$$

Lattice matched to GaAs

$$x = \frac{0.21511 + 0.1896y}{0.4181 - 0.01339y}$$

References

[1] J. Bardeen and W. H. Brattain, Phys. Rev. **74**, 230 (1948).

[2] J. A. Hoerni, IEEE Trans. on Electron Devices **8**, 178 (1961).

[3] J. S. Kilby, IEEE Trans. on Electron Devices **23**, 648 (1976).

[4] Robert N. Noyce, U.S. Patent 2,981,877 (1961).

[5] I. M. Ross, Proc. of the IEEE **86**, 7 (1998).

[6] N. Holonyak Jr., IEEE J. of Selected Topics in Quantum Electron. **6**, 1190 (2000).

[7] R. N. Hall, IEEE Trans. on Electron Devices **ED-23**, 700 (1976).

[8] M. G. A. Bernard and G. Duraffourg, Phys. Stat. Solidi (b) **1**, 699 (1961).

[9] R. J. Keyes and T. M. Quist, Proc. of the IRE **50**, 1822 (1962).

[10] J. I. Pankove and J. E. Berkeyheiser, Proc. of the IRE **50**, 1976 (1962).

[11] R. N. Hall, G. E. Fenner, J. D. Kingsley, T. J. Soltys, and R. O. Carlson, Phys. Rev. Lett. **9**, 366 (1962).

[12] M. I. Nathan, W. P. Dumke, G. Burns, D. H. Frederick Jr., and G. Lasher, Appl. Phys. Lett. **1**, 62 (1962).

[13] N. Holonyak Jr. and S. F. Bevacqua, Appl. Phys. Lett. **1**, 82 (1962).

[14] N. Holonyak Jr., U.S. Patnet 3,249,473 (1966).

[15] T. M. Quist, R. H. Rediker, R. J. Keyes, W. E. Krag, B. Lax, A. L. McWhorter, and H. J. Zeigler, Appl. Phys. Lett. **1**, 91 (1962).

[16] W. L. Bond, B. G. Cohen, R. C. C. Leite, and A. Yariv, Appl. Phys. Lett. **2**, 57 (1963).

[17] H. Kroemer, Proc. of the IEEE **51**, 1782 (1963).

[18] J. M. Woodall, H. Rupprecht, and G. D. Pettit, IEEE Trans. Electron Devices **14**, 630 (1967).

[19] H. Nelson, RCA Rev. **24**, 603 (1963).

[20] H. Rupprecht, J. M. Woodall, and G. D. Pettit, Appl. Phys. Lett. **11**, 81 (1967); H. Rupprecht, J. Woodall, G. Pettit, J. Crowe, and H. Quinn, IEEE J. Quantum Electron. **4**, 35 (1968).

[21] I. Hayashi, IEEE J. Quantum Electron. **4**, 113 (1968).

[22] H. Kressel and H. Nelson, RCA Rev. **30**, 106 (1969).

[23] I. Hayashi, M. Panish, and P. Foy, IEEE J. Quantum Electron. **5**, 211 (1969); M. Panish, I. Hayashi, and S. Sumski, IEEE J. Quantum Electron. **5**, 210 (1969).

[24] I. Hayashi and M. B. Panish, J. Appl. Phys. **41**, 150 (1970).

[25] Zh I. Alferov, V. M. Andreev, V. I. Korol'kov, E. L. Portoni, and D. N. Tret'yakov, Sov. Phys. Semicond. **2**, 843 (1969); Zh I. Alferov, V. M. Andreev, E. L. Portnoi, and M. K. Trukan, Sov. Phys. Semicond. **3**, 1107 (1970).

[26] I. Hayashi, M. B. Panish, P. W. Foy, and S. Sumski, Appl. Phys. Lett. **17**, 109 (1970); I. Hayashi, M. B. Panish, and F. K. Reinhart, J. Appl. Phys. **42**, 1929 (1971).

[27] Zh. I. Alferov, V. M. Andreev, D. Z. Garbuzov, Yu V. Zhilyaev, E. P. Morozov, E. L. Portoni, and V. G. Trofim, Sov. Phys. Semicond. **4**, 1573 (1971).

[28] R. Dingle and Ch. H. Henry, U.S. Patent 3,982,207 (1976).

[29] R. D. Dupuis, P. D. Dapkus, R. Chin, N. Holonyak Jr., and S. W. Kirchoefer, Appl. Phys. Lett. **34**, 265 (1979).

[30] R. Chin, N. Holonyak Jr., B. A. Vojak, K. Hess, R. D. Dupuis, and P. D. Dapkus, Appl. Phys. Lett. **36**, 19 (1980).

[31] N. Holonyak Jr., R. Kolbas, R. Dupuis, and P. Dapkus, IEEE J. of Quantum Electron. **16**, 170 (1980); H. C. Casey Jr. and M. B. Panish, Heterostructure Lasers (Academic Press, New York, 1978).

[32] Y. Arakawa and H. Sakaki, Appl. Phys. Lett. **40**, 939 (1982).

[33] R. Beanland, D. J. Dunstan, and P. J. Goodhew, Adv. Phys. **45**, 87 (1996).

[34] W. E. Hoke, R. E. Leoni, C. S. Whelan, T. D. Kennedy, A. Torabi, P. F. Marsh, Y. Zhang, C. Xu, and K. C. Hsieh, J. Vac. Sci. Technol. B **22**, 1554 (2004).

[35] L. Y. Karachinsky, et al., Semicond. Sci. Technol. **21**, 691 (2006).

[36] A. Adams and E. P. O'Reilly, Physics World **5**, 43 (1992).

[37] E. P. O'Reilly, Semicond. Sci. and Tech. **4**, 121 (1989).

[38] Sh. L. Chuang, Physics of Optoelectronic Devices, 1st ed. (Wiley-Interscience, NewYork, 1995).

[39] E. P. O'Reilly and A. R. Adams, IEEE J. of Quantum Electron. **30**, 366 (1994).

[40] M. O. Manasreh Ed., Optoelectronic Properties of Semiconductors and Superlattices - Strained-Layer Quantum Wells and Their Application (Gordon and Breach Science Publishers, Amesterdam, The Netherlands, 1997).

[41] J. Singh, Physics of Semiconductors and Their Heterostructures (McGraw-Hill, New York, 1993); J. Singh, Electronic and Optoelectronic Properties of Semiconductor Structures, 1st ed. (Cambridge University Press, UK, 2003).

[42] T. P. Pearsall Ed., Strained-layer Super-lattices: Materials Science and Technology (Academic Press, MA, 1991).

[43] E. Yablonovitch and E. O. Kane, J. of Lightwave Technology **6**, 1292 (1988).

[44] A. Adams and E. P. O'Reilly, Physics World **5**, 43 (1992); P. J. A. Thijs, L. F. Tiemeijer, P. I. Kuindersma, J. J. M. Binsma, and T. Van Dongen, IEEE J. of Quantum Electron. **27**, 1426 (1991).

[45] M. Yano, M. Nogami, Y. Matsushima, and M. Kimata , Jpn. J. Appl. Phys. **16**, 2131 (1977).

[46] W. J. Schaffer, M. D. Lind, S. P. Kowalczyk, and R. W. Grant, J. Vac. Sci. Technol. B **1**, 688 (1983).

[47] L. Goldstein, F. Glas, J. Y. Marzin, M. N. Charasse, and G. Le Roux, Appl. Phys. Lett. **47**, 1099 (1985).

[48] F. Houzay, C. Guille, J. M. Moison, P. Henoc, and F. Barthe, J. of Crys. Growth **81**, 67 (1987).

[49] B. Elman, E. S. Koteles, P. Melman, C. Jagannath, J. Lee, and D. Dugger, Appl. Phys. Lett. **55**, 1659 (1989).

[50] P. M. Petroff, A. C. Gossard, R. A. Logan, and W. Wiegmann, Appl. Phys. Lett. **41**, 635 (1982).

[51] L. Birotheau, A. Izrael, J. Y. Marzin, R. Azoulay, V. Thierry-Mieg, and F. R. Ladan, Appl. Phys. Lett. **61**, 3023 (1992).

[52] A. Izrael, B. Sermage, J. Y. Marzin, A. Ougazzaden, R. Azoulay, J. Etrillard, V. Thierry-Mieg, and L. Henry, Appl. Phys. Lett. **56**, 830 (1990).

[53] A. Forchel, R. Steffen, T. Koch, M. Michel, M. Albrecht, and T. L. Reinecke, Semicond. Sci. and Tech. **11**, 1529 (1996).

[54] W. A. Saunders, P. C. Sercel, H. A. Atwater, K. J. Vahala, and R. C. Flagan, Appl. Phys. Lett. **60**, 950 (1992); P. C. Sercel, W. A. Saunders, H. A. Atwater, K. J. Vahala, and R. C. Flagan, Appl. Phys. Lett. **61**, 696 (1992).

[55] M. L. Steigerwald and L. E. Brus, Annu. Rev. Mater. Sci. **19**, 471 (1989); M. A. Olshavsky, A. N. Goldstein, and A. P. Alivisatos, J. Am. Chem. Soc. **112**, 9438 (1990).

[56] M. Krahl, E. Kapon, L. M. Schiavone, B. P. Van der Gaag, J. P. Harbison, and L. T. Florez, Appl. Phys. Lett. **61**, 813 (1992).

[57] R. Nötzel, N. N. Ledentsov, L. Däweritz, M. Hohenstein, and K. Ploog, Phys. Rev. Lett. **67**, 3812 (1991).

[58] K. Brunner, U. Bockelmann, G. Abstreiter, M. Walther, G. Böhm, G. Tränkle, and G. Weimann, Phys. Rev. Lett. **69**, 3216 (1992).

[59] M. Sopanen, H. Lipsanen, and J. Ahopelto, Appl. Phys. Lett. **66**, 2364 (1995); H. Lipsanen, M. Sopanen, and J. Ahopelto, Phys. Rev. B **51**, 13868 (1995).

[60] D. J. Eaglesham and M. Cerullo, Phys. Rev. Lett. **64**, 1943 (1990).

[61] D. Leonard, M. Krishnamurthy, C. M. Reaves, S. P. Denbaars, and P. M. Petroff, Appl. Phys. Lett. **63**, 3203 (1993).

[62] D. Leonard, M. Krishnamurthy, S. Fafard, J. L. Merz, and P. M. Petroff, J. Vac. Sci. Technol. B **12**, 1063 (1994).

[63] D. Leonard, K. Pond, and P. M. Petroff, Phys. Rev. B **50**, 11687 (1994).

[64] J. M. Moison, F. Houzay, F. Barthe, L. Leprince, E. Andre, and O. Vatel, Appl. Phys. Lett. **64**, 196 (1994).

[65] D. Bimberg, M. Grundmann, and N. N. Ledentsov, Quantum Dot Heterostructures (Wiley & Sons, England, 1999).

[66] F. C. Frank and van der Merwe, J. H., Proceedings of the Royal Society of London, Series A, Mathematical and Physical Sciences **198**, 205 (1949); **198**, 216 (1949); **200**, 125 (1949); **201**, 261 (1950).

[67] M. Volmer and A. Weber, Z. Phys. Chem. **119**, 277 (1926).

[68] I. N. Stranski and Von L. Krastanow, Akad. Wiss. Lit. Mainz Math.-Natur. KI. IIb **146**, 797 (1939).

[69] N. Kirstaedter, et al., Electronics Letters **30**, 1416 (1994).

[70] S. Fafard, K. Hinzer, S. Raymond, M. Dion, J. McCaffrey, Y. Feng, and S. Charbonneau, Science **274**, 1350 (1996).

[71] T. Miya, Y. Terunuma, T. Hosaka, and T. Miyashita, Electron. Lett. **15**, 106 (1979).

[72] I. Tångring, H. Q. Ni, B. P. Wu, D. H. Wu, Y. H. Xiong, S. S. Huang, Z. C. Niu, S. M. Wang, Z. H. Lai, and A. Larsson, Appl. Phys. Lett. **91**, 221101 (2007).

[73] D. Gollub, S. Moses, M. Fischer, and A. Forchel, Electronics Letters **39**, 777 (2003).

[74] S. R. Bank, M. A. Wistey, L. L. Goddard, H. B. Yuen, V. Lordi, and J. S. Harris Jr., IEEE J. of Quantum Electron. **40**, 656 (2004).

[75] R. P. Mirin, J. P. Ibbetson, K. Nishi, A. C. Gossard, and J. E. Bowers, Appl. Phys. Lett. **67**, 3795 (1995).

[76] H. Saito, K. Nishi, and Sh. Sugou, Appl. Phys. Lett. **73**, 2742 (1998).

[77] E. C. Le Ru, A. J. Bennett, C. Roberts, and R. Murray, J. Appl. Phys. **91**, 1365 (2002).

[78] B. Alloing, C. Zinoni, V. Zwiller, L. H. Li, C. Monat, M. Gobet, G. Buchs, A. Fiore, E. Pelucchi, and E. Kapon, Appl. Phys. Lett. **86**, 101908 (2005).

[79] D. L. Huffaker, G. Park, Z. Zou, O. B. Shchekin, and D. G. Deppe, Appl. Phys. Lett. **73**, 2564 (1998).

[80] L. F. Lester, A. Stintz, H. Li, T. C. Newell, E. A. Pease, B. A. Fuchs, and K. J. Malloy, IEEE Photon. Tech. Lett. **11**, 931 (1999).

[81] A. E. Zhukov, et al., Appl. Phys. Lett. **75**, 1926 (1999).

[82] A. E. Zhukov, et al., IEEE Photon. Tech. Lett. **11**, 1345 (1999).

[83] Y. Nakata, K. Mukai, M. Sugawara, K. Ohtsubo, H. Ishikawa, and N. Yokoyama, J. of Crys. Growth **208**, 93 (2000).

[84] N. N. Ledentsov, et al., Electron. Lett. **39**, 1126 (2003).

[85] M. Grundmann, et al., J. Mater. Sci.: Mater. Electron. **13**, 643 (2002).

[86] V. M. Ustinov, et al., Nanotechnology **11**, 397 (2000).

[87] A. Zhukov, A. Vasilyev, E. Semenova, N. Kryzhanovskaya, A. Gladyshev, M. Maximov, V. Ustinov, and N. Ledentsov, Proc. SPIE **5946**, 594616 (2005).

[88] L. Seravalli, M. Minelli, P. Frigeri, P. Allegri, V. Avanzini, and S. Franchi, Appl. Phys. Lett. **82**, 2341 (2003).

[89] N. N. Ledentsov, et al., Proc. SPIE **5624**, 335 (2005).

[90] N. Ledentsov, U.S. Patent 6,653,166 (2003).

[91] J. A. Czaban, D. A. Thompson, and B. J. Robinson, Semicond. Sci. Technol. **22**, 408 (2007).

[92] D. B. Holt, J. Mater. Sci. **23**, 1131 (1988).

[93] J. Taftø and J. C. H. Spence, J. Appl. Cryst. **15**, 60 (1982).

[94] E. Spiecker, Ultramicroscopy, **92**, 111 (2002).

[95] Y. Tarui, Y. Komiya, and Y. Harada, J. Electrochem. Soc. **118**, 118 (1971).

[96] D. J. Stirland and B. W. Straughan, Thin Solid Films **31**, 139 (1976).

[97] B. Tuck, J. Mater. Sci. **10**, 321 (1975).

[98] B. A. Fox and W. A. Jesser, J. Appl. Phys. **68**, 2739 (1990).

[99] A. R. Clawson, Materials Science and Engineering: Reports **31**, 1 (2001).

[100] A. Iida and K. Kohra, Phys. Stat. Sol. (a) **51**, 533 (1979).

[101] K. Matney et al., BEDE Contour, Ver. 2.8.04; BEDE Scientific Inc., Centennial, CO, USA, 2005.

[102] J. W. Edington, (Van Nostrand Reinhold Co., New York, 1976), pp. 281-289.

[103] C. Kittel, 7th ed., (Wiley, New York, 1996), pp. 29-50.

[104] M. Fatemi, J. Cryst. Growth **207**, 188 (1999).

[105] S. Adachi, Handbook on Physical Properties of Semiconductors, 1st ed. (Kluwer Academic Publishers, Massachusetts, 2004), Vol. 2, p. 378.

[106] J. C. Bravman and R. Sinclair, J. Electron Microsc. Tech. **1**, 53 (1984).

[107] E. Spiecker, J. Schöne, S. Rajagopalan, and W. Jäger, Microscopy of Semiconducting Materials edited by Cullis and Hutchison, Proceedings of the 14th Conference ed., (Springer Berlin Heidelberg, Oxford, UK, 2005), pp. 117-130.

[108] P.B. Hirsch, A. Howie, R. B. Nicholson, D. W. Pashley, and M.J. Whelan, 2nd ed. (R. E. Krieger Pub. Co., FL, 1977), pp. 91-97; D. B. Williams and C. B. Carter, (Plenum Press, New York, 1996), pp. 239-244.

[109] M. H. Loretto, Electron Beam Analysis of Materials, 2nd ed. (Springer, 1993), p. 272.

[110] J.W. Steeds, Introduction to Analytical Electron Microscopy, edited by Hren, Goldstein and Joy, (Plenum Press, New York, 1979), pp. 387-422.

[111] R. Ayer, J. Electron Microsc. Tech. **13**, 16 (1989).

[112] M. Raghavan, J. C. Scanlon, and J. W. Steeds, Met. Trans. A **15**, 1299 (1984).

[113] J. of Applied Crystallography **24**, 264 (1991).

[114] M. D. Abramoff, P. J. Magelhaes, and S. J. Ram, Biophotonics International **11**, 36 (2004).

[115] M. S. Abrahams and C. J. Buiocchi, J. Appl. Phys. **36**, 2855 (1965).

[116] V. Gottschalch, R. Srnanek, and G. ER Wagner, J. Mater. Sci. Lett. **1**, 358 (1982).

[117] J. W. Matthews and A. E. Blakeslee, J. Vac. Sci. Technol. **14**, 989 (1977).

[118] P. Voisin, Proc. SPIE **861**, 88 (1988).

[119] E. A. Fitzgerald, Materials Science Reports 7, 87 (1991).

[120] R. Beanland, C. J. Kiely, and R. C. Pond, Handbook on Semiconductors edited by Mahajan, (Elsevier Science B.V., 1994), Vol. 3, pp. 1149-1230.

[121] D. J. Dunstan, J. Mater. Sci.: Mater. Electron. **8**, 337 (1997).

[122] M. S. Abrahams, J. Blanc, and C. J. Buiocchi, Appl. Phys. Lett. **21**, 185 (1972).

[123] G. H. Olsen, M. S. Abrahams, and T. J. Zamerowski, J. Electrochem. Soc. **121**, 1650 (1974).

[124] H. Steinhardt and P. Haasen, Phys. Stat. Sol. (a) **49**, 93 (1978).

[125] P. D. Warren, P. Pirouz, and S. G. Roberts, Phil. Mag. A **50**, L23 (1984).

[126] E. Peissker, P. Haasen, and H. Alexander, Phil. Mag. **7**, 1279 (1962).

[127] S. K. Choi, M. Mihara, and T. Ninomiya, Jpn. J. Appl. Phys. **16**, 737 (1977).

[128] J. P. Hirth and J. Lothe, Theory of Dislocations (Krieger Publishing Company, 1992); D. Hull and D. J. Bacon, Introduction to Dislocations, 3rd ed. (Pergamon Press, 1984).

[129] H. Gottschalk, G. Patzer, and H. Alexander, Physica Status Solidi (a) **45**, 207 (1978).

[130] N. Thompson, Proc. Phys. Soc. B **66**, 481 (1953).

[131] B. C. De Cooman and C. B. Carter, Acta Metall. **37**, 2765 (1989); B. C. De Cooman, C. B. Carter, K. T. Chan, and J. R. Shealy, Acta Metall. **37**, 2779 (1989).

[132] H. Nagai, J. Appl. Phys. **45**, 3789 (1974).

[133] G. H. Olsen and R. T. Smith, Phys. Stat. Sol. (a) **31**, 739 (1975).

[134] J. A. Olsen, E. L. Hu, S. R. Lee, I. J. Fritz, A. J. Howard, B. E. Hammons, and J. Y. Tsao, J. Appl. Phys. **79**, 3578 (1996).

[135] H. Ehsani, I. Bhat, R. J. Gutmann, G. Charache, and M. Freeman, J. Appl. Phys. **86**, 835 (1999).

[136] M. K. Hudait, Y. Lin, M. N. Palmisiano, C. Tivarus, J. P. Pelz, and S. A. Ringel, J. Appl. Phys. **95**, 3952 (2004).

[137] F. K. LeGoues, P. M. Mooney, and J. O. Chu, Appl. Phys. Lett. **62**, 140 (1993).

[138] S. K. Ghandhi and J. E. Ayers, Appl. Phys. Lett. **53**, 1204 (1988).

[139] K. Nozawa and Y. Horikoshi, Jpn. J. Appl. Phys. **32**, 626 (1993).

[140] A. Kikuchi and K. Kishino, Appl. Phys. Lett. **60**, 1046 (1992); M. Ettenberg, C. Nuese, J. Appert, J. Gannon, and R. Enstrom, J. Electron. Mater. **4**, 37 (1975).

[141] J. M. Burgers, Proc. Phys. Soc. **52**, 23 (1940).

[142] W. T. Read and W. Shockley, Phys. Rev. **78**, 275 (1950).

[143] F. L. Vogel, W. G. Pfann, H. E. Corey, and E. E. Thomas, Phys. Rev. **90**, 489 (1953).

[144] M. Hao, Ch Shao, T. Soga, T. Jimbo, M. Umeno, and J. Liang, J. Crys. Growth **178**, 276 (1997).

[145] J. E. Ayers, S. K. Ghandhi, and L. J. Schowalter, J. Cryst. Growth **113**, 430 (1991).

[146] B. W. Dodson, D. R. Myers, A. K. Datye, V. S. Kaushik, D. L. Kendall, and B. Martinez-Tovar, Phys. Rev. Lett. **61**, 2681 (1988); J. Y. Tsao, Materials Fundamentals of Molecular Beam Epitaxy, 1st ed. (Academic Press, San Diego, CA, 1992).

[147] O. Hulko, D. A. Thompson, J. A. Czaban, and J. G. Simmons, Appl. Phys. Lett. **89**, 061915 (2006).

[148] O. Hulko, D. A. Thompson, B. J. Robinson, and J. G. Simmons, J. Appl. Phys. **105**, 073507 (2009).

[149] E. J. Heller and M. G. Lagally, Appl. Phys. Lett. **60**, 2675 (1992).

[150] K. Ohta, T. Kojima, and T. Nakagawa, J. Cryst. Growth **95**, 71 (1989).

[151] M. Grundmann, U. Lienert, D. Bimberg, A. Fischer-Colbrie, and J. N. Miller, Appl. Phys. Lett. **55**, 1765 (1989).

[152] K. L. Kavanagh, J. C. P. Chang, J. Chen, J. M. Fernandez, and H. H. Wieder, J. Vac. Sci. Technol. B **10**, 1820 (1992).

[153] M. S. Abrahams, J. Blanc, and C. J. Buiocchi, Appl. Phys. Lett. **21**, 185 (1972).

[154] K. L. Kavanagh, M. A. Capano, L. W. Hobbs, J. C. Barbour, P. M. J. Maree, W. Schaff, J. W. Mayer, D. Pettit, J. M. Woodall, J. A. Stroscio, and R. M. Feenstra, J. Appl. Phys. **64**, 4843 (1988).

[155] J. Tersoff, Appl. Phys. Lett. **62**, 693 (1993).

[156] Y. Ishida, H. Ishida, K. Kohra, and H. Ichinose, Philos. Mag. A **42**, 453 (1980).

[157] G. B. Stringfellow and G. S. Chen, J. Vac. Sci. Technol. B **9**, 2182 (1991).

[158] C. S. Baxter, W. M. Stobbs, and C. J. Gibbings, Philos. Mag. Lett. **67**, 59 (1993).

[159] E. Spiecker, M. Seibt, W. Schröter, R. Winterhoff, and F. Scholz, Appl. Surf. Sci. **188**, 61 (2002).

[160] P. Dreszer, W. M. Chen, K. Seendripu, J. A. Wolk, W. Walukiewicz, B. W. Liang, C. W. Tu, and E. R. Weber, Phys. Rev. B **47**, 4111 (1993).

[161] B. W. Liang, P. Z. Lee, D. W. Shih, and C. W. Tu, Appl. Phys. Lett. **60**, 2104 (1992).

[162] U. Gösele and F. Morehead, J. Appl. Phys. **52**, 4617 (1981).

[163] M. Schultz, U. Egger, R. Scholz, O. Breitenstein, U. Gösele, and T. Y. Tan, J. Appl. Phys. **83**, 5295 (1998).

[164] A. J. Pidduck, G. W. Smith, A. M. Keir, and C. R. Whitehouse, Proc. Mater. Res. Soc. Symp., **317**, 53 (1994).

[165] R. H. Dixon and P. J. Goodhew, J. Appl. Phys. **68**, 3163 (1990).

[166] G. S. Green, B. K. Tanner, S. J. Barnett, M. Emeny, A. D. Pitt, C. R. Whitehouse, and G. F. Clark, Philos. Mag. Lett. **62**, 131 (1990).

[167] R. Beanland, J. Appl. Phys. **77**, 6217 (1995).

[168] H. Strunk, W. Hagen, and E. Bauser, Appl. Phys. **18**, 67 (1979).

[169] M. A. Capano, Phys. Rev. B **45**, 11768 (1992).

[170] P. M. Petroff and L. C. Kimerling, Appl. Phys. Lett. **29**, 461 (1976).

[171] M. S. Abrahams, L. R. Weisberg, C. J. Buiocchi, and J. Blanc, J. Mater. Sci. **4**, 223 (1969).

[172] W. E. Buhro and V. L. Colvin, Nature Materials **2**, 138 (2003).

[173] Sh. Kan, T. Mokari, E. Rothenberg, and U. Banin, Nature Materials **2**, 155 (2003).

[174] M. Asada, Y. Miyamoto, and Y. Suematsu, IEEE J. of Quantum Electron. **22**, 1915 (1986).

[175] A. A. Guzelian, U. Banin, A. V. Kadavanich, X. Peng, and A. P. Alivisatos, Appl. Phys. Lett. **69**, 1432 (1996).

[176] U. Banin, C. J. Lee, A. A. Guzelian, A. V. Kadavanich, A. P. Alivisatos, W. Jaskolski, G. W. Bryant, Al L. Efros, and M. Rosen, J. Chem. Phys. **109**, 2306 (1998).

[177] P. B. Joyce, T. J. Krzyzewski, G. R. Bell, B. A. Joyce, and T. S. Jones, Phys. Rev. B **58**, R15981 (1998).

[178] G. Costantini, A. Rastelli, C. Manzano, R. Songmuang, O. G. Schmidt, K. Kern, and H. v. Kanel, Appl. Phys. Lett. **85**, 5673 (2004).

[179] P. D. Siverns, S. Malik, G. McPherson, D. Childs, C. Roberts, R. Murray, B. A. Joyce, and H. Davock, Phys. Rev. B **58**, R10127 (1998).

[180] N. P. Kobayashi, T. R. Ramachandran, P. Chen, and A. Madhukar, Appl. Phys. Lett. **68**, 3299 (1996).

[181] B. A. Joyce, J. L. Sudijono, J. G. Belk, H. Yamaguchi, X. M. Zhang, H. T. Dobbs, A. Zangwill, D. D. Vvedensky, and T. S. Jones, Jpn. J. Appl. Phys. **36**, 4111 (1997).

[182] F. Bogani, L. Carraresi, R. Mattolini, M. Colocci, A. Bosacchi, and S. Franchi, Solid-State Electronics **40**, 363 (1996).

[183] M. A. Naser, M. J. Deen, and D. A. Thompson, J. Appl. Phys. **100**, 093102 (2006).

[184] M. A. Naser, M. J. Deen, and D. A. Thompson, J. Appl. Phys. **102**, 083108 (2007).

[185] A. Amtout, S. Raghavan, P. Rotella, G. von Winckel, A. Stintz, and S. Krishna, J. Appl. Phys. **96**, 3782 (2004) and reference therein.

[186] E. F. Schubert, Physical Foundations of Solid-State Devices, 1st ed. (Rensselaer Polytechnic Institute, Troy, New York, 2007).

[187] O. Madelung, Semiconductors: Data Handbook, 3rd ed. (Springer, Berlin, 2004).